

Technical University of Denmark



Monolithic Microwave Integrated Circuits for Wideband SAR System

Johansen, Tom Keinicke; Vidkjær, Jens

Publication date:
2003

Document Version
Publisher's PDF, also known as Version of record

[Link back to DTU Orbit](#)

Citation (APA):
Johansen, T. K., & Vidkjær, J. (2003). Monolithic Microwave Integrated Circuits for Wideband SAR System.

DTU Library
Technical Information Center of Denmark

General rights

Copyright and moral rights for the publications made accessible in the public portal are retained by the authors and/or other copyright owners and it is a condition of accessing publications that users recognise and abide by the legal requirements associated with these rights.

- Users may download and print one copy of any publication from the public portal for the purpose of private study or research.
- You may not further distribute the material or use it for any profit-making activity or commercial gain
- You may freely distribute the URL identifying the publication in the public portal

If you believe that this document breaches copyright please contact us providing details, and we will remove access to the work immediately and investigate your claim.

Tom Johansen

Monolithic Microwave Integrated Circuits for Wideband SAR System

PhD thesis

Electromagnetic Systems

Ørsted•DTU

April 2003

Monolithic Microwave Integrated Circuits for Wideband SAR System

Tom K. Johansen
Oersted-DTU, Electromagnetic Systems
Technical University of Denmark

February 2, 2004

Abstract

In this thesis a technology study of monolithic microwave integrated circuits (MMIC's) for future SAR systems operating at L-, C-, and X-band is performed. As a prerequisite for SAR applications, these MMIC's should demonstrate wideband performance with a high degree of gain flatness and phase linearity. The wide signal bandwidth required in future SAR systems makes the development of MMIC's for this application challenging. Integrated circuit technologies suitable for implementing the key components in a wideband SAR system are identified. These are a $0.8\mu\text{m}$, 35 GHz f_T SiGe HBT process for the quadrature modulator/demodulator subsystem and a $0.2\mu\text{m}$, 63 GHz f_T GaAs pHEMT process for the RF up/downconverter subsystem.

An investigation of the influence of substrate effects on the frequency response of SiGe HBT wideband MMIC's is performed. As part of the investigation, parameter extraction methods for device models including substrate effects are developed for SiGe HBT devices, pad structures, interconnect lines, and poly resistors. A direct parameter extraction method suited for modern poly-silicon SiGe HBT devices is presented. The applicability of the direct parameter extraction method for VBIC95 model parameter extraction is successfully demonstrated.

Wideband active mixers and input buffers are key components for the quadrature modulator/demodulator subsystem. An analysis of the main bandwidth limitations in active mixers based on the Gilbert Cell mixer topology is performed. Advanced circuit techniques are exploited, useful when the objective is to achieve wideband operation with high degree of gain flatness and phase linearity. Experimental results for a wideband active mixer implemented in the SiGe HBT process achieves a 8.5 dB conversion gain with 3 dB bandwidth of 11 GHz and 7.5 GHz for the input port and output ports respectively. The experimental results are well predicted by simulations and demonstrates state-of-the-art results compared with other wideband active mixers implemented in comparable processes. The experimental results for an input buffer in the SiGe HBT process achieves a 3 dB bandwidth of 6.6 GHz with excellent phase linearity. These experimental results are well predicted by simulations. The developed key components are well suited for further integration into quadrature modulator/demodulator SiGe HBT MMIC's.

Key components for the RF up/downconverter includes wideband active mixers, active baluns and active output combiners. A fully integrated RF up/downconverter including active mixer, active baluns on the input and LO port, and an active output combiner on the output port has been implemented in the GaAs pHEMT process. The experimental results for the GaAs pHEMT MMIC achieves a 10 dB conversion gain and a 9.5 GHz 3 dB input port bandwidth. The results are comparable to best published results for state-of-the-art highly integrated wideband active mixers based on FET technologies. RF downconversion from C-band to L-band is demonstrated with an excellent conversion gain flatness over an 800 MHz bandwidth.

Resumé

I denne afhandling beskrives et teknologi studie omkring monolitisk mikrobølge integrerede kredsløb (MMIC'er) til fremtidens syntetisk apertur radar (SAR) systemer virkende ved L-, C-, og X-bånd. Som en forudsætning ved SAR anvendelser, skal disse MMIC'er udvise bredbåndet egenskaber med en høj grad af konstant forstærkning og fase linearitet. Den store signal båndbredde påkrævede i fremtidens SAR systemer betyder at udviklingen af MMIC'er til dette formål er udfordrene. Anvendelige integrerede kredsløbs teknologier til at implementerer hovedkomponenterne i et bredbåndet SAR system er identificeret. Disse er en $0.8\mu\text{m}$, 35 GHz f_T SiGe HBT proces for kvadratur modulatorendemodulatorendelsystemet og en $0.2\mu\text{m}$, 63 GHz f_T GaAs pHEMT proces for RF op/nedkonverter delsystemet.

Der er foretaget en undersøgelse af substrateffekters indflydelse på frekvens responset for SiGe HBT bredbåndet MMIC'er. Som en del af denne undersøgelse, er der udviklet parameter ekstraktions metoder for komponent modeller inkluderende substrateffekter for SiGe HBT komponenter, pad strukturer, forbindelseslinier, og poly modstande. Der præsenteres en direkte ekstraktions metode anvendelig for moderne poly-silicium SiGe HBT komponenter. Anvendeligheden af den direkte parameter extractions metode til parameter extraction af VBIC95 modellen bliver demonstreret med succes.

Hovedkomponenterne i kvadratur modulatorendemodulatorendel består af bredbåndet aktive mixere og indgangsbuffere. Der er foretaget en analyse af de hovedsagelige årsager til båndbredde begrænsningen i aktive mixere baseret på Gilbert Celle mixer topologien. Anvendelsen af avanceret kredsløbsteknikker, brugbare når målet er at opnå stor båndbredde med en høj grad af konstant forstærkning og fase linearitet, er blevet udnyttet. De eksperimentielle resultater for en bredbåndet aktiv mixer implementeret i SiGe HBT processen opnår en konversionsforstærkning på 8.5 dB og en 3 dB båndbredde på henholdsvis 11 GHz på indgangsporten og 7.5 GHz på udgangsporten. De eksperimentielle resultater er temmeligt godt forudset fra simuleringer og demonstrerer state-of-the-art resultater sammenlignet med resultater for andre bredbåndet aktive mixere implementerede i tilsvarende processer. De eksperimentelle resultater for en indgangsbuffer i SiGe HBT processen opnår en 3 dB båndbredde på 6.6 GHz med meget god fase linearitet. Disse eksperimentielle resultater er temmeligt godt forudset fra simuleringer. De udviklede hovedkomponenter er anvendelige for videre integration af kvadratur modulator/demodulator SiGe HBT MMIC'erne.

Hovedkomponenterne for RF op/nedkonverteren indeholder bredbåndet aktive mixere, aktive balun'er og udgangskombinations kredsløb. En fuldt integrerede RF op/nedkonverter indholdende aktiv mixer, aktiv balun'er på indgangs- og LO porten, og et aktivt udgangskombinations kredsløb på udgangsporten er blevet implementeret i GaAs pHEMT processen. De eksperimentielle resultater for GaAs pHEMT MMIC'en opnår 10 dB konversionsforstærkning og en 9.5 GHz 3 dB indgangsport båndbredde. Resultaterne er sammenlignende med de bedste publicerede resultater for state-of-the-art bredbandede aktive mixere med høj grad af integration baseret på FET teknologier. RF nedkonvertering fra C-bånd til L-bånd er demonstreret med en meget god konstant konversionsforstærkning over en 800 MHz båndbredde.

Preface

This Ph.D. Study was carried out from February 1st, 2000 to April 30th, 2003 at the section for Electromagnetic Systems, Ørsted-DTU, Technical University of Denmark, Kgs. Lyngby, Denmark. The effective study period has been 39 month, including a 3 month extension. The financial support for this Ph.D Study was provided by the Technical University of Denmark. Associate Professor Jens Vidkjær acted as project supervisor.

The present study is closely related to the ongoing technology research project at the section for Electromagnetic Systems: Next Generation Synthetic Aperture Radar (SAR); Microelectronics, distributed systems and multi-frequency antennas (SAR++ for short), funded by the Danish Technology Research Council.

Seven month of the Ph.D study has been spent during an external research stay at the center for wireless communication, University of California San Diego (UCSD), California, USA. The main research topic during the external research stay was on low phase noise fully integrated voltage controlled oscillators (VCOs) in SiGe HBT technology. The external research stay gave an opportunity to become familiar with a $0.5\mu\text{m}$, 47 GHz f_T SiGe HBT/BiCMOS process from IBM, considered to be an alternative to the $0.8\mu\text{m}$, 35 GHz f_T SiGe HBT/BiCMOS process from AMS currently used at the section for Electromagnetic Systems, at the Technical University of Denmark. Additional one month was spent at the Technical University of Denmark, performing the experimental verification of the fabricated SiGe HBT VCOs.

Thesis Overview

The main part of this thesis consist of seven chapters. Chapter one and two gives a short introduction to the project. The background for the SAR++ project is described and the SAR++ system is introduced as an example of a state-of-the-art wideband SAR system. Detailed considerations are made with respect to the quadrature modulator/demodulator and RF up/downconverter subsystems. In chapter three suitable integrated circuit technologies for implementing the key components in the quadrature modulator/demodulator and RF up/downconverter subsystems are identified. These are a $0.8\mu\text{m}$, 35 GHz f_T SiGe HBT process for the quadrature modulator/demodulator subsystem and a $0.2\mu\text{m}$, 63 GHz f_T GaAs pHEMT process for the RF up/downconverter subsystem. In this chapter the accuracy of the design-kit model in the SiGe HBT process is investigated and it is found that improvements are needed. In chapter four the influence of substrate effects on the frequency response of SiGe HBT wideband MMIC's is investigated. As part of the investigation, suitable equivalent circuit models for SiGe HBT devices, pad structures, interconnect lines and poly resistors are extracted. A direct parameter extraction method for SiGe HBT devices and the applicability for VBIC95 large signal model parameter extraction is demonstrated. In chapter five SiGe HBT designs for the quadrature modulator/demodulator subsystem are described. Key components are wideband active mixers and input buffers and the design and experimental verification of these circuits are discussed in this

chapter. Chapter six gives a description of GaAs pHEMT designs for the RF up/downconverter subsystem. The design and experimental verification of a RF up/downconverter fully integrated with active baluns, active mixer and active output combiner is discussed. Finally chapter seven gives general conclusions regarding the total project.

The work performed on phase noise in fully integrated SiGe HBT VCOs as part of the external research stay is documented in this thesis by appending an article accepted for publication at the 2003 IEEE Radio Frequency Integrated Circuits (RFIC) Symposium to be held in Philadelphia, USA, later this year. The title of the paper is, Optimization of SiGe HBT VCOs for Wireless Applications, and the article describes a combined theoretical and experimental study on phase noise in fully integrated SiGe HBT VCOs.

Acknowledgments

First of all I want to thank Associate Professor Jens Vidkjær and the section for Electromagnetic Systems for hosting the Ph.D. study. I want to thank all former and present members of the SAR++ project group. A special thanks goes to the members of the analog project group, Jens Vidkjær, Viktor Krozer and Madalina Breten for interesting and inspiring dialogs. Also a special thanks goes to Mogens Pallisgaard for assisting with all measurements during the project period. For an interesting and valuable external research stay I want to thank Professor Larry Larson and all of his group at the center for wireless communication, UCSD, California, USA. In connection with this I would also like to thank IBM for chip fabrication.

Finally I want to acknowledge the Technical University of Denmark for their financial support to the Ph.D study and the Danish Technical Research Council for the financial support necessary for chip fabrication.

Technical University of Denmark
Kgs. Lyngby, April 30th, 2003.

Contents

1	Introduction	1
2	Wideband SAR System	5
2.1	SAR Principle	5
2.2	Distortion in Pulse Compression SAR System	6
2.2.1	Transfer Function Requirements	8
2.3	System Overview	10
2.3.1	Quadrature Modulator/Demodulator Subsystem	11
2.3.2	RF UP/Downconverter Subsystem	14
3	MMIC Technology for Wideband SAR System	17
3.1	Technology Considerations for Wideband Active Mixers	18
3.2	SiGe HBT Technology	21
3.2.1	DC Characteristics	21
3.2.2	RF Performance Verification	23
3.3	GaAs pHEMT Technology	26
4	Substrate Effects in SiGe HBT Technology	29
4.1	Substrate Effects in SiGe HBT Modeling	30
4.1.1	Deembedding of Pad and Interconnect Line Parasitics	30
4.1.2	Direct Parameter Extraction Method for SiGe HBT Equivalent Circuit	33
4.1.3	Applicability of The Extraction Procedure For VBIC95 Modeling	43
4.2	Substrate Effects in Basic Circuit Configurations	53
4.2.1	Influence of Transistor Parasitics	53
4.2.2	Pad Structures and Interconnect Lines Modeling	55
4.2.3	Poly Resistor Modeling	57
4.2.4	Experimental Results	57

5	SiGe HBT Designs for Quadrature Modulator/Demodulator Subsystem	61
5.1	Quadrature Modulator/Demodulator Configuration	62
5.2	Wideband SiGe HBT Active Mixer Design	62
5.2.1	Bandwidth Limitation of The Gilbert Cell Mixer	63
5.2.2	The Principle of Strong Impedance Mismatch	66
5.2.3	Experimental Results	70
5.3	Wideband SiGe HBT Input Buffer Designs	74
5.3.1	Differential Amplifier Stage with Shunt Feedback	75
5.3.2	Experimental Results	77
5.4	System Design Simulation	80
5.4.1	Quadrature Demodulator Configuration Simulation	80
6	GaAs pHEMT Designs for RF Up/Downconverter Subsystem	83
6.1	RF Up/Downconverter Configuration	84
6.2	Balance Considerations in GaAs pHEMT Active Mixers	84
6.2.1	The Effect of Mismatch	86
6.2.2	Input Balun Imperfections	86
6.2.3	LO Balun Imperfections	87
6.3	Wideband GaAs pHEMT Active Mixer Design	88
6.3.1	Active Balun Design	88
6.3.2	Double Balanced Active Mixer Design	90
6.3.3	Active Combiner Design	91
6.3.4	Experimental Results	91
7	Conclusions	96

Chapter 1

Introduction

A synthetic aperture radar (SAR) is an active microwave sensor used for high resolution mapping of the earth's surface. The images obtained with SAR are actually a measurements of the radar cross-section of the terrain mapped. A distinct advantage over other mapping techniques is the operation that is independent of sun light and cloud cover. At the Technical University of Denmark, research in SAR systems has been performed for several years. A fully polarimetric and interferometric L- and C-band SAR system, known as EMISAR, has been developed and operated during airborne campaigns [1].

A technology research project, known as SAR++, is currently being carried out at the Technical University of Denmark. The research is concentrated on improvements in terms of performance, cost, and size in order to make SAR systems more broadly used. To met these objectives the SAR++ project aims at improving design methods and technology for complex microwave sensor systems involving wideband analog, digital, and antenna systems. Wide bandwidth is needed in SAR systems in order to provide high spatial resolution. Future commercial applications of SAR data, such as cartographic mapping, may require signal bandwidths of up to 800 MHz [2].

The analog part of the existing EMISAR system was built with discrete connectorized components as shown in Fig. 1.1. For the system considered in the SAR++ project, this technology is considered obsolete. This is mainly because the primary goal for the SAR++ system is a significant higher signal bandwidth compared with the EMISAR system, which may not be possible due to the unavoidable parasitics that exist between discrete components [3]. To achieve wide bandwidth performance, new technologies like multi chip modules (MCM's), and monolithic microwave integrated circuits (MMIC's) seems promising. In particular the small size, wide-band performance, and flexible circuit design available with MMIC technology is interesting for SAR systems [4–6].

In the analog part of the SAR++ system some subsystems have been identified as critical for the performance, and the use of MCM technology together with monolithic microwave integrated circuits will be attempted. These subsystems are the quadrature modulator/demodulator and RF up/downconverter subsystems. The quadrature modulator/demodulator is expected to operate at a 1.25 GHz (L-band) carrier frequency and should be capable of modulation and demodulation of wideband linear FM-modulated signals. The RF up/downconverter should provide frequency conversion of wideband linear FM-modulated signals between 1.25 GHz and 5.4 GHz (C-Band) or 9.5 GHz (X-band). In a wideband SAR system rather extreme requirements exist to the gain flatness and phase linearity for the key components in the quadrature modulator/demodulator and RF up/downconverter subsystem, unlike in any other application [2].

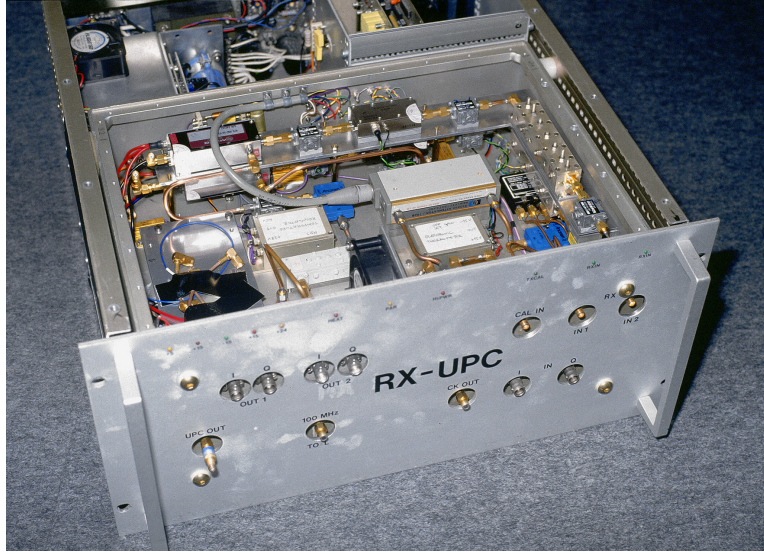


Figure 1.1 RF up/downconverter and quadrature modulator/demodulator subsystems in the analog part of the EMISAR system.

Current activity in the MMIC area mainly focus on wireless and optical communication systems. The trend in wireless communication is toward higher level of integration applying Si-based technologies [7,8]. Circuits for wireless applications are typical of a narrowband nature and therefore unsuitable for a wideband SAR system. Several optical communication circuits operating up to 40 Gbit/second have been demonstrated in the literature [9, 10]. These circuits demonstrates extremely large analog bandwidths, however the gain flatness and phase linearity is not of primary concern. Furthermore, a typical optical communication system consist of multiplexers, demultiplexers, transimpedance amplifiers and limiting amplifiers. These circuit functions differs from up/downconverters, modulators and demodulators required in a wideband SAR system. In general, it is found that commercially available wideband MMIC components suitable for a high-performance SAR system are limited [2].

The purpose of this thesis is to describe a technology study into the development of MMIC's for wideband SAR systems operating at L-, C-, and X-band frequencies. The study includes identification of integrated circuit technologies suitable for the implementation of the key components for the critical subsystems in a wideband SAR system. Among the considerations are the device performance in terms of the unity current gain frequency f_T , maximum frequency of oscillation f_{max} and noise performance as well as the possibility of prototyping in small quantities at a low cost. To develop MMIC designs for a wideband SAR system, with stringent requirements on the gain flatness and phase linearity, the accuracy of the available models becomes an important issue. Part of the study have involved the verification, and whenever necessary, the improvements of the available simulation models in the chosen integrated circuit technologies. The ultimate goal is the ability to predict already from simulations, whether a given MMIC design will degrade the performance of the final SAR system. An extensive investigation of circuit configurations suitable for undistorted frequency conversion and amplification of wideband linear FM-modulated signals at L-, C-, and X-band have been performed and the main findings will be described.

The thesis is organized as follows:

Chapter two gives a short introduction to a wideband SAR system. The basic SAR principle is introduced and the relation that exist between bandwidth and resolution is shown. The requirements on transfer function distortion in a pulse compression SAR system is discussed in

terms of the impulse response parameters of importance for the SAR image quality. The sensor configuration in the analog part of the SAR++ system is described, with emphasis on the quadrature modulator/demodulator and RF up/downconverter subsystems. The specifications for the quadrature modulator/demodulator and RF up/downconverter subsystems in the SAR++ system are given in this chapter.

Chapter three identifies relevant integrated circuit technologies for implementing the key components for the quadrature modulator/demodulator and RF up/downconverter subsystems. A $0.8\mu\text{m}$, 35 GHz f_T SiGe Heterojunction Bipolar Transistor (HBT) process is identified as suitable for the quadrature modulator/demodulator subsystem. For the RF up/downconverter subsystem a $0.2\mu\text{m}$, 63 GHz f_T GaAs pseudomorphic High Electron Mobility Transistor (pHEMT) process is chosen. Experimental results for DC and high-frequency S-parameter measurements on transistor test structure in the SiGe HBT process, shows that the accuracy of the design-kit model is poor and needs to be improved. The chosen GaAs pHEMT technology is suitable for MMIC design, even at millimeter wave frequencies, and the accuracy of the design-kit models will not be questioned here.

Initial investigations, using the $0.8\mu\text{m}$ SiGe HBT process resulted in very poor agreement between simulations and measurements. Part of the explanation for this was that substrate effects were not properly included in the simulation models. In chapter four, an investigation of the influence of substrate effects on the frequency response of SiGe HBT wideband MMIC's is described. As part of the investigation, suitable equivalent circuit models for SiGe HBT devices, pad structures, interconnection lines and poly resistors are extracted. A direct parameter extraction method useful for finding the elements of the equivalent circuit model of modern poly-silicon SiGe HBT devices including fixed oxide capacitances, fixed resistances and substrate parasitics is described in details. The applicability of the direct parameter extraction method for VBIC95 large signal model parameter extraction is demonstrated.

Possible implementations of the SiGe HBT MMIC's for the quadrature modulator/demodulator subsystem are given in chapter five. The key components are wideband active mixers and input buffer stages. A simplified time-varying small-signal model for analyzing the bandwidth limitation of the Gilbert Cell mixer is proposed. The analysis shows that it is in general possible to consider separately the frequency response on the RF and IF port of the Gilbert Cell mixer. Using the knowledge obtained from the analysis, suitable circuit techniques are described, useful when the objective is to achieve wideband operation at both the input and output port of the active mixer. It is verified by simulations, that these circuit techniques in fact improve the gain flatness and phase linearity of the active mixer. The excellent performance of the wideband active mixer circuit predicted by simulations are verified experimentally. An input buffer stage consisting of a differential stage with active shunt feedback and DC adjustment are proposed. The experimental results are reasonable well predicted by simulations. Finally a system design simulation is described in which the designed active mixer is applied in a quadrature demodulator configuration. Matched filtering, performed on the demodulated signal shows practical no degradation compared with the ideal impulse response.

Possible implementation of the GaAs pHEMT MMIC for the RF up/downconverter is given in chapter six. Besides the active mixer, the key components are active baluns, and active output combiner. In the upconverter, LO leakage to the output port is of great concern due to the AM/PM modulation process in the following non-linear high-power traveling wave tube amplifier (the TWT). The cause of LO leakage in a GaAs pHEMT active mixer is discussed, in terms of mismatch effects, input balun imperfections and LO balun imperfections. A compact GaAs pHEMT MMIC with integrated active baluns on the input and LO ports and an active combiner on the output port for C- and X-band SAR applications is described. The experimental results for the GaAs pHEMT MMIC demonstrates wideband operation suitable for C-band SAR

applications. The bandwidth of the GaAs pHEMT MMIC however, is significantly lower than expected from simulations. Therefore wideband operation at X-band is not possible.

General conclusions regarding the total project are given in chapter seven. Suggestions for future work is presented with background in the achieved results, and technological progress in integrated circuit technologies during the project period.

Chapter 2

Wideband SAR System

Advanced high-resolution airborne synthetic aperture radar (SAR) systems involve wide bandwidth analog, digital and antenna subsystems. In this chapter the SAR++ system, being developed at the section for Electromagnetic Systems at the Technical University of Denmark, is shown as an example of a state-of-the-art high-performance wideband SAR system. Emphasis will be put on the analog subsystem, as monolithic microwave integrated circuit (MMIC) technology will mainly be used in this part of the system.

First the basic SAR principle is introduced, and the importance of the signal bandwidth on the resolution is shown. Then requirements for the transfer function distortion in a pulse compression SAR system is considered and the influence on the impulse response parameters (PLSR and ISLR) of interest for the SAR image quality is discussed. The sensor configuration in the analog part of the system is described, including a detailed description of the quadrature modulator/demodulator and RF up/downconverter subsystems. These subsystems are identified as the most critical in wideband SAR systems.

2.1 SAR Principle

An airborne synthetic aperture radar (SAR) achieves high resolution in the along-track direction (azimuth resolution) by coherently collecting echo data along the flight-track [2]. This way a long aperture array antenna may be synthesized. The synthetic aperture array antenna beam width is much smaller than the azimuth beam width for the real antenna and therefore results in much better resolution. The SAR mapping geometry is illustrated in Fig. 2.1. It can be shown [11] that azimuth resolution ρ_a for a SAR is range independent and given by

$$\rho_a = \frac{D}{2} \quad (2.1)$$

where D is the physical length of the antenna.

To achieve high resolution in the cross-track direction (range resolution) a pulse of short duration should ideally be transmitted. However, the transmitter in airborne SAR systems is often peak-power limited resulting in little transmitted energy for short pulses. This leads to an unacceptable reduction in the sensitivity of the SAR system [11]. Instead, a long linear FM-modulated pulse is often transmitted and the high resolution in range is achieved by pulse compression of the received echo signal. The pulse compression is performed by matched filtering in the receiver. A compressed pulse with main lobe width $1/B$ results, where B is the bandwidth of the transmitted linear-FM modulated pulse. The range resolution ρ_r for a pulse

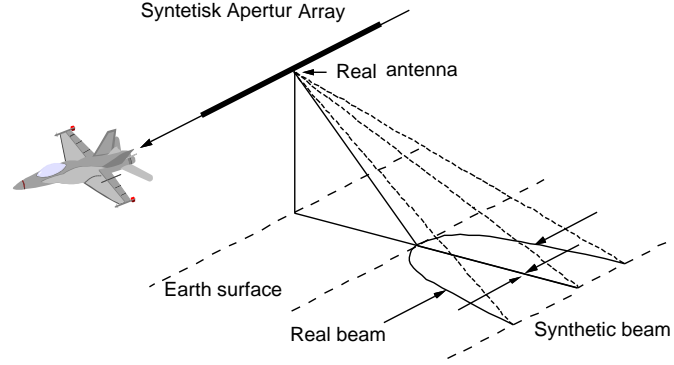


Figure 2.1 SAR mapping geometry.

compression SAR system is given by

$$\rho_r = \frac{c}{2B} \quad (2.2)$$

where c is the speed of light.

The resolution cell, defined as the product of the azimuth and range resolution, is a key performance measure for SAR systems. Often a square resolution cell is chosen, giving the following equation [2]

$$\rho_{sq} = \frac{c^2}{4B^2}. \quad (2.3)$$

The importance of the linear FM-modulated signal bandwidth on resolution is illustrated in Fig. 2.2. The SAR++ system with a 800 MHz signal bandwidth can achieve a square resolution cell of 0.035 m^2 .

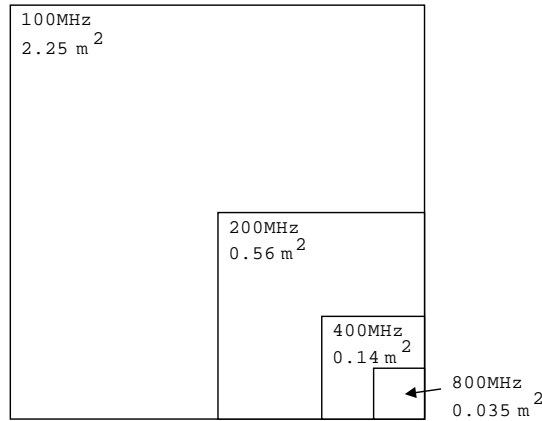


Figure 2.2 Comparison of the square resolution cells for systems with different signal bandwidths.

2.2 Distortion in Pulse Compression SAR System

In a pulse compression SAR system, such as the SAR++ system, the basic requirements are related to the image quality obtained from a point target [12], the so-called impulse response. The point target parameters of interest are the following:

- 3 dB resolution.
- Peak side-lobe ratio (PSLR).
- Integrated side-lobe ratio (ISLR).

The impulse response is the output signal of the matched filter due to the received echo and includes the effect of distortion due to non-ideal components in the receiver and transmitter. Fig. 2.3 shows the impulse response for a point target from an ideal pulse compression SAR system. In an ideal pulse compression SAR system the received signal would correspond to the transmitted signal except for a time delay. The spectrum of the received echo is Hamming weighted in order to suppress the large side-lobes due to an uniform amplitude characteristic of the linear FM-modulated signal. The 3 dB resolution is the width of the main lobe at half the

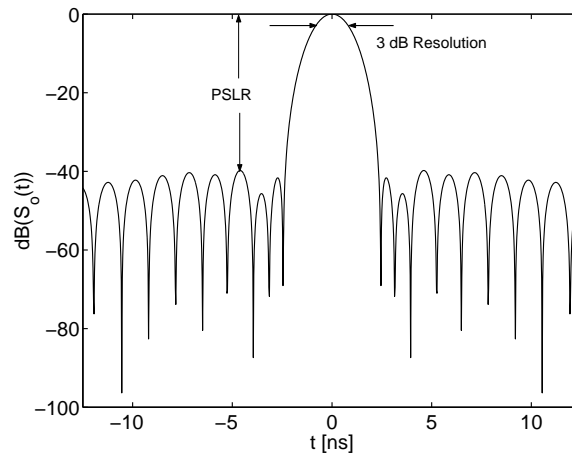


Figure 2.3 Impulse response for ideal pulse compression SAR system.

maximum value as shown in Fig. 2.3, and is a measure of the minimum discernible detail of the image. The peak side-lobe ratio (PSLR) is the ratio of the main lobe of the impulse response to the peak side-lobe level. The PSLR is a measure of the ability of the radar to detect weak reflective targets in the proximity of a strong reflective target. The integrated side-lobe ratio (ISLR) is the ratio of the energy in the side-lobes to the energy in the main lobe. ISLR is a measure of the attainable contrast in the image. In the SAR++ system with 800 MHz signal bandwidth the basic requirements and goals for the point target parameters are stated in Table 2.1.

	<i>Requirements</i>	<i>Design Goals</i>
3 dB resolution [m]	0.25	0.25
PSLR [dB]	-30	-40
ISLR [dB]	-18	-28

Table 2.1 Point target parameter requirements and design goals for the SAR++ system (From [2]).

The point target parameters for a pulse compression SAR system is degraded by signal distortion occurring anywhere in the system [13]. Signal distortion occurs when the amplitude response is not constant and the signal delay is not constant over the bandwidth of the signal. The result is a reduced resolution and increased side-lobe levels. The design goals for the SAR++ system leads to stringent requirements on the transfer function for all components in the system as will be discussed next.

2.2.1 Transfer Function Requirements

The transfer function distortion in a pulse compression SAR system can be divided into three different models [12] describing

- periodic distortion (ripples)
- random distortion
- slowly varying distortion.

The periodic distortion can be treated analytically by considering a linear transfer function

$$H(\omega) = A(\omega)e^{j\Phi(\omega)} \quad (2.4)$$

where $\omega = 2\pi f$ is the angular frequency. If a single sinusoidal amplitude and phase ripple exist

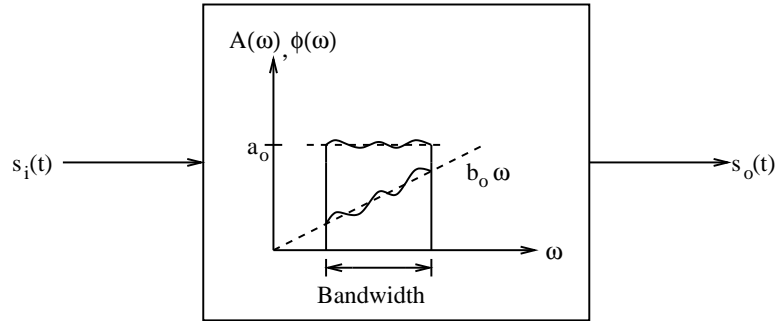


Figure 2.4 Signal transmission through non-ideal component with sinusoidal amplitude and phase ripples.

over the frequency band of interest as shown in Fig. 2.4 the amplitude and phase part of the transfer function in Eq. 2.4 can be expressed as [13]

$$A(\omega) = a_o + a_n \cos(c\omega) \quad (2.5)$$

and

$$\Phi(\omega) = b_o\omega + b_n \sin(c\omega) \quad (2.6)$$

where a_n and b_n are constants describing the deviation from ideal behavior. The transmission of an input signal $s_i(t)$ through a non-ideal component with a single sinusoidal amplitude and phase ripple in the transfer function results in an output signal given by [13]

$$s_o(t) = a_o \left[s_i(t + b_o) + \frac{1}{2} \left(\frac{a_n}{a_o} + b_n \right) s_i(t + b_o + c) + \frac{1}{2} \left(\frac{a_n}{a_o} - b_n \right) s_i(t + b_o - c) \right]. \quad (2.7)$$

The first term in the expression describes the main response as an amplified and time-shifted version of the input signal, whereas the second and third terms are the so-called paired echoes. The relative amplitude of the paired echoes is $a_n/(2a_o)$ for zero phase ripple and $b_n/2$ for zero amplitude ripple. The paired echoes are displaced in time from the main response by $t = \pm c$. The contribution to PSLR from periodic transfer function distortion can be calculated from [12]

$$PSLR_A = 20 \log \left(\frac{a_n}{2a_o} \right) \quad (2.8)$$

for zero phase ripple and

$$PSLR_P = 20 \log \left(\frac{b_n}{2} \right) \quad (2.9)$$

for zero amplitude ripple. The insertion phase of a transmission line mismatched at both ends leads to a periodic transfer function distortion due to multiple reflections [13]. The maximum phase deviation b_n is found from [13] as

$$\tan b_n = \frac{F_T - 1}{\sqrt{4F_T}} \quad (2.10)$$

where

$$F_T = \frac{r_1 r_2 + 1}{r_1 + r_2} \quad (2.11)$$

and r_1 and r_2 are the input and output voltage standing wave ratios (VSWRs) assuming resistive driving source and load impedances. The amount of allowed transmission line mismatch for a given PLSR requirement can be found from Eq. 2.9 using curves of constant phase deviation versus input and output VSWRs as given in [13, page 64, Fig. 3.7]. The frequency period for the ripples is $\omega/(2\beta l)$ where β is the propagation constant [13], meaning that a 1 meter long air filled transmission line generates approximately 5 ripple periods in a 800 MHz bandwidth. Because the position of the side lobes coincidence with the main lobe when the ripple has a period of less than one cycle over the signal bandwidth the contribution to PSLR due to a mismatched transmission line becomes unimportant below a critical length given as

$$l = \frac{c}{\sqrt{\epsilon_{eff}}} \frac{1}{2B} \quad (2.12)$$

where ϵ_{eff} is the effective permittivity for the transmission line structure. As the signal bandwidth increases, the critical transmission line length decreases.

In the preceding analysis it was shown how periodic transfer function distortion leads to paired echoes in a SAR system. In a real system, however, the transfer function exhibits a more complex behavior. This complex behavior is described as random transfer function distortion which can be analyzed by an expansion in Fourier components [12]. The Fourier components will contribute to the side-lobes at many different positions. This mainly contributes to the ISLR performance of the system calculated by [12]

$$ISLR_A = 20 \log a_{rms} \quad (2.13)$$

for an effective amplitude distortion a_{rms} and

$$ISLR_P = 20 \log \phi_{rms} \quad (2.14)$$

for an effective phase distortion ϕ_{rms} .

The last form of transfer function distortion is due to low-frequency phase errors. Low-frequency phase errors are caused by slope error in the generated linear FM-modulated signal, and dispersive components including ripple components with less than one cycle over the signal bandwidth [2, 12, 13]. The result is a broadening of the main lobe and an increase in the sidelobe level.

In Table.2.2 a summary of transfer function requirements and design goals for the SAR++ system are given. The specification for periodic transfer function distortion takes the correlation between the amplitude and phase ripples into account. For random transfer function distortion, the amplitude and phase term is assumed uncorrelated. Furthermore it should be noticed that the considered models for transfer function distortion only give first-order guidelines, which should be aimed at in the beginning of a design. The true picture can only be obtained by accurate simulations or measurements [2].

<i>Parameter</i>	<i>Requirement</i>		<i>Design Goals</i>	
	PSLR=-30dB	ISLR=-18dB	PSLR=-40dB	ISLR=-28dB
Amplitude, Ripple [dB]	0.27	–	0.08	–
Phase, Ripple [Deg.]	1.8	–	0.6	–
Amplitude, RMS [dB]	–	0.53	–	0.17
Phase, RMS [Deg.]	–	3.6	–	1.1
Slow Phase Error [Deg.]	–	60-90	–	45

Table 2.2 Summary of transfer function requirements and design goals for the SAR++ system (From [2]).

2.3 System Overview

In next generation SAR systems aiming at high resolution, increased system scalability, flexibility and reduced system size the major challenges are related to [2]

- wide bandwidth
- design for modularity
- component integration.

The selected microwave carrier frequencies and signal bandwidths for different frequency bands are shown in Table. 2.3. The choice of the carrier frequencies and signal bandwidths for the

Band	<i>Carrier Frequency [GHz]</i>	<i>Bandwidth [MHz]</i>
L	1.25	100
C	5.40	400
X	9.50	800

Table 2.3 Microwave carrier frequency and signal bandwidth for different frequency bands (From [2]).

SAR++ system is related to the available frequency bands for radar applications and the frequency dependence of the backscatter coefficient making certain frequencies more interesting for remote sensing applications [2].

In Fig. 2.5 the sensor configuration to be used in the SAR++ system is shown. Different frequency bands (L-, C-, and X-band) require different sensor configurations. A single channel is used on the transmit side to generate the linear FM-modulated signal around the microwave carrier. Multiple channels are needed on the receive side (only two shown in Fig. 2.5) to be able to implement full polarimetry and interferometry. Each sensor consist of a number of sections. The baseband section (BB Section) contains the digital signal generator (DSG) that generates the I/Q baseband signals, and the digital front end (DFE) that converts the demodulated I/Q baseband signals to digital form. The BB-IF section contains the quadrature modulator converting the I/Q baseband signals to IF and the quadrature demodulator converting the IF to baseband. The BB-IF section will be implemented as one module (The IQMD module) containing the quadrature modulator/demodulator subsystem. The BB-IF section will be identical for all sensors. Frequency conversion from IF to RF, and RF to IF are performed in the IF-RF section by the RF upconverter and downconverter, respectively. The RF-IF section will be implemented as one module (The RFUD module) containing the RF up/downconverter subsystem. In the L-band sensor the IF-RF section is absent as the IF signal from the BB-IF section is already at L-band. The L-band sensor applies the homodyne technique, where the

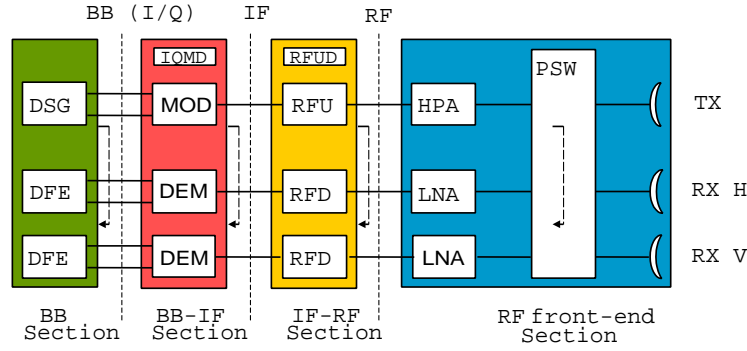


Figure 2.5 Sensor Configuration for the SAR++ system. In the L-Band sensor the IF-RF section is omitted. The transmitting antenna (TX) and two receiving antennas (RX H and RX V) is physical one single dual polarized antenna.

baseband signal is directly modulated and demodulated on the radiated microwave carrier. For wideband SAR applications the homodyne technique has certain advantages compared with the conventional heterodyne technique used in the C- and X-band sensor [14]. Most important is the reduced complexity and fewer bandwidth limiting components. Finally the RF front-end section contains the high power amplifier (HPA) generating the desired RF power level, the low noise amplifiers (LNAs), polarization and T/R switch (PSW), and finally the (multifrequency, dual polarized) antenna. A traveling wave tube (TWT) is used for the high power amplifier, because of the very large bandwidth offered. The TWT normally operates in a highly non-linear mode (saturated mode). As indicated in Fig. 2.5 each section should be able to loop back the signal from the output to the input for calibration purposed. The modular design approach ensures that adding an additional frequency band (Ku-band or higher) only requires the design of a new RF front end and RF up/downconverter.

Additionally to the sensor configuration discussed above, an oscillator subsystem is required in the SAR++ system. A highly stable LO oscillator (STALO) should serve as the system reference oscillator to which all other oscillators must be locked to obtain coherency [2]. The different LO frequencies to be used in the analog part of the SAR++ system are given in Table. 2.4. Lower sideband and upper sideband operation are assumed in the C-band and the X-band

Band	LO Frequency [GHz]
L	1.25
C	6.65
X	8.25

Table 2.4 LO frequencies used in the analog part of the SAR++ system (From [2]).

up/downconverters, respectively, in order to prevent significant interference from image bands.

2.3.1 Quadrature Modulator/Demodulator Subsystem

The quadrature modulator shown in Fig. 2.6a) is needed to convert the complex I/Q baseband signal (DC-400 MHz) to IF ($1.25 \text{ GHz} \pm 400 \text{ MHz}$). The basic modulator configuration consists of two double balanced mixers, a quadrature phase shifter, a power combiner, and two low-pass filters. The low-pass filters are needed to suppress the spurious signals from the digital signal generator. The complex I/Q baseband signal can be represented as

$$m(t) = I(t) + jQ(t) = a(t)e^{j\theta(t)} \quad (2.15)$$

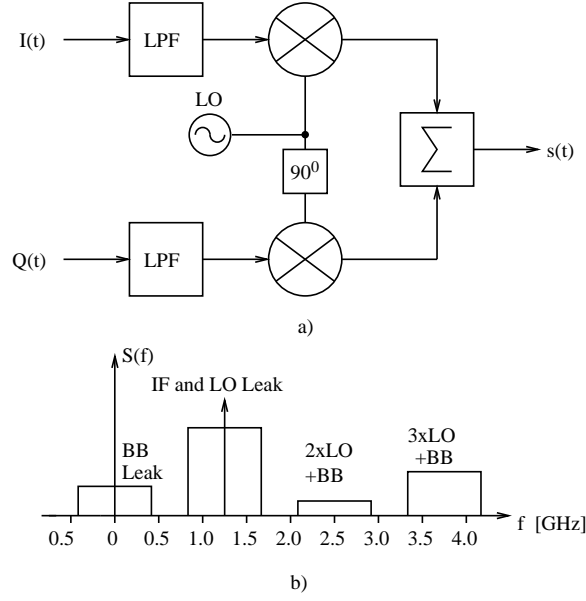


Figure 2.6 Quadrature modulator for SAR system. a) Basic modulator configuration. b) Output spectrum showing baseband leakage, LO leakage and harmonic intermodulation products presents in the modulator.

where $a(t)$ and $\theta(t)$ are the amplitude modulation and phase modulation respectively. The output signal from an ideal modulator is given by

$$s(t) = \Re\{m(t)e^{j2\pi f_{LO}t}\} = a(t) \cos(2\pi f_{LO}t + \theta(t)) \quad (2.16)$$

and represents a frequency conversion of the baseband modulated signal onto the carrier without any by-products [14]. In a real modulator, amplitude and phase imbalance between the I and Q branches produce an output signal given by

$$s(t) = \Re\left\{\left(m(t) + \left(\frac{\Delta a}{2} + j\frac{\Delta\phi}{2}\right)m^*(t)\right)e^{j2\pi f_{LO}t}\right\} \quad (2.17)$$

where $*$ denotes the complex conjugation and Δa and $\Delta\phi$ are the differential amplitude and phase imbalance, respectively. This shows that the output of a real modulator consists of an unwanted signal with reversed phase in addition to the ideal signal. The contribution to ISLR due to amplitude and phase imbalance in the I and Q branches is determined as [12]

$$ISLR = 10 \log \left(\left(\frac{\Delta a}{2}\right)^2 + \left(\frac{\Delta\phi}{2}\right)^2 \right) \quad (2.18)$$

Due to DC-offset in the input signals from the digital signal generator and non-ideal operation of the double balanced mixers the LO signal may leak to the output of the modulator. The LO leakage causes an amplitude modulation of the wanted signal which in turn is converted into phase ripples by the AM/PM conversion process in the TWT. As shown previously, phase ripples degrade the PSLR performance in a wideband SAR system. The amount of carrier leakage allowed is determined by the allowed phase ripple b_n as [12]

$$C = 10^{\frac{1}{20} \frac{b_n}{AM/PM}} - 1 \quad (2.19)$$

where C is the relative amplitude of the carrier and AM/PM is the modulation index (in rad/dB) for the TWT. The AM/PM conversion process due to the TWT is discussed in more details

when discussing the RF upconverter. Non-ideal operation of the double balanced mixers in the modulator also creates baseband leakage and intermodulation products at harmonics of the carrier frequency. These contributions, however, are easily removed by filtering following the modulator. The output spectrum of the quadrature modulator is shown in Fig. 2.6 b).

The quadrature demodulator is needed to convert the linear FM-modulated signal at IF ($1.25 \text{ GHz} \pm 400 \text{ MHz}$) to the complex I/Q baseband signal (DC-400 MHz). The basic demodulator configuration is shown in Fig. 2.7 a) and consists of two double balanced mixers, a quadrature phase shifter, a power divider and two low pass filters. The IF signal input to the quadrature

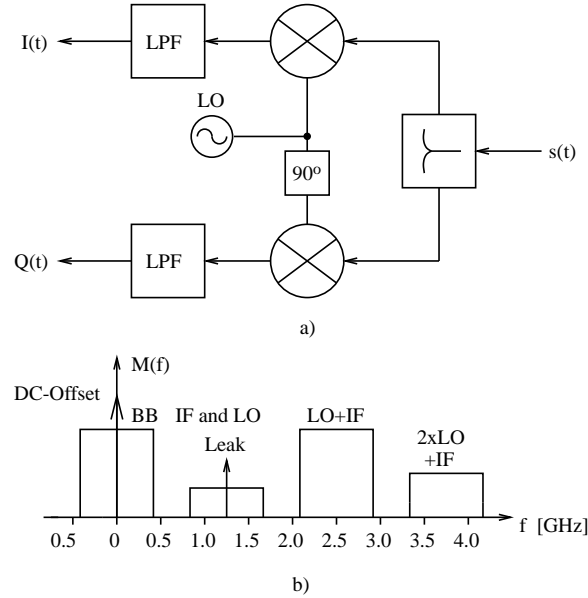


Figure 2.7 Quadrature demodulator for SAR system. a) Basic demodulator configuration. b) Output spectrum showing IF leakage, LO leakage, DC offset, image response (IF+LO) and harmonic intermodulation products in the demodulator.

demodulator can be represented as [15]

$$s(t) = a(t) \cos(2\pi f_{LO}t + \theta(t)) = \frac{m(t)}{2} e^{j2\pi f_{LO}t} + \frac{m^*(t)}{2} e^{-j2\pi f_{LO}t}. \quad (2.20)$$

The baseband I and Q signals are found as

$$I(t) = \Re\left\{\frac{m(t)}{2}\right\} + \Re\left\{\frac{m(t)}{2} e^{j4\pi f_{LO}t}\right\} \quad (2.21)$$

and

$$Q(t) = \Im\left\{\frac{m(t)}{2}\right\} - \Im\left\{\frac{m(t)}{2} e^{j4\pi f_{LO}t}\right\} \quad (2.22)$$

respectively. The low pass filters remove the components at frequency $2f_{LO}$, and the real and imaginary components of the complex modulation function $m(t)$ are recovered. In a real demodulator imperfections due to amplitude and phase imbalance lead to a degradation in the ISLR performance similar to that observed in the modulator. Non-ideal operation of the double balanced mixers may lead to the LO signal leaking to the input of the demodulator and causing a DC offset due to LO-self mixing [15] that adds to the DC offsets in the I and Q branches. DC offset degrades the ISLR performance in a wideband SAR system. Distortion is caused if part of the spectrum is removed by low-frequency cut-off [12]. Instead the demodulator is preferably DC coupled and the DC-offset is removed by either feedback via a D/A converter [2] or a phase

twiddling approach [1]. Besides the LO leakage mentioned above the non-ideal operation of the double balanced mixers in the demodulator also creates IF signal leakage and intermodulation products at harmonics of the carrier frequency. These contributions however are easily removed by filtering following the demodulator. The output spectrum of the quadrature demodulator is shown in Fig. 2.7 b).

In addition to the transfer function specifications given in Table. 2.2 the quadrature modulator/demodulator subsystem should meet the specifications in Table. 2.5. The requirement on

<i>Parameter</i>	<i>Modulator</i>	<i>Demodulator</i>
IF Frequency [MHz]	850-1650	850-1650
Modulation Bandwidth [MHz]	DC-400	DC-400
Amplitude Imbalance [dB]	0.47	0.47
Phase Imbalance [Deg.]	3.2	3.2
Carrier Suppression [dB]	-31.8	–
Gain [dB]	–	22
Noise Figure [dB]	–	12
Return Loss [dB]	-17.7	-17.7
Input 1 dB Compression [dBm]	–	-18

Table 2.5 Specification to the quadrature modulator and demodulator subsystem in order to met the goals for SAR++ system (PLSR=-40dB, ISLR=-28dB) (From [2]). The specifications not yet decided upon are marked with dashed lines (–).

the return loss follows from the phase ripple specification ($b_n = 1.1^\circ$). Assuming equal amount of input and output mismatch the return loss should be kept below -17.7 dB over the signal bandwidth at all transmission line connections. A typical AM/PM modulation index of $5^\circ/\text{dB}$ is assumed in the calculation of the carrier suppression. The gain, noise figure and input 1 dB compression point in the demodulator are chosen in order to optimize the sensitivity and dynamic range of the receiver under various backscatter conditions [2]. The 1 dB compression point is chosen close to the peak signal saturating the analog to digital converters in the digital front end. The requirements on the gain, noise figure and input 1 dB compression point in the modulator will eventually be determined by the signal level from the digital signal generator and the requirements on the transmitter signal to noise ratio (better than -50 dB). The large relative bandwidth of 64% required in the quadrature modulator/demodulator subsystem speaks in favor of a monolithic approach.

2.3.2 RF UP/Downconverter Subsystem

The RF upconverter shown in Fig. 2.8 a) converts the IF ($1.25\text{GHz} \pm 400\text{ MHz}$) to RF ($5.4\text{ GHz} \pm 400\text{ MHz}$ for C-band or $9.5\text{ GHz} \pm 400\text{ MHz}$ for X-band). Previously a 400 MHz bandwidth for the C-band sensor was assumed, however the RF up/downconverter subsystem should preferably be designed for a 800 MHz bandwidth in C-band and an even larger bandwidth in X-band [2]. The basic upconverter consist of a mixer and two bandpass filters for removal of the undesired responses from the quadrature modulator. When the IF signal is upconverted the output signal consist, besides the wanted sideband, of an IF leakage, LO leakage and the unwanted image response, as shown in Fig. 2.8 b). The IF leakage is located far away in frequency from the wanted RF signal and is easily removed by filtering. The LO leakage and image sideband presents a larger problem. Depending on the stopband attenuation of the bandpass filter at the output these unwanted signals may not be fully suppressed. The presence of these unwanted signals lead to an amplitude modulation of the wanted signal as already mentioned in

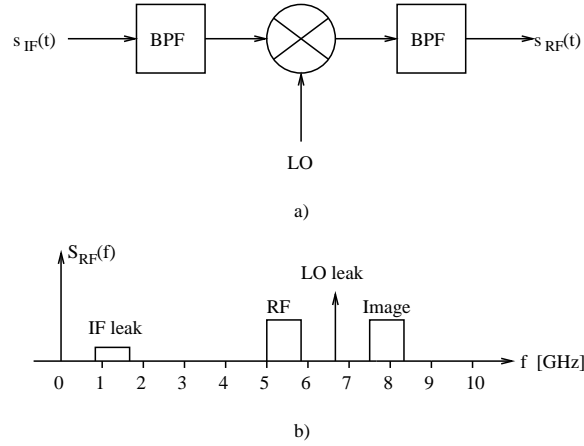


Figure 2.8 RF upconverter for SAR system. a) Basic upconverter configuration. b) Output spectrum showing IF leakage, LO leakage, image response (IF+LO) in the upconverter (C-Band).

connection with the quadrature modulator. If the IF signal is represented as

$$s_{IF}(t) = \Re\{m(t)e^{j2\pi f_{IF}t}\} \quad (2.23)$$

the output of the upconverter becomes

$$s_{RF}(t) = \Re\{m(t)e^{j2\pi(f_{IF}-f_{LO})t} + C|m(t)|e^{j2\pi f_{LO}t} + I|m(t)|e^{j2\pi(f_{IF}+f_{LO})t}\} \quad (2.24)$$

where C and I are the relative amplitudes of the carrier and image signals respectively. The maximum amplitude ripple is found as [12]

$$a[dB] = 20\log(1 + C + I) \quad (2.25)$$

and results in phase ripples given by the relation

$$a[dB] = \frac{b_n}{AM/PM} \quad (2.26)$$

where AM/PM in rad/dB is the TWTs modulation index. For a specified phase ripple the relative amplitudes of the LO leakage and image signals assuming equal LO leakage and image response amplitudes are

$$C = I = \frac{1}{2} \left(10^{\frac{1}{20} \frac{b_n}{AM/PM}} - 1 \right). \quad (2.27)$$

Double balanced mixers are highly recommended as these suppress the amount of LO leakage, relaxing the requirements on the bandpass filter at the output.

The RF downconverter is needed to convert the RF signal ($5.4 \text{ GHz} \pm 400 \text{ MHz}$ at C-band or $9.5 \text{ GHz} \pm 400 \text{ MHz}$ at X-band) to IF ($1.25 \text{ GHz} \pm 400 \text{ MHz}$). The RF downconverter consist of a mixer and two bandpass filters similar to the RF upconverter. The requirement on the carrier suppression is relaxed because the receiver is assumed to be linear. The image band is downconverted to the IF by the downconverter and should be removed by filtering at the input of the downconverter.

The RF upconverter/downconverter subsystem should be designed to meet the specifications in Table. 2.6. The same consideration regarding return loss, AM/PM modulation index, gain, noise figure, and 1 dB compression point applies for the RF up/downconverter as for the quadrature modulator/demodulator. Again the large relative bandwidth speaks in favor of a monolithic approach for the RF up/downconverter subsystem.

<i>Parameter</i>	<i>Upconverter</i>	<i>Downconverter</i>
RF Frequency (C-Band)[MHz]	5000-5800	5000-5800
RF Frequency (X-Band)[MHz]	9100-9900	9100-9900
Carrier Suppression [dB]	-38	–
Image Suppression [dB]	-38	–
Gain [dB]	–	5
Noise Figure [dB]	–	7.2
Return Loss [dB]	-17.7	-17.7
Input 1 dB Compression [dBm]	–	-19

Table 2.6 Specification to the RF upconverter and downconverter subsystem in order to met the goals for the SAR++ system (PLSR=-40dB, ISLR=-28dB) (From [2]). The specification not yet decided upon are marked with dashed lines (–).

Chapter 3

MMIC Technology for Wideband SAR System

Following the discussion of the critical subsystem requirements in a wideband SAR system, this chapter identifies relevant integrated circuit technologies for implementing the key components for the quadrature modulator/demodulator and RF up/downconverter. MMIC technologies are usually specified in terms of basic process features, such as transistor short-circuit unity current gain frequency f_T and maximum frequency of oscillation f_{max} . In general, however, it is difficult to compare different technologies based alone on such figures-of-merit, as these quantities refer to conditions rarely met in circuit designs. Besides technological specifications, other important aspects in choosing the best suited MMIC technology for a wideband SAR system are the possibility for prototyping in small quantities, as well as the accuracy of the available simulation models.

The I/Q modulator/demodulator and RF up/downconverter subsystems consist of mixer based circuits and the bandwidth requirements of these circuits will first be discussed. Then a comparison of the bandwidth capability of various integrated circuit technologies are presented based on published results for state-of-the-art wideband active mixers of the Gilbert Cell mixer topology. The Gilbert Cell mixer topology [16, 17] is generally preferred for monolithic integration due to its high conversion gain over a broad frequency band, and good port-to-port isolation, compared with the passive Schottky diode double-balanced mixer [18]. Apart from substantial conversion loss the passive Schottky diode double-balanced mixer may suffer from passband ripples due to reflections between balun structures and the devices [19]. Passband ripples will degrade the PSLR performance in a wideband SAR system, making passive double-balanced mixers unsuited for this application. Following the initial discussion, suitable processes in SiGe HBT and GaAs pHEMT technologies for SAR applications have been identified. These are a 0.8 μm , 35 GHz f_T SiGe HBT process for the quadrature modulator/demodulator and a 0.2 μm , 63 GHz f_T GaAs pHEMT process for the RF up/downconverter.

A basic overview of the device level performance capabilities in SiGe HBT and GaAs pHEMT technology will be given. Also experimental results for measurements on transistor test structures in the chosen SiGe HBT process are described in order to provide verification of the accuracy of the design-kit models used. It is found that the design-kit models in the SiGe HBT process are inaccurate and need to be improved to predict the performance of the SiGe HBT MMIC's. The chosen GaAs pHEMT technology is suitable for MMIC design, even at millimeter wave frequencies and have proven to be accurate.

3.1 Technology Considerations for Wideband Active Mixers

Wideband active mixers are important building blocks in the analog part of SAR systems that require frequency conversion, modulation and demodulation of wideband linear-FM modulated signals. Fig. 3.1 illustrates applications for wideband active mixers in a SAR system. In the quadrature modulator the linear FM-modulated baseband signal is modulated onto a microwave carrier at L-band. The L-band carrier is then upconverted into C- or X-band microwave carrier in the RF upconverter. In the RF downconverter, a received C- or X-band linear-FM modulated microwave carrier is downconverted to a L-band signal and demodulated to baseband in the quadrature demodulator.

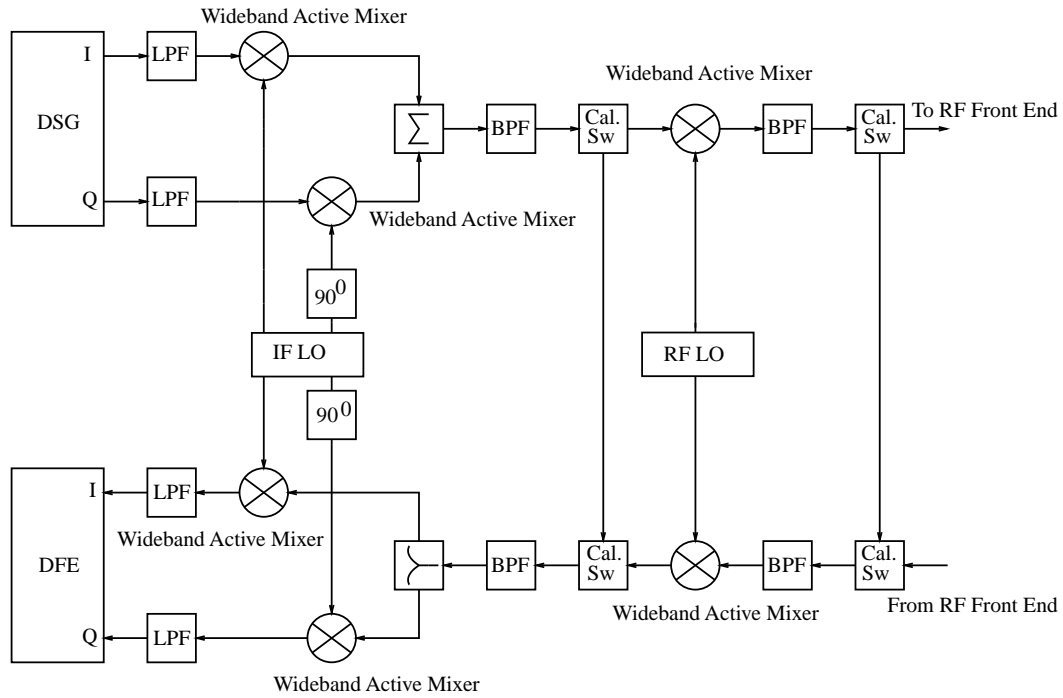


Figure 3.1 Block diagram of SAR system showing applications for wideband active mixers.

The bandwidth requirements on the different ports for the active mixers in a SAR system are determined by the need for undistorted transmission and reception of a wideband linear-FM modulated signal through the system. During transmission and reception, all components in the signal path contribute to the overall bandwidth shrinkage of the signal. If the individual components are designed for a 800 MHz 0.1dB bandwidth, the combined result is assumed to ensure a 800 MHz 3dB signal bandwidth for the full system. This sets a minimum requirement on the high-frequency fall-off at the upper end of the frequency band of interest. In the case of wideband active mixers for quadrature demodulation at L-band with a carrier frequency of 1.25 GHz, the high-frequency fall-off should not exceed 0.1dB at 1.65 GHz. For the RF downconverter, the high-frequency fall-off should not exceed 0.1dB at 5.8 GHz and 9.9 GHz for the C-band and X-band SAR system, respectively. Assuming for now a 20 dB/decade high-frequency fall-off rate for the conversion gain for active mixers based on the Gilbert Cell mixer topology¹, the 1.65 GHz 0.1dB bandwidth requirement for the active mixers in the quadrature demodulator translates into a 10.8 GHz 3dB bandwidth requirement. Thus, in order to receive a linear-FM modulated signal around an L-band carrier at 1.25 GHz, a 10.8 GHz 3dB bandwidth

¹The 20 dB/decade high-frequency fall-off rate corresponds to assuming a first order frequency response for the conversion gain of the Gilbert Cell mixer topology.

is actually required for the active mixer. Similar consideration for the active mixer in the C-band to L-band RF downconverter, the 800 MHz 0.1 dB bandwidth requirement translate into a 37.9 GHz 3dB bandwidth requirement. For the X-band RF downconverter active mixer the 3dB bandwidth requirements becomes even larger. Of cause the above consideration should be taken with a grain of salt, as circuit techniques exist for compensation of the high-frequency fall-off in active mixers, relaxing the 3dB bandwidth requirements. It will, however, serve as a rough guideline for identifying relevant integrated circuit technologies for the key building blocks for the critical subsystems in a wideband SAR system.

In Fig. 3.2 the input port 3dB bandwidth performance for state-of-the-art wideband active mixers in InP HBT [18], Si BJT [19], [20], GaAs MESFET [21], SiGe HBT [22], [23], GaAs HBT [24] and GaAs pHEMT [25] technologies is shown versus the transistors unity current gain frequency f_T (left plot), and maximum unity power gain frequency f_{max} (right plot). The input port bandwidth of an active mixer is found with swept RF/LO-frequencies and fixed IF-frequency. In general, a good correlation is observed between the device f_T and the reported input port bandwidth performance independent of the technology used. Surprisingly, the device f_{max} seems to have only a secondary influence on the input port bandwidth performance for the active mixers. In general, it seems like a 3 dB input port bandwidth of approximately $f_T/4$ can be achieved regardless of the integrated circuit technology considered.

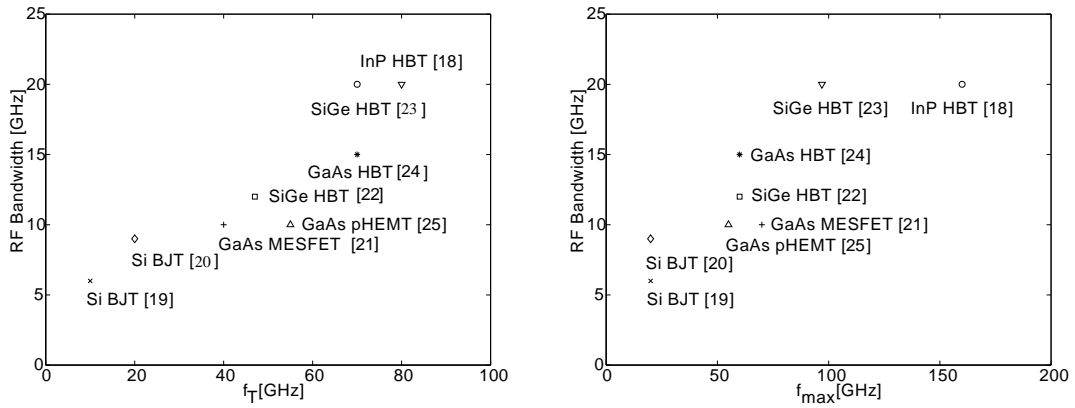


Figure 3.2 Input port bandwidth performance for state-of-the-art wideband active mixers. Left: Input port bandwidth versus unity current gain frequency f_T . Right: Input port bandwidth versus maximum frequency of oscillation f_{max} . All results for the input port bandwidth are stated for a fixed low frequency IF-frequency with swept RF/LO-frequencies.

The output port bandwidth capability of active mixers becomes an important issue in a SAR system in two situations: a) when a wideband linear-FM modulated signal around a C/X-band carrier is downconverted to L-band with the requirement on flat conversion gain over the covered frequency band, and b) when the active mixers are used for upconversion. In Fig. 3.3 the output port 3 dB bandwidth performance for state-of-the-art active mixers in various technologies are shown versus the transistor unity current gain frequency f_T (left plot) and maximum frequency of oscillation f_{max} (right plot). The output port bandwidth of an active mixer is found with swept RF/IF-frequency and fixed LO-frequency. A few of the publications from the previous investigation have been left out of this figure [22,23], as these only reported the input port bandwidth performance. Instead, other publications have been included [26,27] because the performance of the output port in these active mixers were optimized for wideband operation.

A poor correlation is observed between the output port bandwidth and the f_T of the devices in the various technologies. With a few exceptions, a tendency for higher output port bandwidth with higher device f_{max} is observed. It is interesting to notice that wideband operation on the output port seems difficult to achieve with active mixers based on the Gilbert Cell mixer topology.

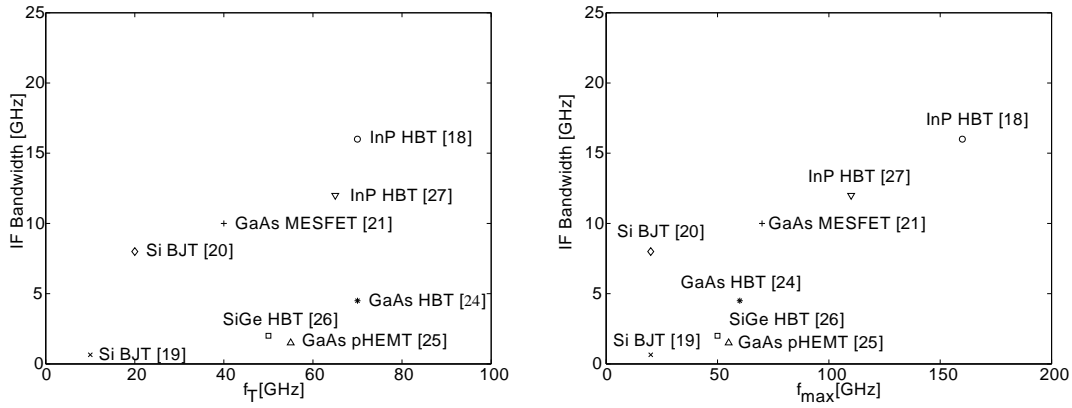


Figure 3.3 Output port bandwidth performance for state-of-the-art wideband active mixers. Left: Output port bandwidth versus unity current gain frequency f_T . Right: Output port bandwidth versus maximum frequency of oscillation f_{max} . All results for the output port bandwidth are stated for swept RF/IF-frequencies and a fixed LO-frequency.

The previous investigations have shown that in order to achieve input port 3 dB bandwidths above 10 GHz in active mixers, heterojunction transistor technologies should be used due to the high f_T offered by the devices in these technologies. With respect to the output port, bandwidths above 10 GHz have only been reported in InP HBT technology [18, 27] using devices with f_{max} above 100 GHz. The impressive 8 GHz 3 dB output port bandwidth reported in a 20 GHz f_{max} Si BJT technology [20], however, shows that such high device f_{max} is not necessary in order to get wideband operation at the output port of the active mixer. Based on the preceeding investigation of state-of-the-art wideband active mixers, a $0.8\mu\text{m}$ 35 GHz f_T SiGe HBT-BiCMOS technology was found suitable in order to implement the designs for the quadrature modulator/demodulator subsystem. Involved in the considerations for this choice have been the excellent low-frequency and broadband noise properties offered in SiGe HBT technology, as well as the possibility for low-cost prototyping in small quantities. Furthermore it seems like active mixers based on Si BJT technologies have performed very well in the past taking the relative low f_T/f_{max} device performance into account. At last it should be mentioned that the high density of integration offered in SiGe HBT technology is beneficial for reducing chip area, and hence cost in the quadrature modulator/demodulator subsystems. The estimated 3 dB bandwidth requirements for the C/X-band SAR system were not met with a Gilbert-Cell active mixer in any of the technologies discussed in the previous investigation. Taking the possibility of applying compensation techniques into account, a $0.2\mu\text{m}$ 63 GHz f_T GaAs pHEMT technology was chosen for the MMIC designs in the RF up/downconverter subsystems. Again, the possibility of low-cost prototyping in small quantities have been among the main considerations for this choice.

3.2 SiGe HBT Technology

The $0.8\mu\text{m}$ 35 GHz f_T SiGe HBT-BiCMOS BYR process [28] from Austria Mikro Systeme International AG (AMS) was chosen for the implementation of the quadrature modulator and demodulator designs. The key specifications for this process are given in Table 3.1 below. State-of-the-art SiGe HBT technologies achieved typical f_T/f_{max} values around 60 GHz back

Element	Characteristics
SiGe HBT	$f_T = 35 \text{ GHz}$, $f_{max} = 30 \text{ GHz}$ and $NF = 1.4\text{dB}@2 \text{ GHz}$
CMOS	$L_{eff} = 0.66\mu\text{m}$
Poly/Poly Capacitors	$1.77 \text{ fF}/\mu\text{m}^2$
Poly2 resistor	$75\Omega/\square$
Bpoly resistor	$170\Omega/\square$
High resistive poly2	$1.2\text{K}\Omega/\square$
Metal Layers	2
Spiral Inductor	$L = 1.8\text{nH}$ with $Q = 5.8@2 \text{ GHz}$

Table 3.1 Key Specification for the $0.8\mu\text{m}$ SiGe HBT-BiCMOS BYR Process from AMS [28, 29].

in 1999 [30, 31] when the technological considerations for the SAR++ system were initiated. Recent reported SiGe HBT technologies aiming at 40 Gbit/s optical communication achieve typical f_T/f_{max} performance of 140/183 GHz [32]. Compared with these state-of-the-art SiGe HBT technologies, the potential for wideband circuit design in AMS's SiGe HBT technology is clearly non-optimal. It is, however, believed to be sufficient for the quadrature modulator/demodulator SiGe HBT MMIC's for the SAR++ system.

In Fig. 3.4, a schematic cross-section of a typical SiGe HBT device is shown. The SiGe HBT device has a self-aligned structure with Si-poly contacts on silicon-dioxide which greatly reduces parasitic capacitances. Highly-doped poly-Si with resulting low resistance are used to contact the narrow emitter. Base-poly is used to provide a low impedance connection to the internal base region. The SiGe base layer is epitaxially deposited forming a Si-SiGe heterojunction at the base-emitter and base-collector junctions.

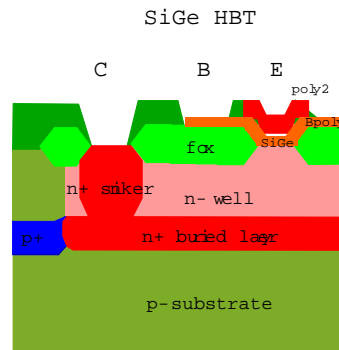


Figure 3.4 Schematic cross-section of a double-poly SiGe HBT device in the BYR process (From [29]).

3.2.1 DC Characteristics

The basic idea behind a heterojunction bipolar transistor is to introduce a large bandgap emitter relative to the base in order to reduce the reverse injected base current and thus decouple

the maximum current gain β in the transistor from the emitter to base doping ratio [33]. The ability to change the emitter and base doping levels without degrading the current gain β is advantageous in several ways, as described below

- lower emitter doping reduces the zero bias base-emitter depletion capacitance C_{je} , giving high f_T at low currents
- higher base doping reduces base sheet resistance, giving higher f_{max}
- reduced base width modulation (the Early effect) allows higher collector doping, increasing the current handling capability by delaying the onset of the Kirk effect [34].

The addition of Ge to the Si base reduces the bandgap relative to pure silicon, creating an n-Si/p-SiGe emitter-base heterojunction and a p-SiGe/n-Si collector-base heterojunction. It turns out, however, that there is a limited amount of Ge allowed in order to assure the SiGe film stability during manufacturing [31]. The limited amount of Ge means that the band offsets in the Si/SiGe heterojunctions are very small, and the full set of advantages discussed above are not easily obtained. Instead, SiGe HBT devices often use a graded-base profile as shown in Fig. 3.5 where the Ge contents in the base is increased linearly from the emitter-base junction to the collector-base junction. The graded-base SiGe HBT energy band diagram is compared to that of a standard Si BJT and shows a finite band offset $\Delta E_{g,Ge}(x=0)$ at the emitter-base junction and a larger band offset $\Delta E_{g,Ge}(x=W_b)$ at the collector-base junction. The consequences of introducing Ge into the base on the DC characteristics for the SiGe HBT can be expressed in terms of these band offsets. First the influence of the current gain β on the Ge-induced band

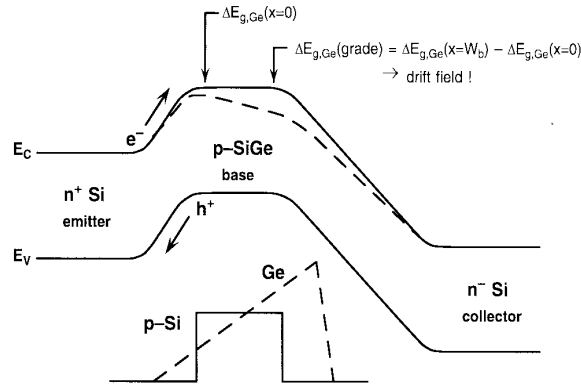


Figure 3.5 Energy band diagram for Si BJT and graded-base SiGe HBT Bipolar (From [31]).

offsets in a graded-base SiGe HBT is found to be [33]

$$\beta \propto \frac{N_e}{P_b} e^{\Delta E_{g,Ge}(x=0)/kT} \Delta E_{g,Ge}(grade)/kT \quad (3.1)$$

where N_e is the emitter doping, P_b is the base doping and $\Delta E_{g,Ge}(grade) = \Delta E_{g,Ge}(W_b) - \Delta E_{g,Ge}(0)$ is called the bandgap grading term. This equation shows that the enhancement in β depends exponentially on the emitter-base junction band offset and linearly on the bandgap grading term. The exponential dependence of the emitter-base junction band offset is caused by Ge-induced barrier lowering for electron injection from the emitter into the base, while the current injection from the base into the emitter is unaffected. Even in the case of a triangular graded-base profile with zero band offset at the emitter-base junction, the current gain is enhanced slightly due to the bandgap grading term. In applications which do not require large

values of β , it can be traded off for increased base doping, P_b , in order to reduce the base resistance. This in turn gives higher f_{max} and better broadband noise performance [31]. The dc value of β cannot be too low, however, as it determines the noise figure at low frequencies [35]. Another benefit of the Ge-induced band offsets in a graded-base SiGe HBT is an increasing Early voltage, depending exponentially on the bandgap grading term. This in turn gives an enhancement in the output conductance of the devices.

The verification of the DC characteristics for the SiGe HBT devices in the $0.8\mu m$ process from AMS has been performed using a HP 4145A Semiconductor parameter analyzer. In Fig. 3.6 the measured forward Gummel and forward beta characteristics are compared with the design kit model response for the $4 \times 0.8\mu m^2$ SiGe HBT device. The measured forward Gummel characteristic is reasonably well predicted by the design-kit model except at very low voltages, where a difference exists in the non-ideal component of the base current. The measured forward beta is slightly lower than predicted from the design-kit model. This might be explained by the fact that the forward beta parameter is sensitive to process spreadings. The measured forward

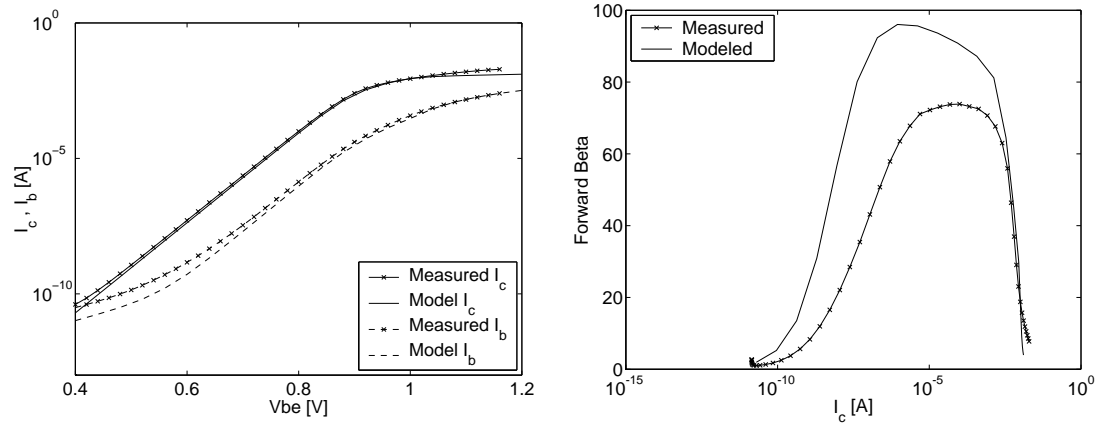


Figure 3.6 Measured and modeled forward characteristics for $4 \times 0.8\mu m^2$ area SiGe HBT device. Left: Forward Gummel plot. Right: Forward beta.

output characteristic for the $4 \times 0.8\mu m^2$ area SiGe HBT device is compared with the prediction from the design-kit model in Fig. 3.7. The collector currents follow soft curves versus the collector-emitter voltages, indicating that quasi-saturation is modeled in the design-kit model. The modeling of the slope in the collector current versus collector-emitter voltage curve at high collector currents, however, is exaggerated in the design-kit model. In general, reasonably good agreements exist between the measured and predicted DC characteristics for the $4 \times 0.8\mu m^2$ area SiGe HBT device using the design kit model based on the VBIC95 large signal model.

3.2.2 RF Performance Verification

The benefits of the Ge-induced bandoffset on the frequency response of a graded-base SiGe HBT is most easily illustrated in term of the expression for the unity current gain frequency f_T given by [36]

$$f_T = \frac{1}{2\pi} \left\{ \frac{kT}{qI_c} (C_{be} + C_{bc}) + \tau_b + \tau_e + \tau_c \right\}^{-1} \quad (3.2)$$

where I_c is the collector current, C_{be} the base-emitter depletion capacitance, C_{bc} the collector-base depletion capacitance, and τ_b , τ_e , and τ_c are the base, emitter and collector transit times respectively. The energy band offset grading across the base region leads to a drift-field which

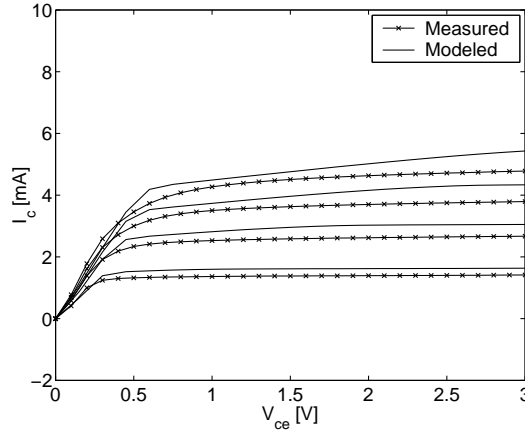


Figure 3.7 Measured and modeled forward output characteristics for $4 \times 0.8 \mu\text{m}^2$ area SiGe HBT device.

accelerates the electrons injected from the emitter to the collector, thereby decreasing the base transit time compared to a traditional Si BJT. The enhancement in beta caused by the Ge-induced band offset also leads to a lower emitter transit time [36]. In modern Si BJT's the total transit time from emitter to collector (and therefore the maximum f_T) depends mainly on the base and collector transit times [31]. In order to achieve the full benefit of the lower base transit time offered in grade-base SiGe HBT devices, it is important to minimize the collector transit time. This is achieved by increasing the collector doping which incidentally also improves the frequency response by delaying the onset of the Kirk effect [34]. Increasing the collector doping, however, decreases the breakdown voltage BV_{ceo} , and there exist a trade off between f_T and the breakdown voltage BV_{ceo} . In general, a high f_T value is achieved even at low current levels, which is in fact the main reason for the recent interest in SiGe HBT technology for wireless applications where the peak f_T performance may be traded for decreased power consumption [37].

It is often stated that the the maximum frequency of oscillation f_{max} is a more relevant figure-of-merit for RF and microwave applications than the unity-current gain frequency f_T because this only describes the vertical structure of the transistor whereas f_{max} also include parasitics. The effect on f_{max} of using a graded-base SiGe HBT device is best illustrated with the expression [31]

$$f_{max} = \sqrt{\frac{f_T}{8\pi C_{cb} R_{bb}}} \quad (3.3)$$

where C_{cb} and R_{bb} are the total collector-base capacitance and total base resistance respectively. Both the increase in unity current gain frequency f_T and the possibility of lowering the base resistance by increased base doping offered by graded-base SiGe HBT devices tend to increase f_{max} . On the other hand, the total collector-base capacitance depends on the collector doping level and the transistor architecture used and should therefore be the same as for a similar constructed Si BJT.

High frequency S-parameters measurement have been performed on various test transistor structures in the $0.8 \mu\text{m}$ SiGe HBT process from AMS in order to investigate the accuracy of the design-kit model provided for the microwave simulator Advanced Design System (ADS) from Agilent. The transistors were measured on-wafer using a HP8510B Network Analyzer in the frequency range from 45 MHz to 26.5 GHz (For details on the experimental setup including de-embedding of pad and interconnect line parasitics refer to chapter 4 of this thesis). The measured bias dependence for the unity-current gain frequency f_T in the $0.8 \mu\text{m}$ SiGe HBT process from AMS is compared to the results for the design-kit model in Fig. 3.8 for two SiGe HBT

devices with different emitter area. The f_T is extracted from measurements, de-embedded from pads and interconnect lines parasitics, as

$$f_T = h_{21} f_{meas} \quad (3.4)$$

where f_{meas} is taken in the region where the current gain with shorted output h_{21} falls with 20 dB/decade [35]. As expected from Eq. 3.2, f_T shows a linearly increasing value at small current levels where the first term dominates, achieves a peak value of $f_T \approx \frac{1}{2\pi}(\tau_b + \tau_c)^{-1}$ at medium current levels, and finally a high-current fall-off due to base-widening effect (the Kirk effect). The peak value of $f_T \approx 26$ GHz is extracted from measurement while corresponding values for the design-kit model are $f_T \approx 30$ GHz and $f_T \approx 22$ GHz for typical and worst-case process corners respectively. The worst-case process corner corresponds to the case with both low beta and low speed. The maximum frequency of oscillation is the frequency where the

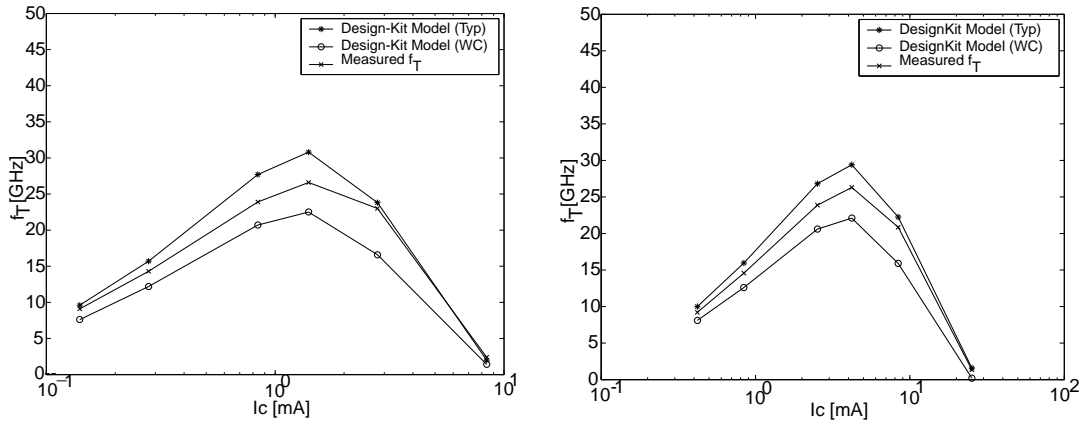


Figure 3.8 Bias dependence of unity current gain frequency f_T for two $0.8\mu\text{m}$ SiGe HBT devices with different emitter areas. Left: Emitter area $4 \times 0.8\mu\text{m}^2$. Right: Emitter area $2 \times 6 \times 0.8\mu\text{m}^2$.

transistor turns passive and can be extracted from the maximum available gain G_{max} in the frequency range where the transistor is unconditionally stable [38]. Thus in the frequency range where the stability factor $K_{stab} > 1$, the maximum frequency of oscillation is extracted from measurements, de-embedded from pad and interconnect line parasitics, as [38, 39]

$$f_{max} = \sqrt{G_{max}} f_{meas} = \sqrt{\left| \frac{Y_{21}}{Y_{12}} \right| (K_{stab} - \sqrt{K_{stab}^2 - 1})} f_{meas} \quad (3.5)$$

where f_{meas} must be in the range where G_{max} falls with 20dB/decade. In Fig. 3.9 the bias dependence for the maximum frequency of oscillation f_{max} extracted from measurement is compared with the results extracted from the design-kit model. A value of $f_{max} \approx 28$ GHz is extracted from measurement while the corresponding value for the design-kit model is $f_{max} \approx 35$ GHz and $f_{max} \approx 22$ GHz for the typical and worst-case process corners. In Fig. 3.10 the magnitude and phase of the measured de-embedded S-parameters for a $4 \times 0.8\mu\text{m}^2$ area SiGe HBT device biased at $V_{ce}=1.5\text{V}$, $I_c=1.4\text{mA}$ are compared with the design-kit frequency response. The fall-off frequencies for the magnitude of S_{11} and S_{21} are well predicted by the design-kit model which is important because this fall-off is mainly determined by the transistor input bandwidth. At frequencies above 5 GHz the phase of S_{11} starts to deviate from the measurements, however, which may be due to inaccuracy in the modeling of the distributed base region in the transistor. The magnitude and phase of S_{12} , describing the feedback in the device, are accurately predicted

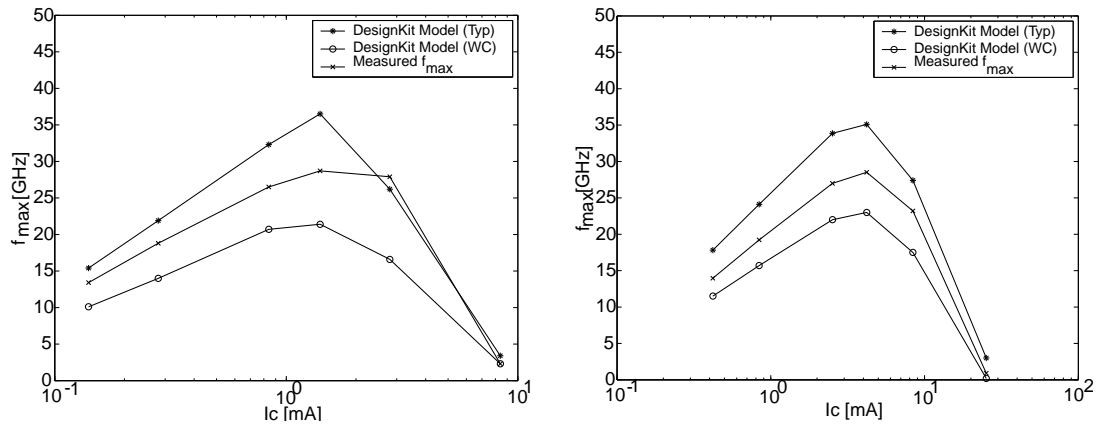


Figure 3.9 Bias dependence of maximum frequency of oscillation f_{max} for two $0.8\mu\text{m}$ SiGe HBT devices with different emitter areas. Left: Emitter area $4 \times 0.8\mu\text{m}^2$. Right: Emitter area $2 \times 6 \times 0.8\mu\text{m}^2$.

by the design-kit model in the full frequency range. The magnitude and phase of S_{22} starts to deviate at frequencies around a few GHz. This is critical as the magnitude and phase of S_{22} depends to a large extent on the collector to substrate capacitance and substrate parasitic modeling which are important parasitics for the bandwidth estimation in circuits such as wideband active mixers. In Fig. 3.11 the magnitude and phase for the measured de-embedded S-parameters for a $2 \times 6 \times 0.8\mu\text{m}^2$ area SiGe HBT device biased at $V_{ce}=1.5\text{V}$, $I_c=4.2\text{mA}$ are compared with the design-kit frequency response. As for the smaller size SiGe HBT, the fall-off frequencies for the magnitude of both S_{11} and S_{21} are accurately determined, whereas the phase response of S_{11} deviates already at frequencies above a few GHz. The same apply to the magnitude and phase of S_{12} and S_{22} , describing the feedback in the device and substrate parasitics respectively. Again it is believed that inaccurate modeling of the distributed base region is the reason for the deviation in both S_{12} and the phase in S_{11} . The measured S-parameters on transistor test structures show large qualitative differences compared with the frequency responses for the design-kit models, which is caused by improper modeling of the parasitics around the intrinsic SiGe HBT device. This inaccuracy in parasitics modeling is unacceptable for successful microwave integrated circuit design in wideband SAR applications. Therefore the next chapter is devoted to accurate high-frequency modeling of devices and basic circuit configurations in the $0.8\mu\text{m}$ SiGe HBT process from AMS.

3.3 GaAs pHEMT Technology

The $0.2\mu\text{m}$, 63 GHz f_T GaAs pHEMT ED02AH process from OMMIC was chosen for the implementation of the RF up/downconverter MMIC designs. The ED02AH process is intended for microwave applications up to millimeter wave frequencies. Both depletion and enhancement mode transistors are available for design. In addition to the active devices, the ED02AH process offers high quality inductors, capacitors, resistors, via holes and air bridges. The key specifications for the ED02AH process are given in Table 3.2. Furthermore it should be mentioned that measured results on a 1.5nH spiral inductor in the ED02AH process demonstrated a 16 GHz self-resonance frequency. This makes compensation techniques using spiral inductors interesting for wideband SAR applications at X-band frequencies and below.

A schematic cross-section of a conventional GaAs HEMT device is shown in Fig. 3.12. A

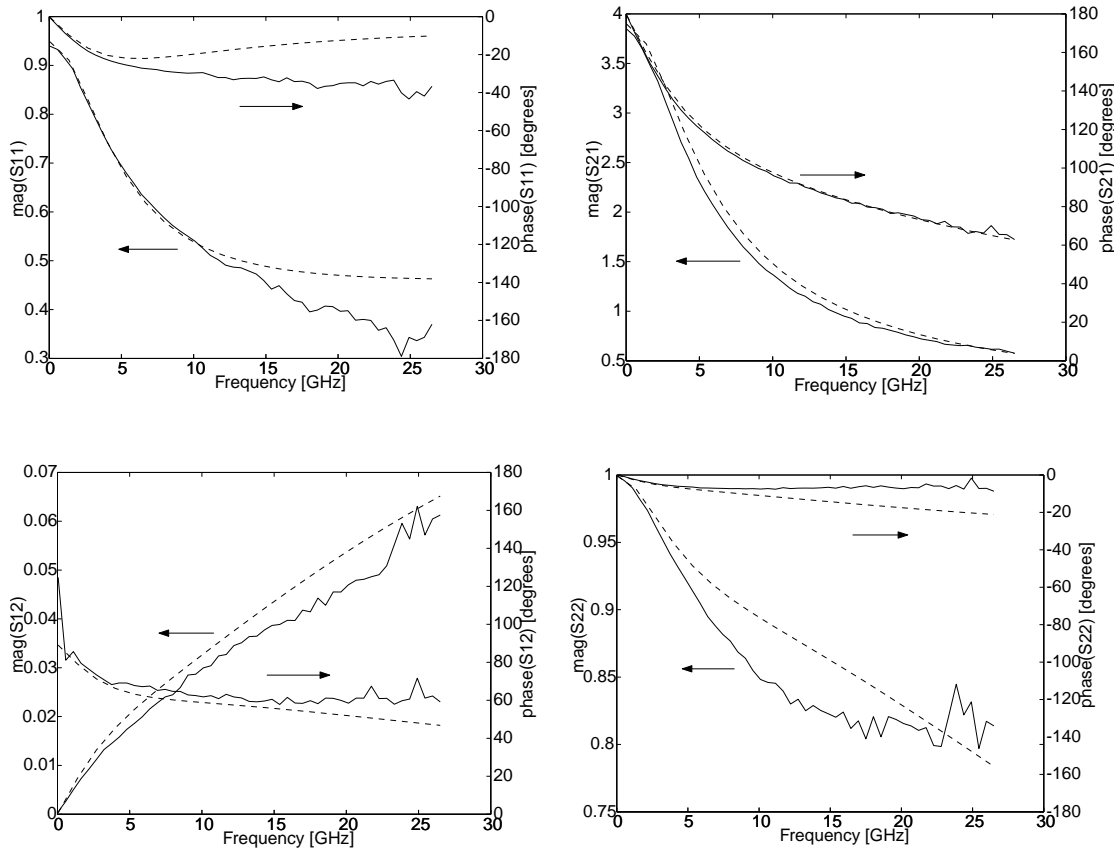


Figure 3.10 Frequency dependence for S-parameters for $4 \times 0.8 \mu\text{m}^2$ area SiGe HBT device biased at $V_{ce} = 1.5\text{V}$, $I_c = 1.4\text{mA}$. Solid and dashed lines represent measured and design kit model frequency response respectively.

Element	Characteristics
pHEMT	$f_T = 63\text{ GHz}$, $NF = 0.9\text{dB}@12\text{ GHz}$
Spiral Inductor*	$L = 1.5\text{nH}$ with $Q = 8@12\text{ GHz}$

Table 3.2 Key Specification for the $0.2\mu\text{m}$ GaAs pHEMT ED02AH Process from OM-MIC [40](* Based on measured results).

heterojunction interface is created at the layer of undoped GaAs and the n-doped AlGaAs. The electrons in the n-doped AlGaAs layer may become trapped at the heterojunction interface. These trapped electrons accumulate in a thin sheet at the heterojunction interface, also known as the two dimensional (2D) electron gas [41]. The density of trapped electrons is controlled by the applied gate voltage. A more positive gate voltage increases the electron density and therefore the drain-source channel current. Because of the undoped GaAs layer, the ionised impurity scattering is reduced. As a result, the mobility for the electrons in the two dimensional electron gas is enhanced, hence the name High Electron Mobility Transistor. The practical consequences of the high electron mobility are high unity current gain frequency f_T , high gain, and low noise. Conventional HEMT devices suffer from low current drive capabilities caused by the small conduction band offset at the GaAs/AlGaAs heterojunction. In a pseudomorphic HEMT (pHEMT) device an AlGaAs/InGaAs heterojunction interface is grown on GaAs. The confinement of the electrons in the channel in the pHEMT is better leading to better performance than in the conventional HEMT [41].

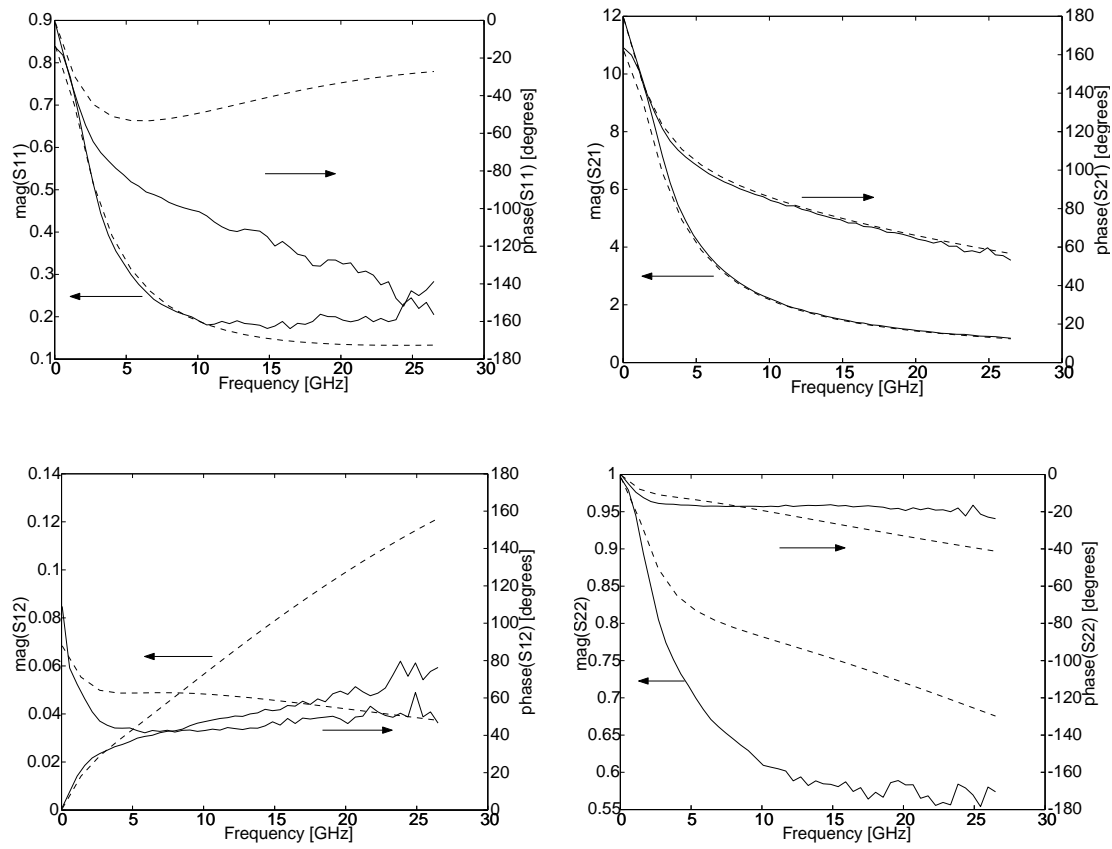


Figure 3.11 Frequency dependence for reverse S-parameters for $2 \times 6 \times 0.8 \mu\text{m}^2$ SiGe HBT biased at $V_{ce} = 1.5\text{V}$, $I_c = 4.2\text{mA}$. Solid and dashed lines represent measured and design kit model frequency response respectively.

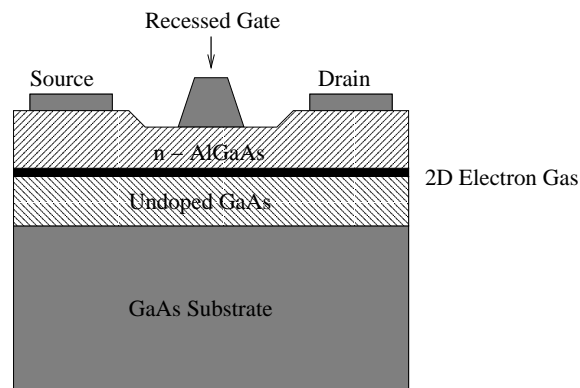


Figure 3.12 Schematic cross-section of a conventional GaAs HEMT device.

Chapter 4

Substrate Effects in SiGe HBT Technology

Advanced Si/SiGe bipolar technologies makes use of a high-resistivity (p^-) substrate with a typical resistivity of $20\Omega - cm$. In Si-based monolithic microwave integrated circuits (MMICs) this results in a significant high-frequency loading of circuit nodes involving both transistors and passive elements. The nonzero dielectric constant and the conductivity of the Si-substrate may also lead to unwanted coupling between components that otherwise are supposed to operate independently. Equivalent circuit models suitable for predicting the loading due to substrate effects have been presented in [42, 43] while substrate coupling effects have been discussed in [44–46]. In the past, however, investigations of the influence of substrate effect in actually circuit designs have been mainly limited to mixed-signal circuits [47], and low-noise amplifiers (LNA's) [48]. The influence of substrate effects on the frequency response of SiGe HBT wide-band MMICs is not obvious. In order to investigate this influence, a combined experimental and simulation study is performed on basic circuit configurations. Especially the frequency response of a differential amplifier stage, often used in integrated circuit design will serve as a canonical example for the present discussion. The experimental part of the study consist of extracting suitable equivalent circuit models from fabricated test structures. These equivalent circuit models are then used in the simulation of the differential amplifier stage to investigate the influence on the frequency response.

First, an accurate high-frequency small-signal model including the parasitic elements associated with the SiGe HBT device structure in the $0.8\mu m$ SiGe HBT process from AMS is found using a direct parameter extraction method. The applicability of the direct parameter extraction method for VBIC95 large signal modeling is shown.

The study of substrate effects in basic circuit configurations consist of an investigation of the importance of various parasitics on the frequency response of a SiGe HBT differential amplifier. The extraction of equivalent circuit models for the pad structure, interconnect lines and poly resistors from fabricated test structures in the $0.8\mu m$ SiGe HBT process from AMS is described. Specially the importance of SiGe HBT device parasitics and substrate parasitics associated with pad structures, interconnect lines, and poly resistors for matching simulations to experimental results will be discussed.

4.1 Substrate Effects in SiGe HBT Modeling

Accurate modeling of parasitics associated with the individual transistors is a prerequisite to achieve wideband operation. As the frequency of operation increases, the influence from parasitic substrate effects becomes more important and must be accurately accounted for in the modeling of the SiGe HBTs. Existing methods for substrate parasitic extraction relies on either numerical optimization techniques [49, 50], or cumbersome numerical simulation with requirement on process information often not available [43]. It is well-known that numerical optimization techniques may lead to extracted elements values which depends on the starting value and may be non-physical [51]. Thus in recent years a trend toward direct parameter extraction methods for the small-signal equivalent circuit of bipolar devices have been observed [51–56]. Most of these paper have been concerned with parameter extraction for GaAs HBTs where the substrate have no direct effect on the performance. Direct parameter extraction methods have been reported for Si BJT [52] and SiGe HBTs [56], however substrate effects were not taken into account in these methods.

Here a direct extraction method for SiGe HBTs is described. Unlike previous reported extraction methods, the method presented here can be used to determined the elements associated with the parasitic transistor action. The method uses a multi-step deembedding approach and requires knowledge of the measured S-parameters for the SiGe HBT biased in forward active, cut-off and saturated regions. The applicability of the extraction procedure for VBIC95 large-signal model parameter extraction is discussed and the performance is experimentally verified in the frequency range from 45 MHz-26.5 GHz.

4.1.1 Deembedding of Pad and Interconnect Line Parasitics

For characterizing high-frequency devices on Si-substrates by on-wafer measurements, it is generally preferred to use an Impedance Substrate Standard (ISS) followed by de-embedding of parasitics from the test-fixture [57]. For successful parameter extraction of SiGe HBTs it is essential that an accurate deembedding procedure is applied to remove the influence from pads and interconnect lines. For this purpose, the methods reported in [58–60] have traditionally been used. These methods differs in terms of complexity, accuracy and number of on-wafer standards required. All existing de-embedding methods rely on a physical interpretation of the parasitics associated with pads and interconnect lines. The accuracy depends upon the extent that the physical interpretation for a given de-embedding method is fulfilled in the design of the experiment.

The layout of the test-structure including the SiGe HBT devices is seen in Fig. 4.1. The devices under investigation are a single-emitter SiGe HBT with area $4 \times 0.8 \mu\text{m}^2$, and a double-emitter SiGe HBT with area $2 \times 6 \times 0.8 \mu\text{m}^2$ fabricated in the $0.8 \mu\text{m}$ SiGe HBT process from AMS. The ground-shielded pad configuration uses an n^+ -layer underneath the signal pad. The potential of the substrate is tied to ground with a p^+ -guard ring around the devices. The emitter is connected together with the substrate and have a low-impedance connection to RF-ground. All on-wafer high-frequency measurements (45 MHz-26.5 GHz) were performed using a HP8510B network analyzer calibrated up to the probe tips by an ISS calibration substrate. Cascade GSG probes were used to contact the test structures on the chips.

The general equivalent circuit representation for the test-structure with a ground-shielded pad configuration is shown in Fig. 4.2. The coupling from the pads to the shield is represented as a shunt admittance Y_{ps} , and the shield conductance due to nonzero resistivity of the ground-shield is represented as the admittances Y_s . The loading from the interconnect lines is here absorbed in the shunt admittances Y_{bs} and Y_{cs} connected across the base-emitter and collector-

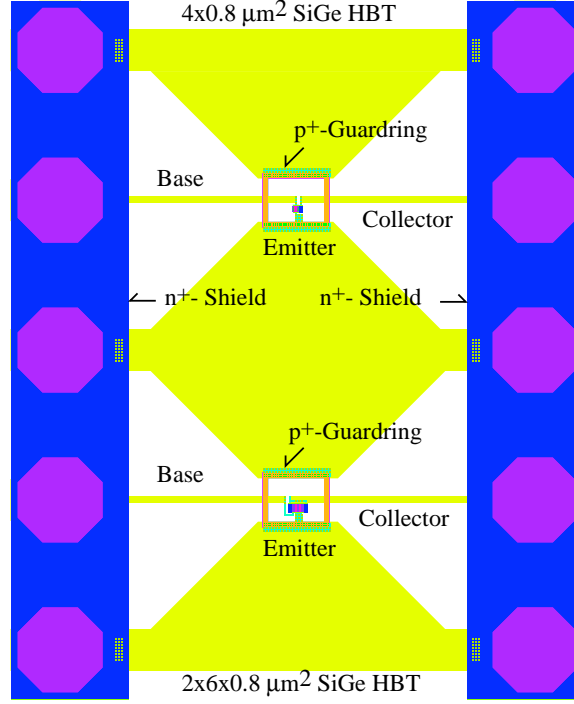


Figure 4.1 The layout of the SiGe HBT test devices with single and double-emitters.

emitter terminals of the SiGe HBT device. A shunt admittance Y_{bc} is connected across the base-collector terminals of the SiGe HBT. The use of a ground-shielded pad configuration ideally

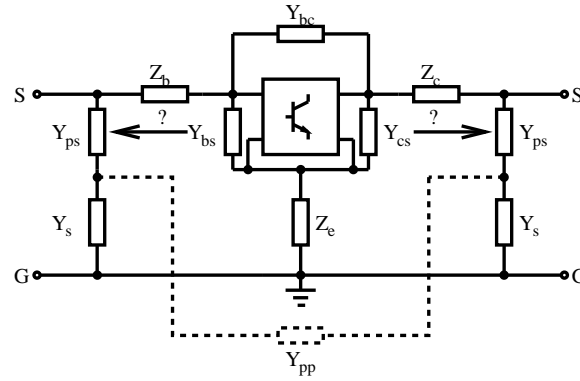


Figure 4.2 Equivalent circuit representation of SiGe HBT with ground shielded pads.

prevent coupling between the input and output pads through the substrate [61]. As a result, the coupling admittance Y_{pp} can in some cases be left out of consideration. In Fig. 4.3 the measured coupling between input and output pads in a simple open structure without interconnect lines, and an open structure with interconnect lines all the way up to the (removed) device under test are compared. As expected, it is observed that the ground shielded pad configuration results in very small coupling for the open structure without lines. The open structure with lines shows that a significant part of the coupling is due to the small gap between the lines where the device under test is to be placed. Therefore both the neglect of the substrate coupling admittance Y_{pp} , and the placement of Y_{bc} between the base-collector terminals of the SiGe HBT in Fig. 4.2 seems to be justified. The question remains whether the placement of the loading due to the interconnect lines across the SiGe HBT device terminals is valid, or it is more correct to place all of this loading at the pads, as assumed by the three-step de-embedding method

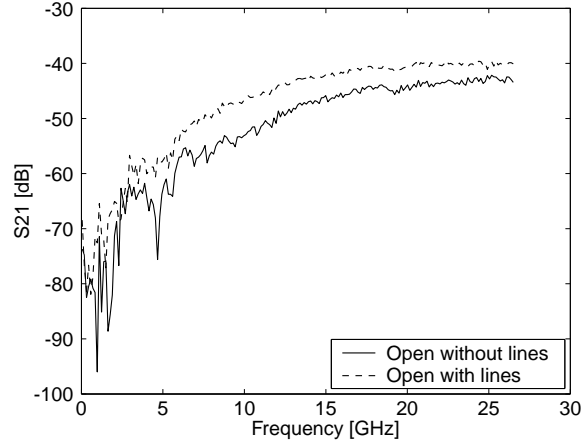


Figure 4.3 Measured coupling between ground-shielded pads with and without interconnect lines.

described in [60]. In order to investigate the influence of the placement of the parasitics from the interconnect lines, two different de-embedding method were applied to measured S-parameter on the single-emitter SiGe HBT device. In the variant described below of the distributed method reported in [59] (The Koolen de-embedding method) the shunt parasitics are all placed across the transistor terminals, and the de-embedded Y-parameters for the device are found in three steps as follows. First, the measured Y-parameters, Y_{meas} , are de-embedded from pad parasitics as

$$Y_{d1} = Y_{meas} - Y_{pad} \quad (4.1)$$

where Y_{pad} are the measured Y-parameters for an open standard without lines. Next, the measured Y-parameters de-embedded for pad parasitics are converted into Z-parameters and the series parasitics Z_b , Z_e , and Z_c are subtracted as

$$Y_{d2} = (Y_{d1}^{-1} - (Y_{short} - Y_{pad})^{-1})^{-1} \quad (4.2)$$

where Y_{short} are the measured Y-parameters for a short standard. The last step is to subtract the parallel parasitics Y_{bs} and Y_{cs} due to the interconnect lines as

$$Y_{d3} = (Y_{d2} - ((Y_{open} - Y_{pad})^{-1} - (Y_{short} - Y_{pad})^{-1})^{-1}) \quad (4.3)$$

where Y_{open} are the measured Y-parameters for an open standard with the device under test removed. This de-embedding method requires three standards, an open without lines, an open with lines, and a short standard. In the method reported in [60] (The Cho-Burk de-embedding method) the parasitics from pads and interconnect lines are de-embedded in three-steps. In this method, the shunt parasitics due to pads and interconnect lines are first subtracted from the measured Y-parameters as

$$Y_{d1} = Y_{meas} - \begin{bmatrix} Y_{11open} + Y_{12open} & 0 \\ 0 & Y_{22open} + Y_{12open} \end{bmatrix} \quad (4.4)$$

where Y_{open} are the measured Y-parameters for the open standard with lines. Then the series parasitics due to the interconnect lines are de-embedded as

$$Y_{d2} = \left(Y_{d1}^{-1} - \left(Y_{short} - \begin{bmatrix} Y_{11open} + Y_{12open} & 0 \\ 0 & Y_{22open} + Y_{12open} \end{bmatrix} \right)^{-1} \right)^{-1} \quad (4.5)$$

where Y_{short} are the measured Y-parameters for the short standard with all lines connected together. The last step is to subtract the shunt element across the input and output lines as

$$Y_{d3} = Y_{d2} - \begin{bmatrix} Y_{12open} & -Y_{12open} \\ -Y_{12open} & Y_{12open} \end{bmatrix}. \quad (4.6)$$

The variant of the Cho-Burk de-embedding method described above uses only two standards, an open standard with lines, and a short standard with all lines connected together. The original method requires four standards, two shorts, a thru, and an open standard. In order to investigate the accuracy of the de-embedding methods described above, the base-emitter capacitance C_{be} for the parasitic substrate transistor of a $4 \times 0.8 \mu\text{m}^2$ area single-emitter SiGe HBT device is extracted using the method described in the next subsection after pad and interconnect line parasitics have been removed using each of the two de-embedding methods just described. The frequency dependence of the extracted capacitance as seen in Fig. 4.4 shows that the Cho-Burk de-embedding method is superior to the Koolen de-embedding method for extracting small-size parasitics. Therefore the Cho-Burk de-embedding method has been used for all succeeding parameter extraction on SiGe HBT devices in this work.

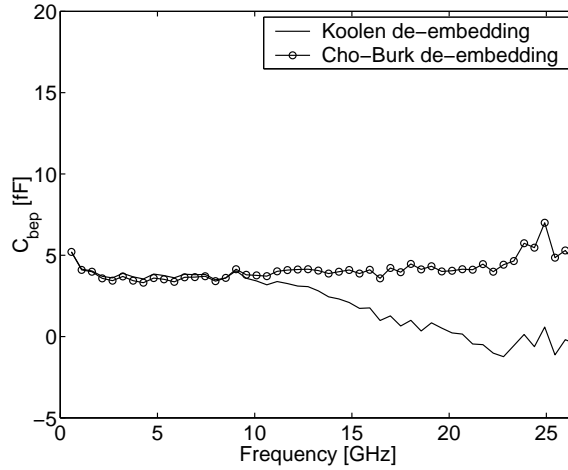


Figure 4.4 The base-emitter capacitance C_{be} for the parasitic substrate transistor of a $4 \times 0.8 \mu\text{m}^2$ area single-emitter SiGe HBT extracted from measured S-parameters using the Koolen and Cho-Burk de-embedding methods.

4.1.2 Direct Parameter Extraction Method for SiGe HBT Equivalent Circuit

Small-signal equivalent circuit models for SiGe HBT devices can naturally be divided into an intrinsic part describing the transistor action in a vertical structure underneath the emitter, and an extrinsic part due to unavoidable parasitics associated with the device structure as seen in Fig. 4.5. The intrinsic part is described with the well-known hybrid- π equivalent circuit which follows from a linearization of the Gummel-Poon large-signal model in the forward active region [62]. The transconductance g_m contains a delay component τ in order to model the excess phase shift which becomes noticeable at frequencies approaching f_T for the devices [63]. The base-emitter capacitance C_{be} contains both depletion and diffusion components, while the base-collector capacitance C_{bc} only includes the depletion components. The intrinsic base resistance R_{bi} models the current dependent part of the total base resistance, arising due to conductivity modulation of the internal base sheet resistance [64]. The reduced base-width modulation (the Early effect) experienced in SiGe HBTs means that the output conductance g_o can be neglected. As shown in Fig. 4.5, the parasitics in the extrinsic part includes fixed base, collector, and

emitter series resistances and parasitics due to substrate transistor action C_{bep} , C_{bcp} , and R_s . Furthermore, in modern double-poly SiGe HBT devices a large part of the total capacitance between base-emitter and base-collector terminals is due to fixed oxide capacitances shown in Fig. 4.5 as C_{beo} and C_{bco} respectively. The small-signal equivalent circuit model shown in Fig. 4.5 should be able to accurately describe the behavior for a SiGe HBT from DC to frequencies in excess of f_T of the devices for all current levels up to the point where base-widening effects starts to dominate the device behavior.

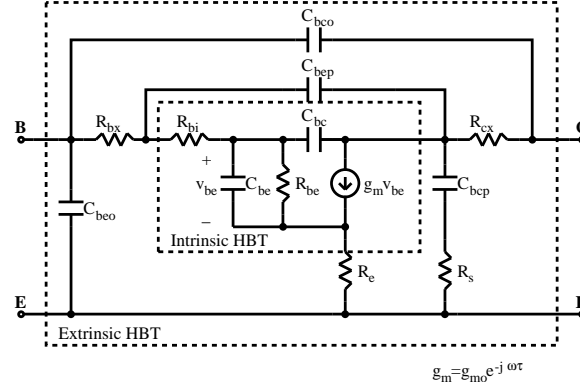


Figure 4.5 High-frequency equivalent circuit model for a double-poly SiGe HBT device in the forward active region.

Fixed Access Resistances and Fixed Oxide Capacitances

In the cut-off mode, the small-signal equivalent circuit model for a HBT consist only of capacitances and resistances [65] as shown in Fig. 4.6. In the lower frequency range, where the effects of the resistors remains negligible, the resulting capacitance network have a π -topology so that the total input capacitance C_{in} can be found as [66]

$$\omega C_{in} = \Im(Y_{11} + Y_{12}) \quad (4.7)$$

where Y_{11} and Y_{12} are measured Y-parameters de-embedded from pad and interconnect line parasitics. Similar, the total feedback capacitance C_{fb} between base and collector terminals can be found as

$$\omega C_{fb} = \Im(-Y_{12}). \quad (4.8)$$

The measured frequency dependence of the imaginary part of the above Y-parameter equation for a $2 \times 6 \times 0.8 \mu m^2$ area SiGe HBT device biased in the cut-off region are shown in Fig. 4.7 (left plot). A linear frequency dependence is observed verifying the capacitive behavior. The input capacitance C_{in} includes both the fixed oxide capacitance C_{beo} , and the voltage dependent base-emitter depletion capacitance C_{be} . Thus the input capacitance is given by

$$C_{in} = C_{beo} + \frac{C_{je}}{\left(1 - \frac{V_{be}}{P_e}\right)^{M_e}} \quad (4.9)$$

where C_{je} is the zero bias base-emitter depletion capacitance, P_e is the built-in potential for the base-emitter junction, and M_e is the base-emitter junction grading term. Extraction of C_{beo} is accomplished by fitting this equation to measured C_{in} for a reverse biased, as well as slightly forward biased base-emitter junction. The feedback capacitance C_{fb} includes both the fixed oxide capacitance C_{bco} , and the total voltage dependent base-collector depletion capacitance.

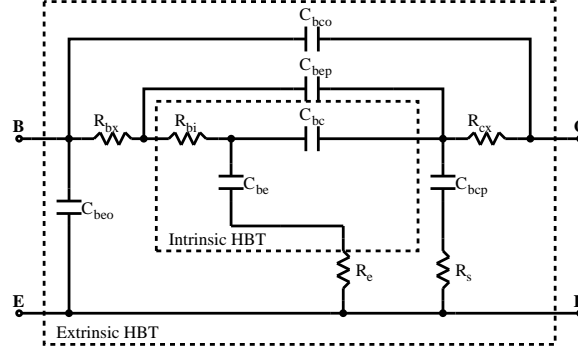


Figure 4.6 Small-signal equivalent circuit valid when the SiGe HBT is biased in cut-off mode.

The base-collector C_{bc} and parasitic base-emitter depletion capacitances C_{bep} are assumed to have the same voltage dependence, so that the feedback capacitance is written as

$$C_{fb} = C_{bco} + \frac{C_{jc} + C_{jep}}{\left(1 - \frac{V_{bc}}{P_c}\right)^{M_c}} \quad (4.10)$$

where C_{jc} and C_{jep} are the zero-bias depletion capacitances for the base-collector and parasitic base-emitter junctions respectively, while P_c is the built-in potential for the base-collector junction and M_c is the base-collector junction grading term. In Fig. 4.7 (right plot), the excel-

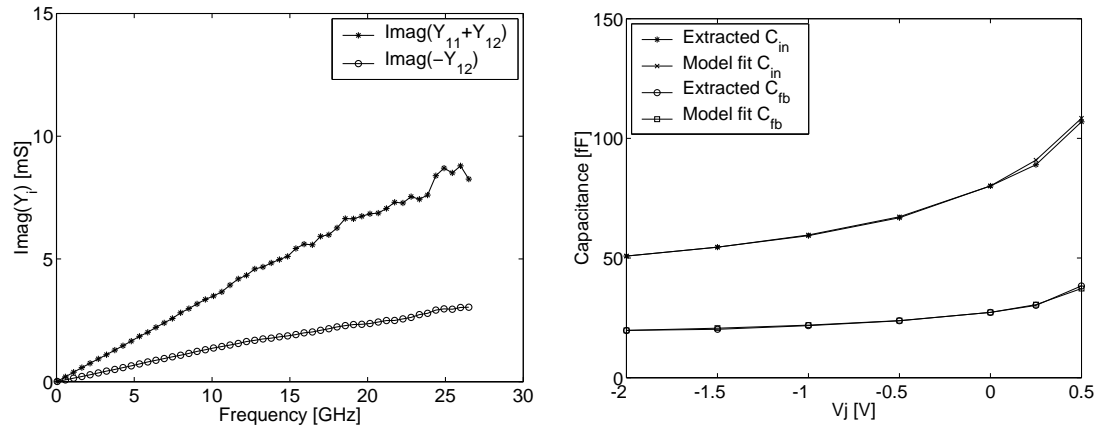


Figure 4.7 Extraction of base-emitter and base-collector junction capacitances for a $2 \times 6 \times 0.8 \mu\text{m}^2$ area SiGe HBT device. Left: The resulting frequency dependence of imaginary part of the Y-parameters in cut-off mode ($V_{be} = -1.5\text{V}$, $V_{ce} = 0.0\text{V}$). Right: Model fit for total base-emitter and base-collector capacitances using extracted values for fixed oxide and depletion capacitances.

lent model fits to measured data for the input capacitance C_{in} and feedback capacitance C_{fb} are shown using extracted values for the fixed oxide capacitances, zero bias depletion capacitances, built-in potentials and junction grading terms for the base-emitter junction and base-collector junction.

In order to find the access base, emitter, and collector resistances in bipolar transistors, the methods described in [62] have traditional been used. These methods are based on oversimplifications of the model and the extracted values must be refined by optimization. Instead, it

has been shown that a HBT biased in saturation at zero collector-emitter voltage and driven with a very large forward base current I_b can be represented with a simple T -equivalent circuit model consisting only of external base, emitter, and collector access resistances [66]. In a SiGe HBT, things are complicated by the presence of the parasitic substrate transistor which starts to conduct current in saturation. In the saturation region, a significant part of the applied base current I_b will flow in the substrate because the parasitic base-emitter junction turns on. The remaining part of the current will flow thru the forward biased emitter-base, base-collector, and parasitic base-emitter junctions. The transport current cancels internally so no current flows into the collector. Now, as the base current I_b increase toward infinity, the dynamic resistances of the base-emitter, base-collector, and parasitic base-emitter junctions decrease toward zero and a simple T -equivalent circuit consisting of the fixed base, collector, and emitter series resistances results despite the substrate conductance. At very high base currents the base, emitter, and collector resistances are given by the equations

$$R_{bx} = \Re(Z_{11} - Z_{12}) \quad (4.11)$$

$$R_e = \Re(Z_{12}) \quad (4.12)$$

$$R_{cx} = \Re(Z_{22} - Z_{12}) \quad (4.13)$$

where Z_{11} , Z_{12} and Z_{22} are measured Z-parameters de-embedded for pad and interconnect line parasitics for a SiGe HBT biased in the saturation region. The frequency dependence of the real part of the measured Z-parameter equations for a $2 \times 6 \times 0.8 \mu m^2$ area SiGe HBT device are shown in Fig. 4.8 (left plot). The flat frequency dependence verifies that all internal junction resistances short-circuits all the internal capacitances as they should. The extraction of the fixed base, emitter, and collector resistances are based on the extrapolation of the plots of the real part of the above Z-parameter equations versus $1/I_b$, up to the ordinate as illustrated in Fig. 4.8 (right plot). Only a very small part of the applied base current will actually flow through the intrinsic base resistance, explaining the observed slow variation of $\Re(Z_{11} - Z_{12})$ with base current.

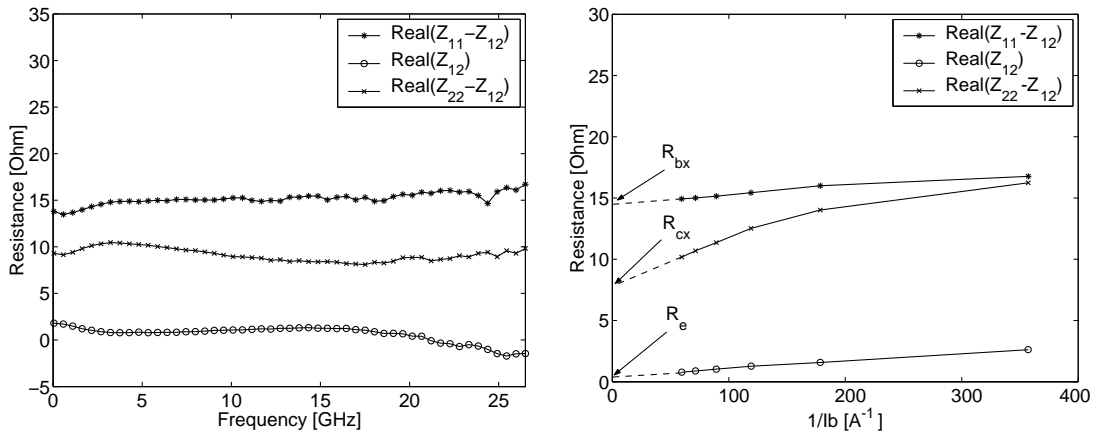


Figure 4.8 Extraction of fixed base, collector and emitter series resistances for a $2 \times 6 \times 0.8 \mu m^2$ area SiGe HBT. Left: Frequency dependence of real part of Z-parameters when the SiGe HBT is in the saturation region ($V_{ce} = 0.0V$, $I_b = 16.8mA$). Right: Evolution of the real part of the Z-parameters versus $1/I_b$.

In Table. 4.1 a summary is given of the extracted values obtained for the fixed oxide capacitances and the fixed series resistances for both the $2 \times 6 \times 0.8 \mu m^2$ area, and the $4 \times 0.8 \mu m^2$ area SiGe HBT devices.

Parameter	Extracted Value (2x6x0.8 μm^2 area)	Extracted Value (4x0.8 μm^2 area)
C_{beo} [fF]	21.26	9.54
C_{bco} [fF]	9.75	2.76
R_{bx} [Ω]	14.5	31.0
R_e [Ω]	0.7	3.0
R_{cx} [Ω]	7.5	18.0

Table 4.1 Extracted fixed oxide capacitances and fixed access resistances parameters for 2x6x0.8 μm^2 area and 4x0.8 μm^2 area SiGe HBT devices.

Substrate Parasitics Extraction

Once the fixed access resistances and fixed oxide capacitances have been extracted, it is possible to remove their influence by de-embedding. It should be noticed that the emitter resistance can not be de-embedded at this point, as the parasitic substrate network is connected to the emitter node as shown previously in Fig. 4.5. The equivalent circuit model for the SiGe HBT in the cut-off region after de-embedding can then be represented as shown in Fig. 4.9. Straightforward

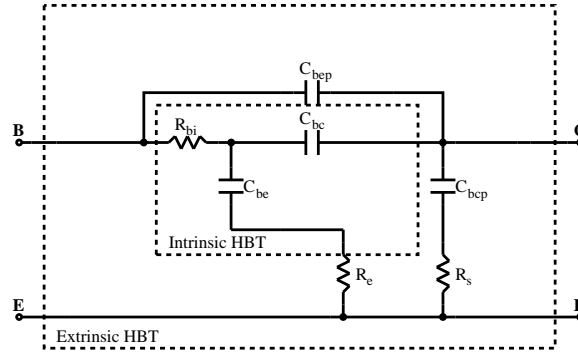


Figure 4.9 Small-signal equivalent circuit model for a SiGe HBT biased in the cut-off region after fixed oxide capacitances and fixed base and collector access resistances have been removed.

analysis on the equivalent circuit in Fig. 4.9 shows that the Y-parameters Y_{22} and Y_{12} are given by

$$Y_{22} = \frac{j\omega C_{bcp}}{1 + j\omega C_{bcp} R_s} + j\omega C_{bep} + \frac{j\omega C_{bc}(1 + j\omega C_{be} R_{bi})}{1 + j\omega(C_{be} + C_{bc}) R_{bi}} \quad (4.14)$$

and

$$Y_{12} = -j\omega C_{bep} - \frac{j\omega C_{bc}}{1 + j\omega(C_{be} + C_{bc}) R_{bi}} \quad (4.15)$$

where the influence of R_e has been neglected for simplicity. The influence of the parasitic base-emitter capacitance C_{bep} can be removed by adding the two Y-parameters together

$$\begin{aligned} Y_{22} + Y_{12} &= \frac{j\omega C_{bcp}}{1 + j\omega C_{bcp} R_s} - \frac{-\omega^2 C_{bc} C_{be} R_{bi}}{1 + j\omega(C_{be} + C_{bc}) R_{bi}} \\ &\approx \frac{j\omega C_{bcp}}{1 + j\omega C_{bcp} R_s} \end{aligned} \quad (4.16)$$

where the approximation is valid for $\omega^2 C_{bc} C_{be} R_{bi} \approx 0$, which is equivalent to neglecting the internal feedback path through the device. Thus, the substrate resistance R_s and parasitic base-

collector admittance ωC_{bcp} are extracted as follows

$$R_s = \Re \left(\frac{1}{Y_{22} + Y_{12}} \right) \quad (4.17)$$

and

$$\omega C_{bcp} = \frac{-1}{\Im \left(\frac{1}{Y_{22} + Y_{12}} \right)}. \quad (4.18)$$

The frequency dependence of the extracted substrate resistance and parasitic substrate base-collector admittance for a $2 \times 6 \times 0.8 \mu m^2$ area SiGe HBT device are shown in Fig. 4.10. At low frequencies, the extraction of the substrate resistance is inaccurate because the measured Y-parameters are dominated by capacitive effects. At high frequencies especially, the extracted parasitic base-collector capacitance shows a frequency dependence. It has been verified, by simulation on a realistic small-signal model, that this frequency dependence identify the frequency region where the approximation used for the substrate extraction becomes inaccurate. The extraction of the substrate parasitics should therefore be confined to the frequency range where the substrate resistance R_s shows flat characteristics and ωC_{bcp} depends linear on the frequency.

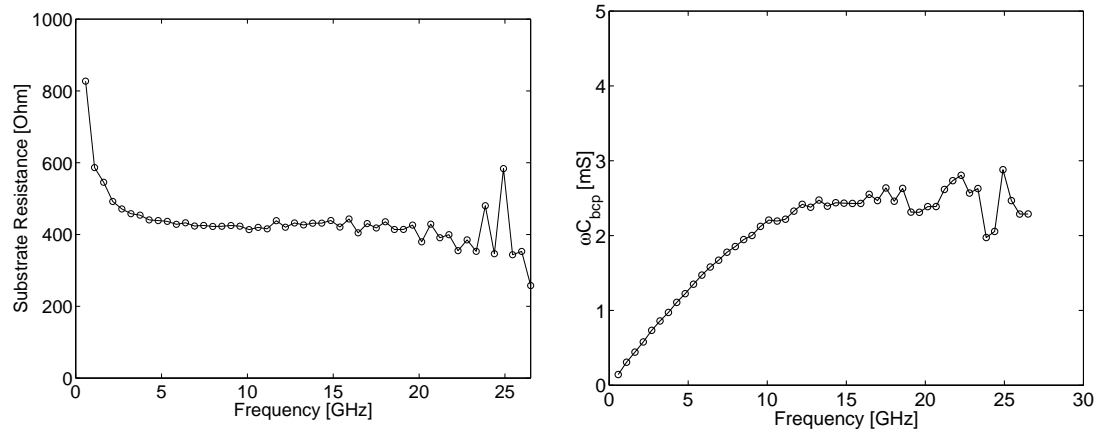


Figure 4.10 Extraction of substrate parasitics for a $2 \times 6 \times 0.8 \mu m^2$ area double-emitter SiGe HBT biased in the cut-off region ($V_{ce} = 1.5V, V_{be} = 0V$). Left: Frequency dependence of the extracted substrate resistance R_s . Right: Frequency dependence of the extracted parasitic base-collector admittance ωC_{bcp} .

The parasitic base-collector capacitance is a voltage dependent depletion capacitance described by the usual type of equation

$$C_{bcp} = \frac{C_{jcp}}{\left(1 - \frac{V_{sc}}{P_s}\right)^{M_s}} \quad (4.19)$$

where C_{jcp} is the zero bias parasitic base-collector depletion capacitance, P_s is the built-in potential for the parasitic base-collector junction, M_s is the parasitic base-collector grading term, and V_{sc} is the substrate to collector potential. In Fig. 4.11, the model fit is compared to measured parasitic base-collector capacitance C_{bcp} using extracted values for the zero bias depletion capacitance, built-in potential, and junction grading term for the parasitic base-collector junction.

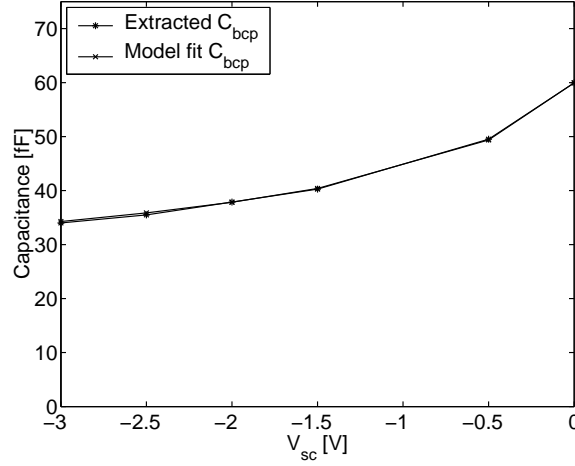


Figure 4.11 Model fit for parasitic base-collector capacitances using extracted values for the depletion capacitance

In Table. 4.2, a summary is given for the extracted values obtained for the substrate resistance R_s and parasitic base-collector capacitance C_{bcp} . The parasitic base-emitter capacitance is extracted after the elements for the intrinsic hybrid- π equivalent circuit are extracted as discussed next.

Parameter	Extracted Value ($2 \times 6 \times 0.8 \mu\text{m}^2$ area)	Extracted Value ($4 \times 0.8 \mu\text{m}^2$ area)
R_s [Ω]	428.2	965.4
C_{jcp} [fF]	59.95	34.04
P_s [V]	0.55	0.55
M_s	0.3	0.3

Table 4.2 Extracted substrate resistance R_s and parasitic base-collector junction capacitance parameters C_{jcp} , P_s and M_s for $2 \times 6 \times 0.8 \mu\text{m}^2$ area and $4 \times 0.8 \mu\text{m}^2$ area SiGe HBT devices.

Determination of Intrinsic Hybrid- π Equivalent Circuit

At this point all external elements of the small signal equivalent circuit for the SiGe HBT device have been extracted, except the parasitic base-emitter capacitance C_{bep} . It is however possible to extract the intrinsic elements of the hybrid- π equivalent circuit independently of this capacitance [56]. In order to do this, the influence from the external elements of the SiGe HBT must first be removed using the following multi-step de-embedding approach: Step 1) de-embed fixed oxide capacitances; Step 2) de-embed fixed base and collector resistances; Step 3) de-embed substrate resistance and parasitic base-collector capacitance (bias dependent); Step 4) de-embed fixed emitter resistance. The small-signal equivalent circuit model after the de-embedding procedure have been applied can be represented as shown in Fig. 4.12.

Using the multi-step de-embedding procedure described above, the complicated SiGe HBT equivalent circuit shown in Fig. 4.5 have been reduced to the simpler hybrid- π small-signal topology. The commonly used Gummel-Poon large-signal model reduces to the hybrid- π small-signal topology, when linearized and several methods exists for the parameter extraction for this circuit [51–56]. Most of the previous methods have used Z-parameters due to the distributed nature of the base network. During the parameter extraction on the SiGe HBT devices in this

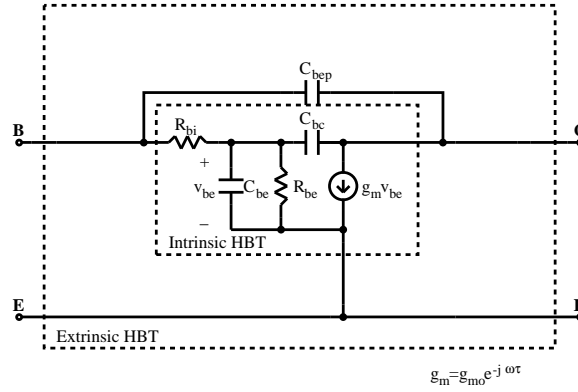


Figure 4.12 Small-signal equivalent circuit model for a SiGe HBT biased in the forward active region after fixed oxide capacitances, fixed access resistances, parasitic base-collector capacitance and parasitic substrate resistance have been removed.

work, however, methods based on Y-parameters have proven best suitable. This might be due to the small but non-negligible output conductance distorting the Z-parameters in a manner which makes certain assumptions for the parameter extraction methods unfulfilled. Now, the parameter extraction for the internal hybrid- π using the Y-parameter method reported in [56] will be described in detail, with emphasis on the verification of the assumptions in this method. Analytical expressions for the Y-parameters of the equivalent circuit shown in Fig. 4.12 are easily derived. The results are stated below

$$Y_{11} = \frac{g_{be} + j\omega(C_{be} + C_{bc})}{1 + R_{bi}(g_{be} + j\omega(C_{be} + C_{bc}))} + j\omega C_{bep} \quad (4.20)$$

$$Y_{12} = \frac{-j\omega C_{bc}}{1 + R_{bi}(g_{be} + j\omega(C_{be} + C_{bc}))} - j\omega C_{bep} \quad (4.21)$$

$$Y_{21} = \frac{g_{mo}e^{-j\omega\tau} - j\omega C_{bc}}{1 + R_{bi}(g_{be} + j\omega(C_{be} + C_{bc}))} - j\omega C_{bep} \quad (4.22)$$

$$Y_{22} = \frac{j\omega C_{bc}(g_{be} + g_{mo}e^{-j\omega\tau} + j\omega C_{be})}{1 + R_{bi}(g_{be} + j\omega(C_{be} + C_{bc}))} + j\omega C_{bep} \quad (4.23)$$

where $g_{be} = 1/R_{be}$ has been used. The influence from the parasitic base-emitter capacitance C_{bep} are removed by forming the following terms

$$Y_a = Y_{11} + Y_{12} = \frac{g_{be} + j\omega C_{be}}{1 + R_{bi}(g_{be} + j\omega(C_{be} + C_{bc}))} \quad (4.24)$$

$$Y_b = Y_{21} - Y_{12} = \frac{g_{mo}e^{-j\omega\tau}}{1 + R_{bi}(g_{be} + j\omega(C_{be} + C_{bc}))} \quad (4.25)$$

$$Y_c = Y_{22} + Y_{12} = \frac{j\omega C_{bc}R_{bi}(g_{be} + g_{mo}e^{-j\omega\tau} + j\omega C_{be})}{1 + R_{bi}(g_{be} + j\omega(C_{be} + C_{bc}))}. \quad (4.26)$$

The value of $1/|Y_b|^2$ is a quadratic function of frequency given by

$$\frac{1}{|Y_b|^2} = \frac{(1 + R_{bi}g_{be})^2}{g_{mo}^2} + \omega^2 \frac{R_{bi}^2(C_{be} + C_{bc})^2}{g_{mo}^2} \quad (4.27)$$

and verified by measurements on a $2 \times 6 \times 0.8 \mu\text{m}$ area SiGe HBT biased at $V_{ce} = 1.5\text{V}$, $I_c = 4.2\text{mA}$ as shown in Fig. 4.13. From Eq. 4.27 two useful terms are extracted as

$$a = \frac{1}{|Y_b|_{\omega \rightarrow 0}} = \frac{1 + R_{bi}g_{be}}{g_{mo}} \quad (4.28)$$

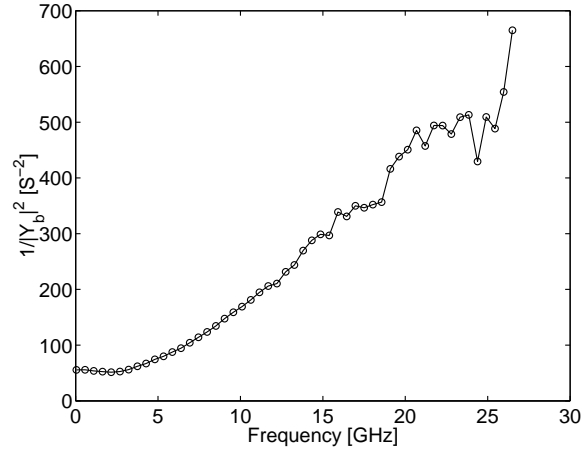


Figure 4.13 Extracted $1/|Y_b|^2$ for a $2 \times 6 \times 0.8 \mu\text{m}$ area SiGe HBT biased in the forward active region ($V_{ce}=1.5\text{V}$, $I_c=4.2\text{mA}$) verifying the quadratic frequency dependence.

and

$$b = \sqrt{\frac{\frac{1}{|Y_b|^2} - a^2}{\omega^2}} = \frac{R_{bi}(C_{be} + C_{bc})}{g_{mo}}. \quad (4.29)$$

Dividing Y_a by Y_b gives an expression from which two more terms are extracted as

$$c = \Re\left(\frac{Y_a}{Y_b} e^{-j\omega\tau}\right) = \frac{g_{be}}{g_{mo}} \quad (4.30)$$

and

$$d = \Im\left(\frac{Y_a}{Y_b} e^{-j\omega\tau}\right) = \frac{\omega C_{be}}{g_{mo}} \quad (4.31)$$

where the excess phase delay through the device τ is extracted from Y_b as

$$\omega\tau = -\left(\angle Y_b + \arctan \frac{\omega b}{a}\right). \quad (4.32)$$

In Fig. 4.14 a linear dependence on frequency is observed, except at low frequencies, for the extracted value of $\omega\tau$ for a $2 \times 6 \times 0.8 \mu\text{m}^2$ area SiGe HBT. Furthermore it is seen that dividing Y_c by $Y_b + Y_a$, the following term emerge

$$\omega\tau_{RC} = \frac{Y_c}{Y_a + Y_b} = \omega R_{bi} C_{bc} \quad (4.33)$$

from which $\tau_{RC} = R_{bi} C_{bc}$ follows. In Fig. 4.15 the linear frequency dependence of the extracted value of $\omega\tau_{RC}$ for a $2 \times 6 \times 0.8 \mu\text{m}^2$ area SiGe HBT is verified. The equations 4.28-4.31 together with 4.33 are solved for the elements of the hybrid- π equivalent circuit as

$$R_{bi} = \frac{b - a\tau_{RC}}{d - c\tau_{RC}} \quad (4.34)$$

$$g_{mo} = \frac{1}{a - cR_{bi}} \quad (4.35)$$

$$R_{be} = \frac{1}{cg_{mo}} \quad (4.36)$$

$$\omega C_{be} = dg_{mo} \quad (4.37)$$

$$C_{bc} = \frac{\tau_{RC}}{R_{bi}} \quad (4.38)$$

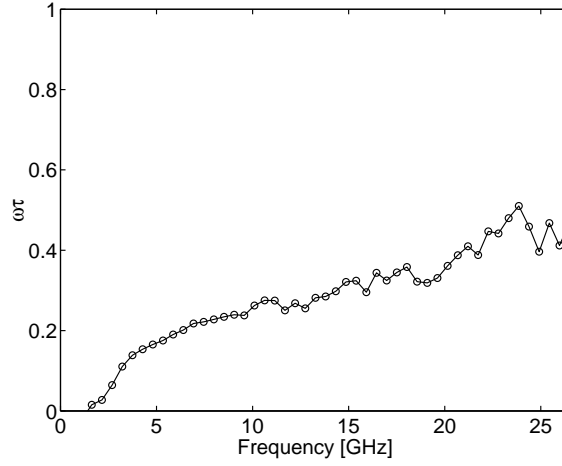


Figure 4.14 Extracted $\omega\tau$ for a $2 \times 6 \times 0.8 \mu\text{m}$ area SiGe HBT biased in the forward active region ($V_{ce} = 1.5\text{V}$, $I_c = 4.2\text{mA}$) verifying the linear frequency dependence.

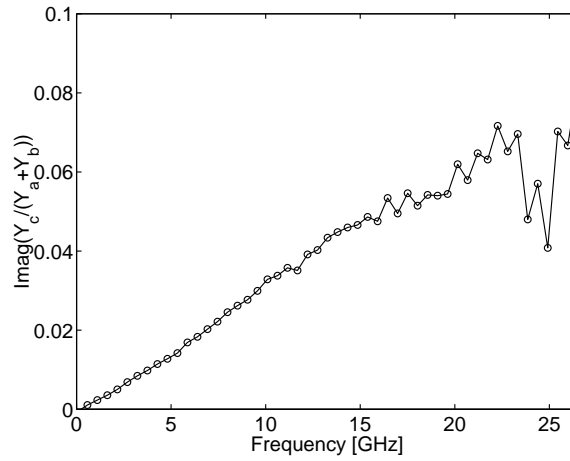


Figure 4.15 Extracted $\omega\tau_{RC}$ for a $2 \times 6 \times 0.8 \mu\text{m}$ area double-emitter SiGe HBT biased in the forward active region ($V_{ce} = 1.5\text{V}$, $I_c = 4.2\text{mA}$) verifying the linear frequency dependence.

and from Eq. 4.25 the parasitic base-emitter capacitance C_{bep} are found as

$$\omega C_{bep} = \Im \left(-Y_{12} - \frac{j\omega C_{bc}}{1 + g_{be}R_{bi} + j\omega R_{bi}(C_{be} + C_{bc})} \right). \quad (4.39)$$

In order to check the robustness of the parameter extraction method, the frequency dependence of the intrinsic base resistance is shown in Fig. 4.16 for the $2 \times 6 \times 0.8 \mu\text{m}^2$ area SiGe HBT device. The extracted parameters, in general shows well-behaved frequency dependence.

In Table. 4.3 a summary is given for the bias dependent extracted values (at a fixed collector-emitter voltage) obtained by the direct parameter extraction method for the SiGe HBT devices under investigation. As a verification of the direct parameter extraction method, the excellent agreement between measured and modeled S-parameters in the frequency range from 45 MHz-26.5 GHz is shown in Fig. 4.17. The bias point corresponds to the peak f_T for the devices.

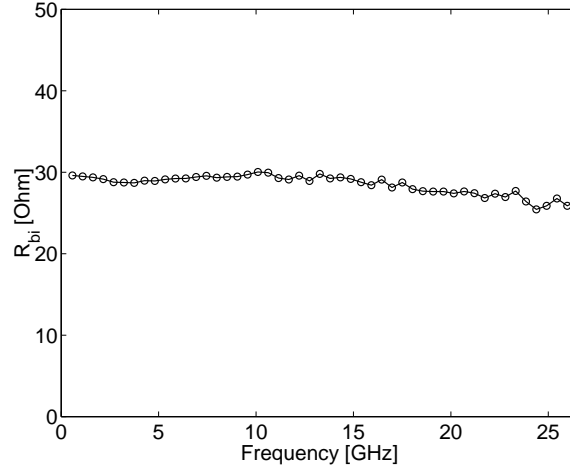


Figure 4.16 Frequency dependence of the extracted intrinsic base resistance R_{bi} for a $2 \times 6 \times 0.8 \mu\text{m}^2$ area SiGe HBT biased in the forward active region ($V_{ce} = 1.5\text{V}$, $I_c = 4.2\text{mA}$).

Parameter @ $V_{ce}=1.5\text{V}$	Extracted Value: ($2 \times 6 \times 0.8 \mu\text{m}^2$ area)			Extracted Value: ($4 \times 0.8 \mu\text{m}^2$ area)		
	$I_c=0.84\text{mA}$	$I_c=4.2\text{mA}$	$I_c=8.4\text{mA}$	$I_c=0.28\text{mA}$	$I_c=1.4\text{mA}$	$I_c=2.8\text{mA}$
R_{bi} [Ω]	33.3	28.3	23.1	103.6	83.0	68.1
C_{bc} [fF]	14.8	16.5	22.8	2.0	2.8	3.8
C_{be} [fF]	320	811	1625	113	295	576
R_{be} [Ω]	2388	464	222	6651	1273	603
g_{mo} [mS]	33	142	240	11	49	88
τ [pS]	3.32	3.04	2.28	2.48	1.8	0.8
C_{bep} [fF]	≈ 0	≈ 0	≈ 0	4.2	4.0	3.7

Table 4.3 Bias dependence of extracted parameters for $2 \times 6 \times 0.8 \mu\text{m}^2$ area and $4 \times 0.8 \mu\text{m}^2$ area SiGe HBT devices. For each transistor the first column corresponds to the linear part of the f_T versus I_c curve, the second column corresponds to peak- f_T and the third column corresponds to the high-current fall-off part of f_T .

4.1.3 Applicability of The Extraction Procedure For VBIC95 Modeling

Though an accurate extraction method for the small-signal equivalent circuit of SiGe HBT devices is certainly important, in order to estimate the influence from parasitic elements most wideband circuit design requires a large signal model. The parameter extraction for large signal models such as the VBIC95 model, usually requires optimization to extensive data [67]. In order to preserve the physical behavior, however, it is beneficial to extract as many of the model parameters as possible and minimize the number of unknowns in the final optimization process. The applicability of the direct parameter extraction method in connection with VBIC95 modeling for SiGe HBT devices, will be illustrated next. The VBIC model includes several features important to accurately model modern double-poly SiGe HBT devices. These includes [68, 69]

- improved Early effect modeling
- parasitic substrate transistor modeling
- fixed oxide capacitance modeling
- quasi-saturation modeling

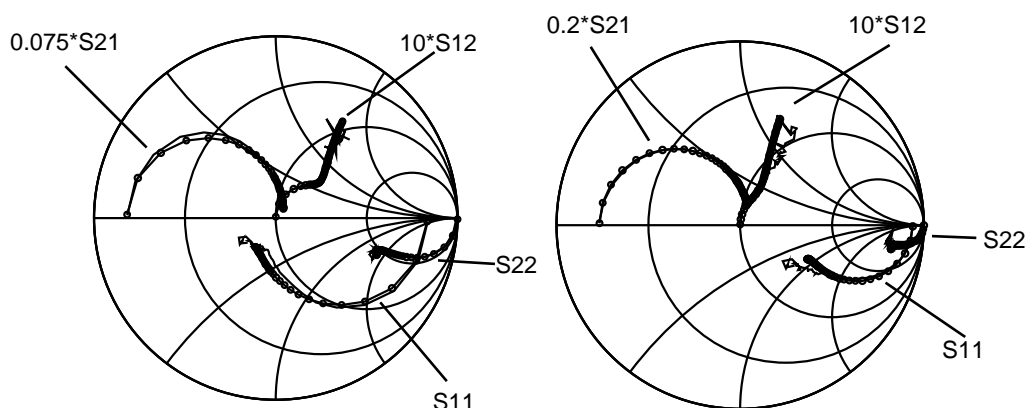


Figure 4.17 Measured (-) and modeled (-o-) S-parameters in the frequency range from 45 MHz-26.5 GHz for SiGe HBT devices biased in the forward active region. Left: $2\times6\times0.8\mu\text{m}^2$ area SiGe HBT ($V_{ce}=1.5\text{V}$, $I_c=4.2\text{mA}$). Right: $4\times0.8\mu\text{m}^2$ area SiGe HBT ($V_{ce}=1.5\text{V}$, $I_c=1.4\text{mA}$).

- excess phase modeling
- avalanche multiplication
- self-heating modeling.

The avalanche multiplication and self-heating modeling features will not be considered in the present parameter extraction method. As the main motivation is improved high-frequency modeling of the SiGe HBT devices the accuracy of the model will not suffer by leaving out these features. The equivalent circuit for the VBIC95 model is shown in Fig. 4.18. The VBIC model

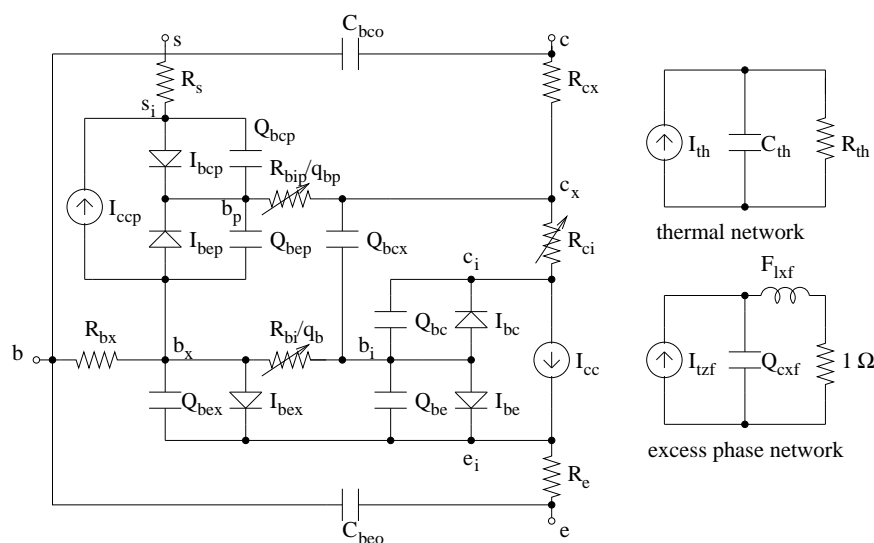


Figure 4.18 Equivalent circuit for VBIC95 model.

includes an intrinsic npn bipolar junction transistor based on the Gummel-Poon model, and

a parasitic pnp substrate transistor modeled with a partial Gummel-Poon model. Fixed oxide capacitances are added between the external base-emitter and base-collector nodes. Quasi-saturation is modeled with the elements R_{ci} , Q_{bcx} , and a modified Q_{bc} . Excess phase is modeled with a separate second order network which modifies the forward transport current.

The DC characterization for the SiGe HBT devices was performed on-wafer using a HP 4145A Semiconductor Parameter Analyzer. The SiGe HBT devices were laid out in a common-emitter configuration with the substrate and emitter terminals connected together. This was done for accurate high-frequency characterization, but made the parameter extraction in the reverse region of operation for the VBIC95 model cumbersome. The high frequency measurements were performed on-wafer in the frequency range from 45 MHz-26.5 GHz using a HP 8510B network analyzer. The VBIC95 model parameter extraction will be described for the $4 \times 0.8 \mu\text{m}^2$ area SiGe HBT device.

Early Effect Extraction

The modulation of the position of the base-emitter and base-collector depletion regions with bias observed in bipolar junction transistors is called the Early effect. Because the Early effect modeling in VBIC95 depends on the depletion charges, the first step in the extraction procedure is to extract the junction depletion capacitance parameters. The base-emitter and base-collector junction depletion capacitance parameters have already been extracted from S-parameters using cut-off mode measurements. In Table. 4.4, a summary of the extracted junction depletion capacitance parameters for the $4 \times 0.8 \mu\text{m}^2$ area SiGe HBT device are given. The partitioning of the total zero bias base-collector junction capacitance into the intrinsic part C_{jc} and extrinsic part C_{jep} is based on the ratio extracted under forward active bias at peak f_T .

Parameter	Extracted Value	Parameter	Extracted Value
C_{je} [fF]	16.73	C_{jep} [fF]	4.07
P_e [V]	1.14	P_c [V]	0.55
M_e	0.68	M_c	0.45
C_{jc} [fF]	2.85		

Table 4.4 Extracted junction depletion capacitance parameters for $4 \times 0.8 \mu\text{m}^2$ area SiGe HBT device.

The forward and reverse Early voltages, V_{ef} and V_{er} , are found solving the following equations [70]

$$\begin{bmatrix} (q_{j,bc}^f - c_{j,bc}^f I_c / g_o^f) & q_{j,be}^f \\ q_{j,bc}^r & (q_{j,be}^r - c_{j,be}^r I_e / g_o^r) \end{bmatrix} \begin{bmatrix} 1/V_{ef} \\ 1/V_{er} \end{bmatrix} = \begin{bmatrix} -1 \\ -1 \end{bmatrix} \quad (4.40)$$

where superscripts f and r denote forward and reverse region of operation respectively, q_j is the normalized junction charge, c_j is the derivative of q_j , and g_o is the output conductance. The normalized junction charge is found from junction parameters as follows

$$\begin{aligned} c_j &= \frac{\delta q_j}{\delta V_j} = \frac{1}{\left(1 - \frac{V_j}{P_j}\right)^{M_j}} \Rightarrow \\ q_j &= \frac{-P_j}{M_j - 1} \left(1 - \left(1 - \frac{V_j}{P_j}\right)^{(1-M_j)}\right) \end{aligned} \quad (4.41)$$

where V_j is the voltage, P_j the built-in potential, and M_j the grading coefficient for the junction in question. The extraction of the Early effect parameters from measurements should be

performed at a fixed low value of the base-emitter voltage in the forward region and a fixed low value of the base-collector voltage in the reverse region. The extracted forward and reverse Early voltages for the SiGe HBT devices are $V_{ef} = 84.65V$ and $V_{er} = 2.25V$ respectively.

Gummel Measurements

The transport current in VBIC95 is modeled as [71]

$$I_{cc} = \frac{I_s}{q_b} \left(\exp \left(\frac{V_{bei}}{N_f V_{tv}} \right) - \exp \left(\frac{V_{bci}}{N_r V_{tv}} \right) \right) \quad (4.42)$$

where V_{bei} is the internal base-emitter voltage, V_{bci} is the internal base-collector voltage, I_s is the saturation current, q_b is the normalized base charge, N_f and N_r are the forward and the reverse ideality factors respectively. The normalized base charge is modeled using depletion charge components, and high level injection is modeled with the knee currents parameters I_{kf} and I_{kr} . The parameters I_s , N_f , and I_{kf} for the forward transport current are extracted from forward Gummel measurement in the range from 0.4-1.2 V. The base-collector voltage was set to 0 V to avoid the influence from avalanche currents and self-heating effects [72]. The ideality factor is extracted from the slope of the $\ln(I_c)$ against V_{be} curve at low voltages. The saturation current is extracted taking the influence of the reverse Early voltage on the forward Gummel characteristic into account [70] as

$$\ln \left(\frac{I_s}{q_b} \right) = \ln(I_c) - \frac{V_{bei}}{N_f V_{tv}} \quad (4.43)$$

where $q_b \approx 1 + q_{j,be}/V_{er}$ is the normalized base charge at low voltages. The current that corresponds to the current gain β at half of its peak value is defined as the forward knee current. Because the current gain at high currents is influenced by series resistances, only a rough estimate of the knee current can be extracted if these resistances are not known. The base-emitter component of the base current consist of ideal and non-ideal components ¹ as

$$I_{be} = I_{bei} \left(\exp \left(\frac{V_{bei}}{N_{ei} V_{tv}} \right) - 1 \right) + I_{ben} \left(\exp \left(\frac{V_{bci}}{N_{en} V_{tv}} \right) - 1 \right) \quad (4.44)$$

where I_{bei} , N_{ei} and I_{ben} , N_{en} are the base-emitter ideal and non-ideal parameters respectively. The ideal component of the base current is due to recombination in the neutral emitter region and at the emitter contact, while the non-ideal component is caused by recombination in the base-emitter depletion region [62]. The non-ideal parameters are extracted from the $\ln(I_b)$ versus V_{be} curve in the forward Gummel plot at low voltages. The ideal parameters are extracted at medium voltages where the influence from series resistances (R_{bx} , R_{bi} and R_e) is negligible.

The parasitic substrate transistor is modeled in VBIC95 similarly to the intrinsic transistor. The parasitic transport current is given as

$$I_{ccp} = \frac{I_{sp}}{q_{bp}} \left(\exp \left(\frac{V_{bep}}{N_{fp} V_{tv}} \right) - \exp \left(\frac{V_{bcp}}{N_{rp} V_{tv}} \right) \right) \quad (4.45)$$

where V_{bep} is the internal parasitic base-emitter voltage, V_{bcp} is the internal parasitic base-collector voltage, I_{sp} , N_{fp} and q_{bp} are the saturation current, ideality factor, and normalized base charge for the parasitic substrate transistor. The normalized base charge only includes the knee current I_{kp} to model forward high injection as the Early effects and reverse high injection are not important for the parasitic substrate transistor. Because the substrate terminal have been

¹Actually in VBIC95 the base-emitter current is partitioning between an intrinsic component I_{be} and extrinsic component I_{bex} using the parameter W_{be} in order to model to first order the distributed nature of the base.

connected to the emitter terminal in the SiGe HBT device under test, it was necessary to extract the saturation current and ideality factor from the reverse Gummel plot of the parasitic substrate transistor. In order to measure the reverse Gummel plot for the parasitic substrate transistor the SiGe HBT devices must be biased with a negative potential on the collector and base terminals relative to the emitter, e.g. $-V_c > 0V$ and $V_{bc} = 0V$. The reverse current component for the parasitic substrate transistor modeled ($q_{bp} = 1$ for the reverse current component) as

$$I_{trp} = I_{sp} \exp\left(\frac{V_{bcp}}{N_{fp}V_{tv}}\right) \quad (4.46)$$

will flow out of the base of the SiGe HBT device. The base-collector current for the parasitic substrate transistor flows out of the collector of the SiGe HBT device and consist of a ideal and non-ideal components modeled as

$$I_{bcp} = I_{bcip} \left(\exp\left(\frac{V_{bcp}}{N_{cip}V_{tv}}\right) - 1 \right) + I_{bcnp} \left(\exp\left(\frac{V_{bcp}}{N_{cnp}V_{tv}}\right) - 1 \right) \quad (4.47)$$

where I_{bcip} , N_{cip} and I_{bcnp} , N_{cnp} are the parasitic base-collector ideal and non-ideal parameters respectively. The ideality factor for the reverse current component of I_{ccp} is extracted from the slope of the $\ln(I_{trp})$ versus V_{bcp} curve, and the saturation current I_{sp} is extracted as

$$\ln(I_{sp}) = \ln(I_{trp}) - \frac{V_{bcp}}{N_{fp}V_{tv}}. \quad (4.48)$$

The non-ideal parameters are extracted from the $\ln(I_{bcp})$ versus V_{bcp} curve in the reverse Gummel plot for the parasitic substrate transistor at low voltages. The ideal parameters are extracted at medium voltages, where the influence from series resistances (R_{bp} , R_s and R_{cx}) is negligible. The base-emitter current for the parasitic substrate transistor is modeled as

$$I_{bep} = I_{beip} \left(\exp\left(\frac{V_{bep}}{N_{ci}V_{tv}}\right) - 1 \right) + I_{benp} \left(\exp\left(\frac{V_{bep}}{N_{cn}V_{tv}}\right) - 1 \right) \quad (4.49)$$

where I_{beip} , N_{ci} and I_{benp} , N_{cn} are the parasitic base-emitter ideal and non-ideal parameters respectively. The extraction of the parasitic base-emitter current parameters is complicated by the fact that it is not possible to separate the substrate current component, base-collector current, and the parasitic base-emitter current in the measurement. It turns out, however, that the base-collector and parasitic base-emitter current can be estimated from a measurement with a negative bias on the collector and zero bias on the base of the SiGe HBT device, e.g. $-V_c > 0V$ and $V_b = 0V$. In this measurement, the substrate transistor is saturated because $-V_c \approx V_{bcp} \approx V_{bep} > 0V$ and the parasitic transport current cancels at low voltages, where the approximation is most accurate. That is, at low voltages the base current consist only of the base-collector and parasitic base-emitter current. This is verified by simulations on the extracted VBIC95 model that compares the parasitic base-emitter current in the reverse Gummel plot (found by subtracting the substrate current from the base current) and the base current with saturated substrate transistor². The results are shown in Fig. 4.19 and proves that the extraction of the ideal and non-ideal parameters for the parasitic base-emitter current can be performed from the measurement with saturated substrate transistor if the voltages is kept below 0.6 V. In the measurement with saturated substrate transistor the emitter current $I_e = -(I_b + I_c)$ is influenced by the reverse transport current parameters N_r and I_{kr} . An approximate value for these parameters can be obtained by fitting.

A summary of the VBIC95 model parameters extracted from Gummel measurements is given in Table. 4.5. Because the parasitic resistors were already found using the direct parameter extraction method, the high current parameters required very little optimization.

²In the extracted VBIC95 model the base-collector current is absorbed as part of parasitic base-emitter current.

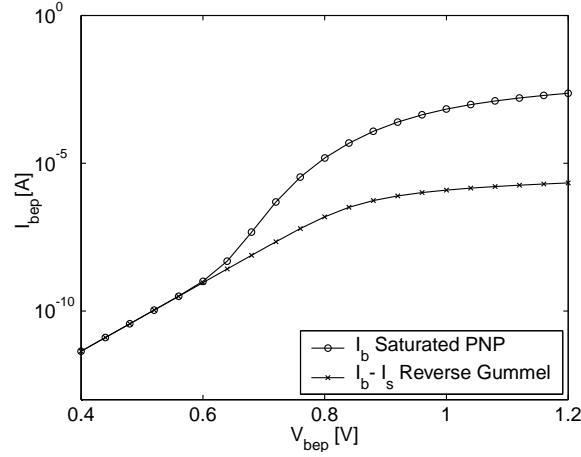


Figure 4.19 Comparison of parasitic base-emitter current I_{bep} found from reverse Gummel plot ($I_{bep} = I_b - I_s$) and saturated parasitic pnp substrate transistor ($I_{bep} = I_b$ at $V_{bcp} > 0V$ and $V_{bep} > 0V$).

Parameter	Extracted Value	Parameter	Extracted Value
I_s [A]	3.5e-18	N_{ci}	1.46
N_f	0.99	N_{cn}	4.93
N_r	1.01	I_{sp} [A]	3.1e-19
I_{kf} [mA]	6	N_{sp}	0.93
I_{kr} [mA]	0.39	I_{kp} [A]	∞
I_{bei} [A]	53e-21	I_{beip} [A]	46e-21
I_{ben} [A]	53.9e-15	I_{benp} [A]	33e-18
N_{ei}	1.01	W_{sp}	—
N_{en}	2.41	I_{bcip} [A]	9.4e-15
W_{be}	—	I_{bcnp} [A]	—
I_{bci} [A]	—	N_{cip}	1.13
I_{bcn} [A]	—	N_{cnp}	—

Table 4.5 VBIC95 model parameters extracted from Gummel measurements for $4 \times 0.8 \mu m$ area SiGe HBT device. Parameters kept at the default value are denoted (—).

Quasi-Saturation Parameters

At high injection levels in the collector, the DC current gain drops as does the unity current gain frequency due to base push-out into the lightly doped collector region. This phenomena is called quasi-saturation and happens when the internal base-collector junction becomes forward biased while the external base-collector terminal remains reverse biased [73]. In this operation region minority carriers are injected into the collector from the base, effectively widening the base and storing excess charge. Quasi-saturation is modeled in VBIC95 using the parameters R_{ci} , V_o , γ , H_{rci} , and Q_{co} as explained in the VBIC95 model description [71].

The unmodulated intrinsic collector resistance R_{ci} can be estimated using knowledge about the collector epi-layer doping N_{epi} and the width of the lightly doped collector W_{epi} as

$$R_{ci} = \frac{W_{epi}}{qA_e N_{epi} \mu_n} \quad (4.50)$$

where q is the electron charge, A_e is the emitter area, and μ_n is the doping dependent electron

mobility. The epi-drift saturation voltage V_o accounts for the influence from velocity saturation on the current in the collector region. It can be estimated from

$$V_o = \frac{W_{epi} v_{sat}}{\mu_n} \quad (4.51)$$

where v_{sat} is the saturation velocity for electrons in Silicon. Conductivity modulation in the collector region is modeled using the epi-doping parameter γ which can be estimated from

$$\gamma = \left(\frac{2n_i}{N_{epi}} \right)^2 \quad (4.52)$$

where n_i is the intrinsic carrier concentration for Silicon. At high current levels the rise in collector current with collector-emitter voltage is empirically modeled using the high current parameter H_{rcf} . Finally, the stored excess charge Q_{co} , important for high-frequency modeling in quasi-saturation is estimated from

$$Q_{co} = \frac{1}{4} q A_e W_{epi} N_{epi}. \quad (4.53)$$

Unfortunately the epi-layer doping is not known for the 0.8 μm SiGe HBT process from AMS. Instead, the quasi-saturation parameters have been calculated for three different epi-layer doping levels as shown in Table. 4.6. An epi-layer doping level of $N_{epi} = 10^{17} \text{ cm}^{-3}$ seems to give a good agreement between the VBIC95 model and measured forward output characteristic as will be shown later. The high current parameter H_{rcf} was kept at the default value.

$N_{epi} [\text{cm}^{-3}]$	$R_{ci} [\Omega]$	$V_o [V]$	γ	$Q_{co} [C]$
1e16	650.2	0.33	4.16e-12	0.51e-15
5e16	156.1	0.40	166.5e-15	2.55e-15
1e17	97.5	0.50	41.6e-15	5.13e-15

Table 4.6 Calculated quasi-saturation parameter. Semiconductor parameters used in the calculations are: $n_i = 1.02e10 \text{ cm}^{-3}$, $v_{sat} = 1e7 \text{ cm s}^{-1}$, $\mu_n(N_{epi} = 1e16 \text{ cm}^{-3}) = 1.2e3 \text{ cm}^2/Vs$, $\mu_n(N_{epi} = 5e16 \text{ cm}^{-3}) = 1e3 \text{ cm}^2/Vs$, $\mu_n(N_{epi} = 1e17 \text{ cm}^{-3}) = 0.8e3 \text{ cm}^2/Vs$ (From [74]).

AC Parameters Extraction

The extraction of the VBIC95 model parameters of interest for the ac-modeling includes the intrinsic base resistance R_{bi} , the forward transit time parameters T_f , I_{tf} , V_{tf} , X_{tf} , reverse transit time T_r , and excess phase delay T_d .

The bias dependence of the intrinsic base resistance due to conductivity modulation is modeled as R_{bi}/q_b , where q_b is the normalized base charge [69]. High-frequency S-parameters, measured at several bias points in the forward active region, is used to determine the intrinsic base resistance by applying the direct parameter extraction method. As the collector current I_c goes toward zero, the normalized base charge becomes approximately unity. The extraction of the parameter R_{bi} is then achieved by extrapolating values of R_{bi}/q_b versus collector current I_c onto the ordinate axis, as shown in Fig. 4.20.

The forward transit time τ_f is important for accurate modeling of the base-emitter diffusion charge $\tau_f I_c$. The current dependence of the total transit time from emitter to collector for a

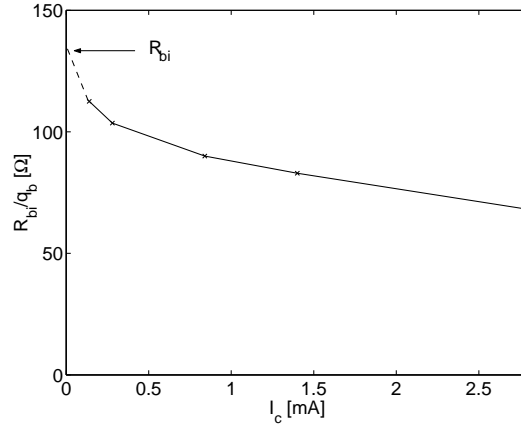


Figure 4.20 Intrinsic base resistance R_{bi}/q_b versus collector current I_c extracted on $4 \times 0.8 \mu\text{m}^2$ area SiGe HBT device biased in the forward active region.

SiGe HBT device has been discussed previously in chapter 3 of this thesis. When the effect of parasitic series resistances is included, the transit time is modified as [64]

$$\frac{1}{2\pi f_T} \approx T_f + \frac{V_{IV}}{I_c} (C_{be} + C_{bc} + C_{bep}) + (R_{ci} + R_{cx})C_{bc} \quad (4.54)$$

where C_{be} , C_{bc} and C_{bep} are depletion capacitances and T_f contains the transit times through the base and collector regions. The forward transit time parameter T_f is extracted from a plot of the transit time, found from measured f_T , versus the inverse of collector current [62]. The transit time extrapolated to the ordinate (infinity collector current) as shown in Fig. 4.21 (left plot) is then given as $T_f + (R_{ci} + R_{cx})C_{bc}$, from which the forward transit time parameter T_f is easily extracted. The bias dependence of the forward transit time is modeled according to

$$\tau_f = T_f (1 + Q_{tf} q_b) \left(1 + X_{tf} \left(\frac{I_c}{I_c + I_{tf}} \right)^2 \exp \frac{V_{bci}}{1.44 V_{tf}} \right) \quad (4.55)$$

where I_{tf} , Q_{tf} , V_{tf} , and X_{tf} models the current and voltage bias dependence. These parameters are extracted by fitting measured f_T versus collector current I_c , for two different collector-emitter voltages, as shown in Fig. 4.21 (right plot). In general, the bias dependence of the unity current gain frequency is well predicted by the extracted VBIC95 model also in the high current region where the Kirk effect results in the f_T fall-off.

The reverse transit time is important to model the base-collector diffusion charge $\tau_r I_e$, when the base-collector junction becomes forward biased. It have been shown that the relation

$$T_f I_{kf} = T_r I_{kr} \quad (4.56)$$

should hold for the transport and charge models to be consistent in the VBIC95 model [71]. Once the forward transit time T_f , and knee current parameters I_{kf} and I_{kr} have been extracted, T_r is found using the above relation.

The excess phase delay becomes important in the frequency range close to the unity current gain frequency f_T . In the direct parameter extraction method, the excess phase delay was modeled as a phase shift affecting the small-signal transconductance as $g_{mo} e^{-j\omega\tau}$. An estimate for the excess phase delay factor T_d can be extracted from high-frequencies S-parameters measured on the SiGe HBT device biased in the forward active region, as shown in Fig. 4.22. At low bias currents, the excess phase delay decreases with the increase of the current, but once base-widening effects becomes noticeable it increases due to the increase in τ_f [75]. The decrease

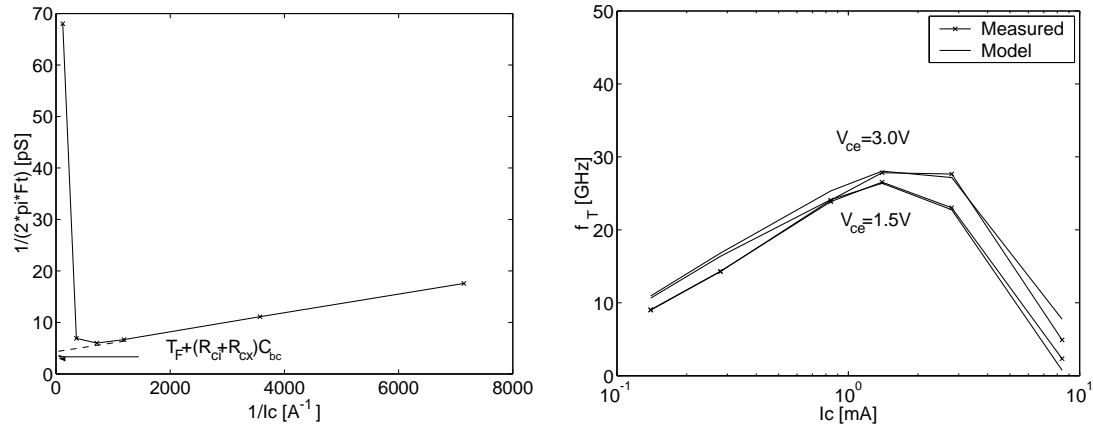


Figure 4.21 Transit time parameter extraction for $4 \times 0.8 \mu\text{m}^2$ area SiGe device. Left: Transit time versus inverse of collector current. Right: Bias dependence of the unity current gain frequency f_T .

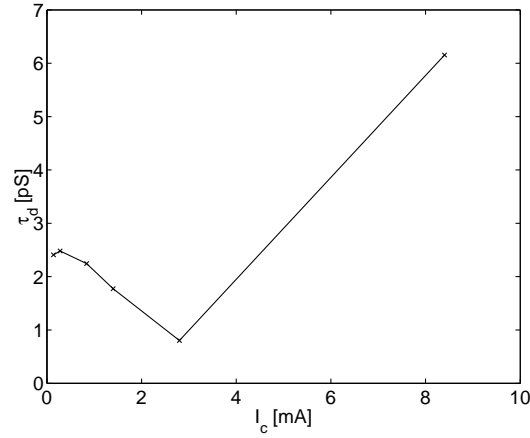


Figure 4.22 Bias dependence for excess phase delay τ extracted from $4 \times 0.8 \mu\text{m}^2$ SiGe HBT device ($V_{ce} = 1.5\text{V}$).

in excess phase delay at low currents might be explained by the bias dependence of the delay through the collector depletion region, which contribute to the total excess phase delay [75]. That is, as the current increases (with fixed collector-emitter voltage), the base-collector reverse voltage, and hence the depletion width decreases, resulting in reduced transit time through the collector depletion region. In the VBIC95 model, the excess phase delay is bias independent, so the extracted value at low bias current should be used for T_d [75].

Table. 4.7 shows a summary of the ac parameters extraction using high-frequency S-parameters for the $4 \times 0.8 \mu\text{m}^2$ SiGe HBT device.

Model Verification

The extracted parameters were applied to the built-in VBIC95 circuit component in the microwave simulator HP Advanced Design System (ADS) from Agilent, and the model verification will be given here.

In Fig. 4.23, the VBIC95 model fit to measured forward Gummel and forward beta characteris-

Parameter	Extracted Value	Parameter	Extracted Value
R_{bi} [Ω]	135	V_{tf} [V]	1.3
T_f [pS]	4.0	I_{tf} [A]	0.037
X_{tf}	8	T_r [pS]	62.1
Q_{tf}	—	T_d [pS]	2.4

Table 4.7 VBIC95 model ac parameters extracted from measured high-frequency S-parameters for the $4 \times 0.8 \mu m^2$ area SiGe HBT device. Parameters kept at the default value is denoted (—).

tics are shown. The forward Gummel and forward beta characteristics are accurately modeled at low voltages (compare with the design-kit model response described in chapter 3). The deviation in the collector current at high voltages may be due to thermal effects not yet accounted for. In general, the saturation current, base-emitter currents, ideality factors, reverse Early voltage, series resistances, and knee current parameter which influence the forward Gummel and forward beta characteristics seems to be accurately extracted. It should also be mentioned that the measured reverse Gummel plot for the parasitic substrate transistor, as well as the measured result with saturated parasitic substrate transistor are reasonable predicted by the extracted VBIC95 model (not shown).

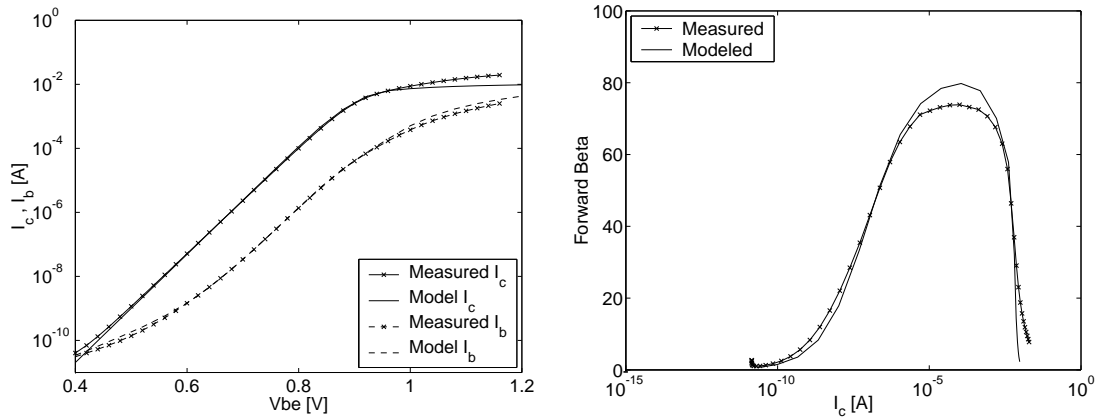


Figure 4.23 Measured and modeled forward Gummel plot (left) and forward beta (right) for the $4 \times 0.8 \mu m^2$ area SiGe HBT device.

The VBIC95 model fit is compared to the measured forward output characteristic for constant base currents in the range from 20-100 μA as shown in Fig. 4.24. The rather large forward Early voltage extracted is verified by the observed current slope at low base currents. The transition region from saturated to the linear region is well predicted by the calculated quasi-saturation parameters for an epi-layer doping of 10^{17} cm^{-3} . The current slope observed in the measured data at high base currents, however, is not included in the present VBIC95 model because the high current parameter was kept at the default value. In order to fit this region the quasi-saturation parameters needs to be optimized to the measured data with resulting loss of the physical nature.

Fig. 4.25 shows the VBIC95 model fit compared to measured S-parameters for the $4 \times 0.8 \mu m^2$ SiGe HBT device. The SiGe HBT device is biased at $V_{ce} = 1.5V$, $I_c = 1.4mA$ corresponding to peak f_T . The VBIC95 model is able to predict very well the frequency response of both magnitude and phase for all measured S-parameters in the frequency range from 45 MHz-

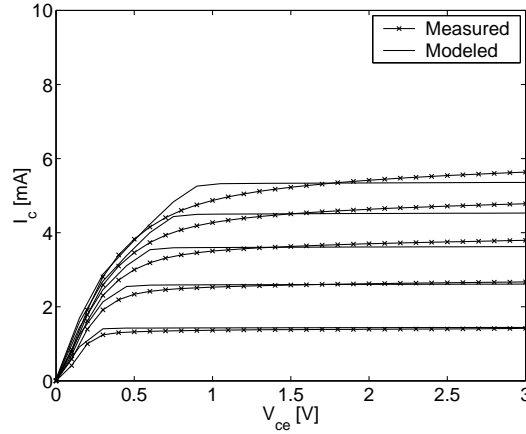


Figure 4.24 Measured and modeled forward output characteristic for the $4 \times 0.8 \mu\text{m}^2$ area SiGe HBT device biased with constant base currents in the range from 20-100 μA .

26.5 GHz. Compared with the frequency response for the design kit model investigated in chapter three of this thesis, the following improvements are observed. First, the frequency range where the magnitude and phase of the S_{11} parameter are reasonable well predicted is extended significantly. Also the magnitude and phase of the S_{22} parameter are now well predicted in the measured frequency range. The improvements are a result of more accurately modeling of the distributed base region, parasitic capacitances and substrate parasitic modeling. The extracted VBIC95 model should thus be more accurate for wideband circuit design, where the influence from parasitics elements are important.

4.2 Substrate Effects in Basic Circuit Configurations

The investigation of substrate effects in basic circuit configurations is mainly concerned with the influence from various parasitics on the frequency response of a SiGe HBT differential amplifier, as shown in Fig. 4.26. The reasons for choosing this rather simple circuit are its common use in integrated circuit designs even at microwave frequencies, as well as the existence of a theoretical expression for the bandwidth of an ideal differential amplifier in terms of the SiGe HBT device parasitics. An ideal SiGe HBT differential amplifier consist only of the SiGe HBT devices and ideal resistors. In reality the SiGe HBT devices are embedded in interconnect lines and pads structures that add parasitics and therefore influence the frequency response. Also the poly resistors may have a significant parasitics capacitance to the substrate that needs to be taken into account.

After a discussion of the influence of the transistor parasitics, the extraction of suitable equivalent circuit models for pad structures, interconnect lines, and poly resistors will be described. It will be shown how the inclusion of these equivalent circuit models in simulations makes it possible to predict the measured performance of a SiGe HBT differential amplifier.

4.2.1 Influence of Transistor Parasitics

The SiGe HBT differential amplifier shown in Fig. 4.26 was designed, using the design kit for the $0.8 \mu\text{m}$ SiGe HBT process from AMS, for a transducer gain S_{21} of 5 dB and a 3 dB bandwidth of 4.6 GHz. The transistors in the differential pair (Q_1 and Q_2) each have an emitter dimension of $4 \times 0.8 \mu\text{m}^2$, and the transistors in the current mirror have $8 \times 0.8 \mu\text{m}^2$ emitter area. A

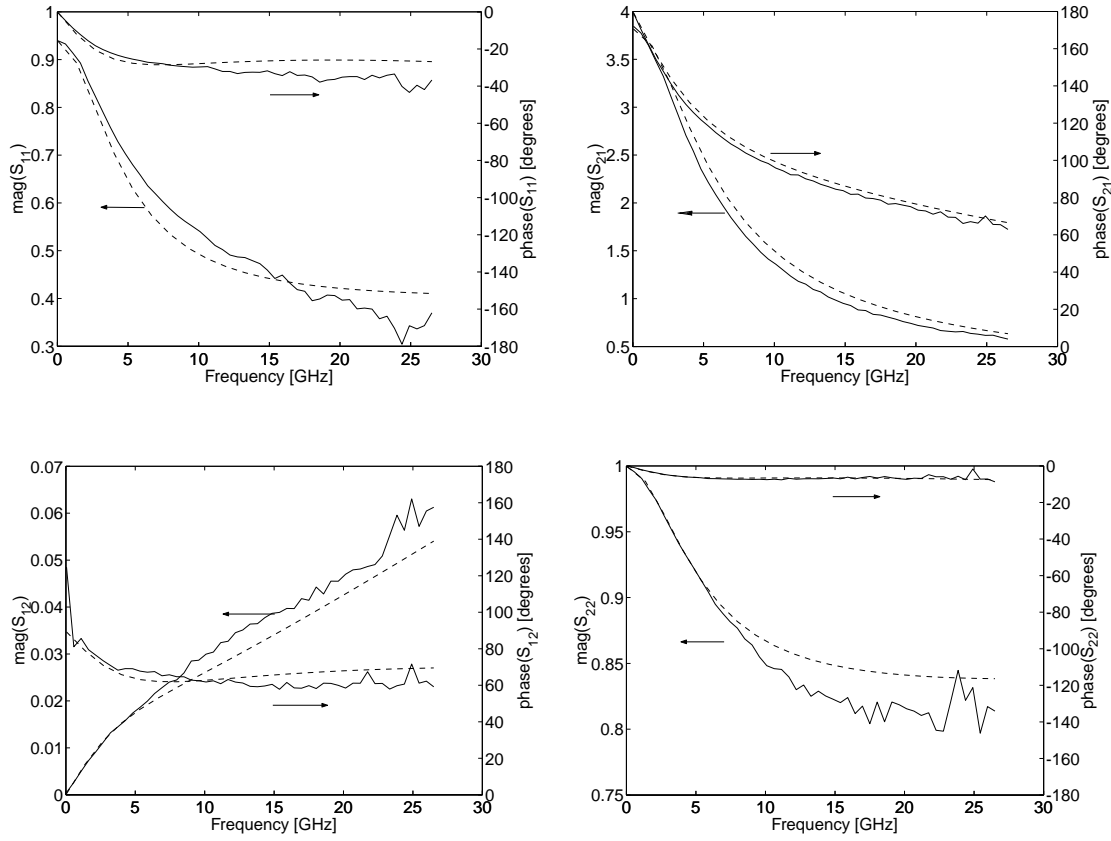


Figure 4.25 Frequency dependence for S-parameters for $4 \times 0.8 \mu\text{m}^2$ area SiGe HBT device biased at $V_{ce} = 1.5\text{V}$, $I_c = 1.4\text{mA}$. Solid and dashed line represent measured and modeled frequency response respectively.

bias current of 2.85 mA was used in order to obtain the largest bandwidth performance.

The bandwidth capabilities of the SiGe HBT differential amplifier is expressed as [76]

$$\frac{1}{f_{3dB}} = \frac{1}{f_v} + \frac{2\pi|a_{vo}|C_{tot}}{g_m} + \frac{|a_{vo}|f_T}{4f_{max}^2} \quad (4.57)$$

where f_v is the input bandwidth, $|a_{vo}| = g_m R_L$ is the low frequency voltage gain, and $C_{tot} = C_{bc} + C_{bep} + C_{bcp} + C_L$. The first term represents the response of the internal base-emitter junction to an applied input voltage, and depends on the unity current gain frequency f_T as

$$\frac{1}{f_v} = \frac{g_m R_{bb}}{f_T} \quad (4.58)$$

where R_{bb} is the total base resistance. The second term represents the conversion of the collector current into an output voltage and is determined by the load impedance, the collector-substrate and the total base-collector capacitance. The third term represents the Miller effect expressed here in terms of the transistor parameters f_T and f_{max} .

The contribution from each term (input bandwidth, output loading, and Miller effect) in the above expression, to the 3 dB bandwidth of the SiGe HBT differential amplifier can be calculated using extracted values for the $4 \times 0.8 \mu\text{m}^2$ SiGe HBT device. Table. 4.8 shows the individual contributions calculated for SiGe HBT devices biased at $V_{ce} = 1.5\text{V}$, $I_c = 1.4\text{mA}$ and assuming 50Ω source and load impedances. The calculated 3 dB bandwidth $f_{3dB} = 4.1\text{ GHz}$ comes close

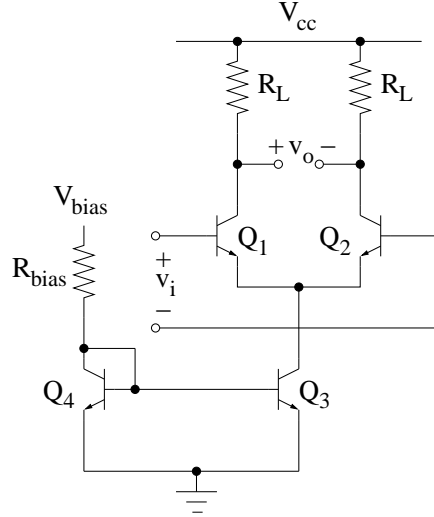


Figure 4.26 SiGe HBT differential amplifier.

Contribution	Value [GHz]
Input bandwidth	4.7
Output loading	110.9
Miller effect	49.2
f_{3dB}	4.1

Table 4.8 Contribution from input bandwidth, output loading and Miller effect terms to 3 dB bandwidth of SiGe HBT differential amplifier.

to simulation expectations for the SiGe HBT differential amplifier and is mainly limited by the low input bandwidth of the transistors in the differential pair. The insignificant contribution from the Miller effect and output loading is a result of the low transducer gain and neglect of output capacitive loading.

4.2.2 Pad Structures and Interconnect Lines Modeling

In order to reduce the influence from substrate coupling, it is recommended to apply ground shielded pads [48]. The ground-shielded pad configuration uses an n^+ -layer underneath the signal pad to prevent coupling to the substrate, as already mentioned in connection with the transistor modeling. The pad structure model shown in Fig. 4.27 (left plot) was extracted from on-wafer high-frequency S-parameter measurements in the frequency range from 45 MHz-26.5 GHz using an open test structure without any interconnect lines. The effect of substrate coupling is neglected (e.g. R_f is infinity) and the pad capacitance C_{pad} is extracted as

$$\omega C_{pad} = \frac{1}{\Im\left\{\frac{-1}{Y_{11}+Y_{12}}\right\}} \quad (4.59)$$

using measured Y-parameters. The shield resistance is found as

$$R_{shield} = \Re\left\{\frac{1}{Y_{11}+Y_{12}}\right\}. \quad (4.60)$$

The right plot in Fig. 4.27 shows the excellent fit to measured S_{11} for the extracted pad structure model.

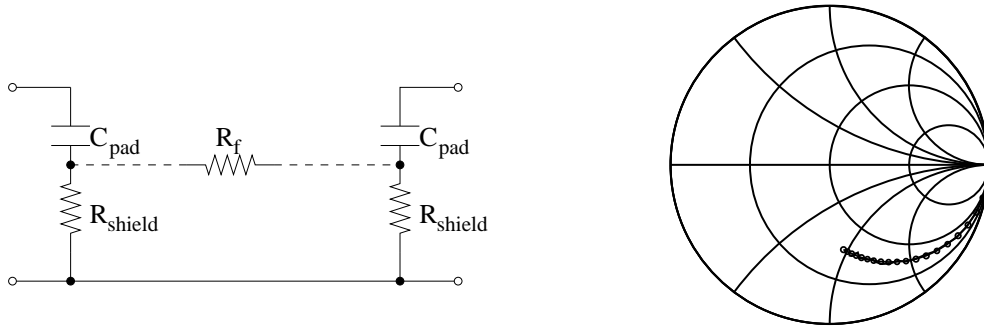


Figure 4.27 Pad structure modeling. Left: Lumped element equivalent circuit model. Right: Model fit (dotted line) to measurements (solid line) for S_{11} in the frequency range from 45 MHz-26.5 GHz.

In silicon bipolar processes, the metal-insulator-semiconductor interconnect line structure results in large wiring capacitances to the substrate. The loss in the substrate can not be neglected at high frequencies and should be taken into account in the modeling of the interconnect lines [77]. Even though the interconnect line in principle is a distributed structure, it is assumed here that a simple π -type model as shown in left plot of Fig. 4.28 is sufficient accurate to model the behavior of the interconnect line at least to 10 GHz. The equivalent circuit model consist of a series resistance R_s , a series inductance L_s , an oxide capacitor to the substrate C_{ox} , and the substrate resistance R_{sub} . Adding a shunt capacitor across the substrate resistance may be necessary at higher frequencies where the dielectric properties of the substrate have to be taken into account [43]. An interconnect line test structure with line length of $369\mu\text{m}$ and line width of $6.8\mu\text{m}$ using the top metal layer in the SiGe HBT process from AMS was measured on-wafer in the frequency range from 45 MHz-26.5 GHz. The elements of the equivalent circuit model are extracted using Y-parameters de-embedded for pad parasitics as follows. First, the series resistance and series inductance of the line are extracted as

$$R_s = \Re\left\{\frac{-1}{Y_{12}}\right\} \quad (4.61)$$

and

$$\omega L_s = \Im\left\{\frac{-1}{Y_{12}}\right\} \quad (4.62)$$

respectively. The oxide capacitance to the substrate is then extracted as

$$\omega C_{ox} = \frac{1}{\Im\left\{\frac{-1}{Y_{11} + Y_{12}}\right\}} \quad (4.63)$$

and the substrate resistance as

$$R_{sub} = \Re\left\{\frac{1}{Y_{11} + Y_{12}}\right\}. \quad (4.64)$$

The frequency dependent lossy behavior of the interconnect line on silicon is clearly observed in the right plot of Fig. 4.28. In general the fit to measured S_{21} and S_{11} is good except at very high frequencies where it seems like the loss in the substrate is a bit to high in the model.

A summary of the extracted equivalent circuit elements for the pad structure and the interconnect line are given in Table. 4.9. The elements of the interconnect line model can be scaled to fit different line geometries, when necessary.

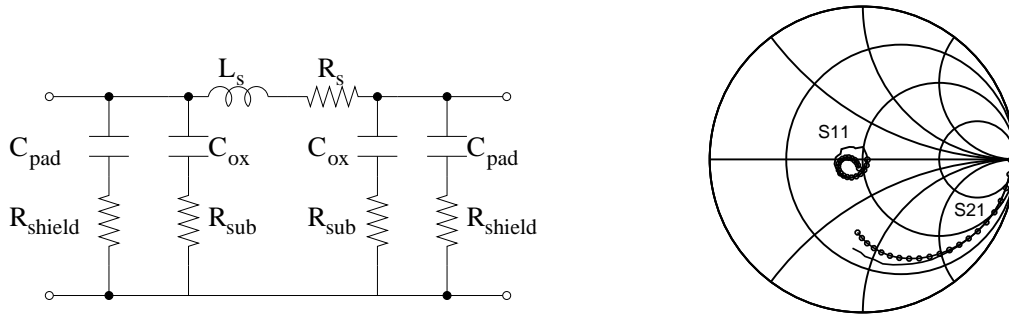


Figure 4.28 Interconnect line model including pad structure parasitics. Left: Lumped element equivalent circuit model. Right: Model fit (dotted lines) to measurements (solid lines) for S_{11} and S_{21} in the frequency range from 45 MHz-26.5 GHz for a $6.8 \mu\text{m}$ wide and $369 \mu\text{m}$ long interconnect line implemented in the top metal layer.

Parameter	Extracted Value	Parameter	Extracted Value
C_{pad} [fF]	126.1	R_{shield} [Ω]	31.7
R_s [Ω]	3.3	L_s [pH]	371.1
C_{ox} [fF]	31.5	R_{sub} [Ω]	124.9

Table 4.9 Extracted values of equivalent circuit element for pad structure and interconnect line model. The interconnect line is implemented in the top metal layer with line length of $369 \mu\text{m}$ and line width of $6.8 \mu\text{m}$.

4.2.3 Poly Resistor Modeling

The parasitic capacitance to the substrate of a poly resistor depends on the area and the perimeter of the resistor. Shielding to the substrate are possible using a n-well underneath the poly resistor or alternatively a p^+ -guardring could be placed around the poly resistor. High-frequency S-parameters for a 200Ω poly resistor (Poly1) test structure was measured on-wafer in the frequency range from 45 MHz-10 GHz. A p^+ -guardring was placed around the poly resistor in the test-structure in order to define the potential of the substrate close to the resistor. The measured Y-parameters were de-embedded for pad structure and interconnect line parasitics, using an open and a short standard. The π -type equivalent circuit model for the poly resistor is shown in the left plot of Fig. 4.29. The extraction of the elements follows the same procedure as for the interconnect lines. As shown in the right plot of Fig. 4.29, the fit to measured S-parameters S_{11} and S_{21} after de-embedding is good. A very weak frequency dependence is observed for the poly resistor implemented in the poly1 layer.

A summary of the extracted equivalent circuit elements for the poly resistor are given in Table. 4.10. The elements of the poly resistor model can be scaled to fit different geometries when necessary.

4.2.4 Experimental Results

The layout of the differential amplifier implemented in the $0.8 \mu\text{m}$ SiGe HBT process from AMS is shown in Fig. 4.30. The differential amplifier was on-wafer measured using a HP 8510B Network Analyzer in the frequency range from 45 MHz to 10 GHz. The network analyzer

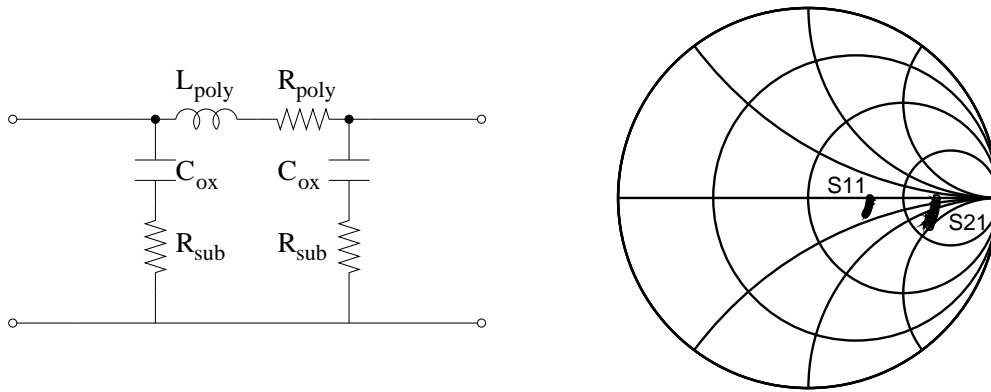


Figure 4.29 Poly resistor model without pad structure and interconnect line parasitics. Left: Lumped element equivalent circuit model. Right: Model fit (dotted lines) to measurements (solid lines) for S_{11} and S_{21} in the frequency range from 45 MHz-10 GHz for a 10 μm wide and 95 μm long poly resistor implemented in the poly1 layer.

Parameter	Extracted Value	Parameter	Extracted Value
R_{poly} [Ω]	208	L_{poly} [pH]	371
C_{ox} [fF]	40	R_{sub} [Ω]	50

Table 4.10 Extracted values of equivalent circuit element for poly resistor. The poly resistor is implemented in the poly1 layer with line length of 95 μm and line width of 10 μm .

was calibrated using a Cascade ISS calibration substrate placing the reference plane for the measurements at the probetips. The circuit operated at a supply voltage of 5 V for V_{cc} , and the control voltage V_{bias} was adjusted until a bias current of 2.85 mA was obtained. An additional bias of 2.5 V was applied at the input of the differential stage through bias-T's at port 1 and port 2. Two sets of measurements were performed. First S-parameters were measured from port 1 to port 3 with port 2 and port 4 terminated in matched loads and secondly from port 1 to port 4 with port 2 and 3 terminated. For these measurements Cascade WPH-705-PPGSGSGP probes were used.

In order to investigate the prediction accuracy of the measured magnitude and phase characteristics of S_{31} and S_{41} , as well as the input and output return losses of interest for the SiGe HBT differential amplifier, three levels of simulation complexity are used. The first level is a nominal simulation performed on the ideal SiGe HBT differential amplifier using the extracted VBIC95 model. The second level of simulation complexity takes the pad structures and interconnect lines parasitics for the input, output, supply and ground lines into account. The third level also takes the load resistor parasitics into account.

From the nominal simulation, a 3 dB bandwidth of 4.6 GHz was expected, however the measurement shows a disappointing 3 dB bandwidth of 2.4 GHz for S_{31} and 2.7 GHz for S_{41} as shown in Fig. 4.31. The difference in 3 dB bandwidth between S_{31} and S_{41} is an indicator of the imbalance in the differential amplifier. Also the phases of S_{31} and S_{41} are far from expectations as are the input and output return losses as shown in Fig. 4.32. Clearly the frequency response of the SiGe HBT differential amplifier is affected by other factors than the SiGe HBT device performance. It should be notice that little difference was observed between the prediction ability of the design-kit model and the extracted VBIC95 model. Taking into account the substrate

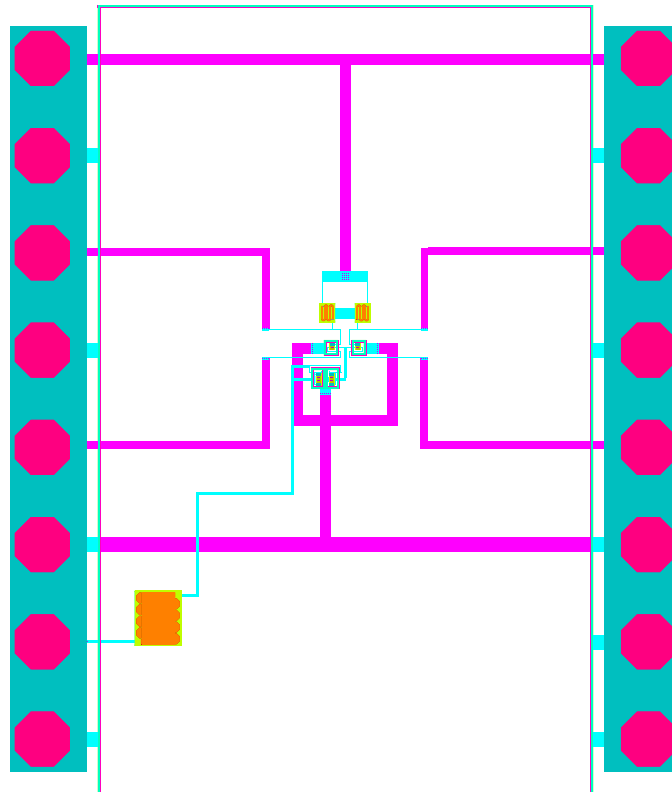


Figure 4.30 Layout of SiGe HBT differential amplifier.

effects due to pads structure and interconnect lines, the frequency response of the differential amplifier becomes well-predicted. The interconnect lines parasitics is very important in order to model correctly the phase characteristic in the SiGe HBT differential amplifier. As observed in Fig. 4.31 and Fig. 4.32 the simulation results with inclusion of poly resistor parasitics coincide with the simulation with pad structure and interconnect lines parasitics. This could however, be expected as the large pad and interconnect line capacitances dominate the output capacitive loading of the SiGe HBT differential amplifier.

In conclusion, the present investigation have shown that the frequency response of basic circuit configurations depends to a large extent on substrate effects. Nominal simulation including only the frequency dependence of the SiGe HBT devices fails to predict the measured bandwidth capability and phase characteristics even in basic circuit configurations. Inclusion of substrate effect parasitics associated with pad structures and interconnect lines are found important in order to let simulation predict measured results with respect to the frequency response of a SiGe HBT differential amplifier. Poly resistors show only weak frequency dependence and the parasitics associated with these resistors do not influence the prediction of measured results. All following simulation results presented for SiGe HBT circuits includes the parasitics from the most critical interconnect lines and pad structures while the influence from the poly resistor parasitics is neglected.

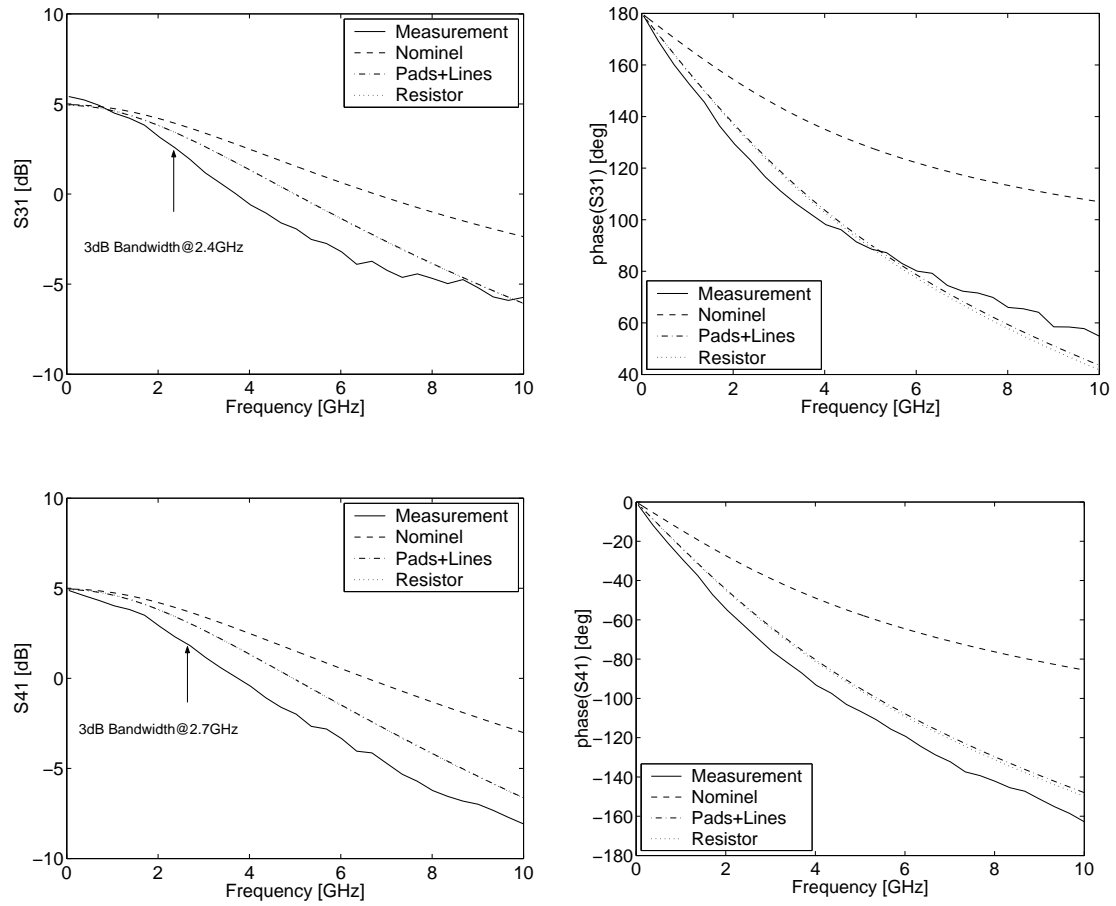


Figure 4.31 Comparison of simulated and measured magnitude and phase characteristics for SiGe HBT differential amplifier in the frequency range from 45 MHz-10 GHz. Top left: $\text{dB}(S_{31})$. Top right: $\text{phase}(S_{31})$. Bottom left: $\text{dB}(S_{41})$. Bottom right: $\text{phase}(S_{41})$.

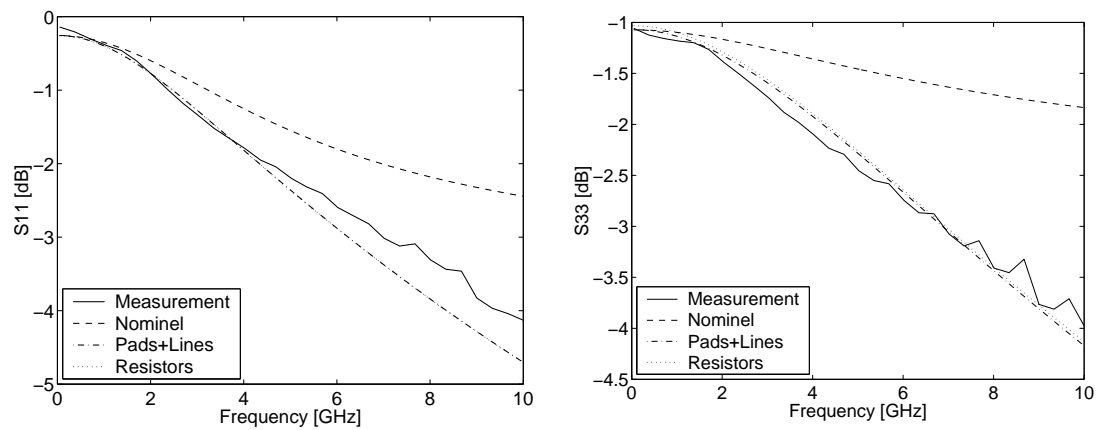


Figure 4.32 Comparison of simulated and measured return losses for SiGe HBT differential amplifier in the frequency range from 45 MHz-10 GHz. Left: Input return loss. Right: Output return loss.

Chapter 5

SiGe HBT Designs for Quadrature Modulator/Demodulator Subsystem

The quadrature modulator/demodulator subsystem is one of the most important building blocks in wideband SAR systems as it is required in all sensors. Quadrature modulators and demodulators for SAR systems have previously been developed using connectorized components. This approach becomes ineffective as the bandwidth requirement increases. Instead, monolithic microwave integrated circuits (MMIC's) should be used to implement these subsystem in order to meet the stringent transfer function requirements over the signal bandwidth, minimize quadrature modulator/demodulator imperfections, and reduce size and cost. SiGe HBT technology seems to be well suited for the implementation of key components performing quadrature modulation and demodulation in a SAR system.

Typical specifications for a quadrature modulator/demodulator subsystem in a wideband SAR system have been discussed in chapter 2 of this thesis, however nothing was decided about the actual implementation of the SiGe HBT MMIC's. In the present chapter, possible implementations of the SiGe HBT MMIC's for the quadrature modulator/demodulator subsystem will be discussed.

The wideband operation with resulting stringent requirements on gain flatness and phase linearity in the quadrature modulator/demodulator have lead to a choice of a bottom-up design approach. This means that in order to implement the SiGe HBT MMIC's for the quadrature modulator/demodulator, the suitability of basic circuit configurations for a wideband SAR systems have been investigated. In particular, wideband SiGe HBT active mixers and wideband input buffer designs have been investigated in the present work. Though wideband active mixers have been reported in Si/SiGe bipolar technologies [19, 20, 22, 23, 26, 77, 78], these have mostly been optimized for downconversion performance in wireless applications. Such active mixers are capable of frequency conversion of narrowband signals over a wide range of input frequencies to a fixed low output frequency. This differs from the demands on the wideband active mixers for SAR applications. For active mixers in SAR applications, a wideband signal at the input port should be converted undistorted in amplitude and phase to the output port. Thus active mixers for quadrature modulation and demodulation in SAR applications must exhibit wideband operation on both the input and output ports. In order to meet these demands, a basic understanding of the main bandwidth limitations of the Gilbert Cell mixer are needed. Therefore, a simplified time-varying small-signal model for analyzing the frequency response of the Gilbert Cell mixer is proposed. The analysis of the main bandwidth limitation of the Gilbert Cell mixer shows that it is in general possible to consider RF separately the frequency response on the RF and IF port. The frequency response on the RF port is limited by the input bandwidth

of the transistors in the lower differential pair of the Gilbert Cell mixer while the IF port bandwidth limitation arises due to the capacitive loading at the output nodes. Using the knowledge obtained from the frequency response analysis, suitable circuit techniques are described, useful when the objective is to achieve wideband operation at both the input and output port of the mixer. The experimental results for an active mixer implemented in the $0.8\mu\text{m}$ SiGe HBT process from AMS are well predicted by simulations and have sufficient bandwidth performance on both the input port and output port to be used in the quadrature modulator and demodulator subsystem. Wideband input buffers are needed for adaption to the quadrature mixers and should perform signal level adjustment, DC offset adjustment, input matching and single-ended to differential conversion. An input buffer approach using a differential amplifier stage with shunt feedback has been implemented in the $0.8\mu\text{m}$ SiGe HBT Process from AMS. The experimental results for these input buffers demonstrates wideband performance, although the bandwidth is somewhat lower than expected from simulations.

Finally, a system design simulation setup is described which is capable of predicting the performance of the SiGe HBT MMIC designs in terms of the PSLR and ISLR quantities of interest for high resolution SAR applications. The quantities are evaluated by matched filtering of the base-band quadrature signals, similar to what is done in a real SAR system.

5.1 Quadrature Modulator/Demodulator Configuration

Block diagrams for the quadrature modulator and demodulator are shown in Fig. 5.1. Both consist of a 90° phase shifter and the modulator/demodulator core. The modulator core should be implemented as one SiGe HBT MMIC and contains two double-balanced wideband active mixers with their output currents combined together, input buffers for input matching, DC offset adjustment as well as single-to-differential conversion, and an output buffer. The demodulator core should also be implemented as one SiGe HBT MMIC, and contains two double-balanced wideband active mixers, an input buffer for wideband input matching as well as single-to-differential conversion, and two output buffers with DC offset adjustment. Several approaches exist for monolithic integration of the 90° phase shifter together with the quadrature modulator/demodulator [79–83]. These however, are either relatively narrowband or inaccurate and conflict with the modular design principle for future SAR systems where a change in local oscillator frequency should not require a full redesign of the quadrature modulator/demodulator chipset.

It will be attempted to reuse the designed double-balanced wideband active mixers¹ and input buffers for both the quadrature modulator and demodulator. This is in agreement with the bottom-up design approach mentioned in the beginning of this chapter.

5.2 Wideband SiGe HBT Active Mixer Design

Wideband SiGe HBT active mixers based on the Gilbert Cell mixer topology [16] is generally preferred for quadrature modulator/demodulator designs due to its double-balanced operation. Double-balanced mixers are needed to suppress LO leakage to the output in the quadrature modulator [81] and to prevent DC-offsets due to LO self-mixing in the quadrature demodulator [84].

¹The output buffers are considered to be a part of the active mixers, and will not be given special attention in this work.

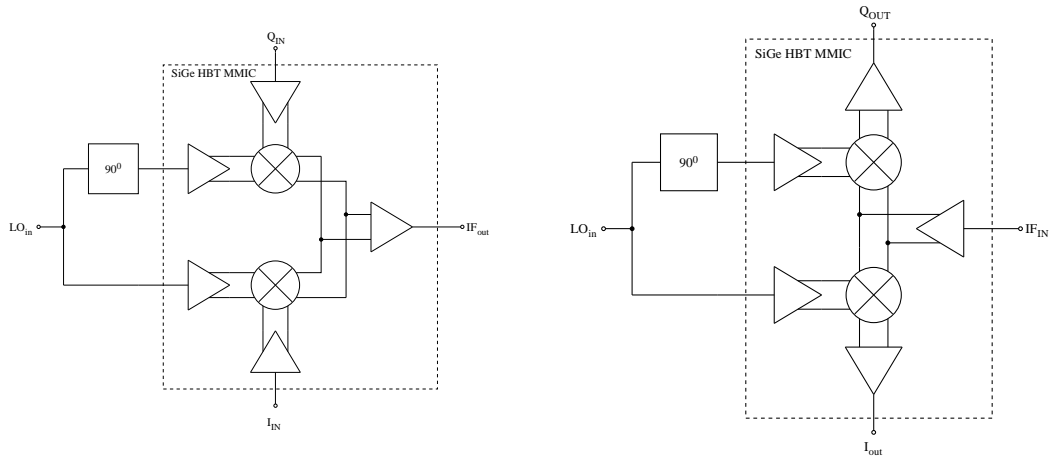


Figure 5.1 Block Diagrams for quadrature modulator/demodulator showing possible implementations of SiGe HBT MMIC's. Left: Quadrature modulator. Right: Quadrature demodulator.

5.2.1 Bandwidth Limitation of The Gilbert Cell Mixer

The Gilbert Cell mixer topology shown in Fig. 5.2 consist of a quasi-linear transconductance input stage (Q_1 - Q_2), a switching quad (Q_3 - Q_6) and finally an output stage consisting here of the load resistance (R_L). The transconductance input stage converts the RF voltage signal into a current which ideally is multiplied by ± 1 at the rate of the LO frequency by the switching quad, enabling the wanted frequency conversion. While it is in principle possible to interchange the RF and LO signals, it is preferred to apply the RF signal to the lower differential pair of the Gilbert Cell mixer due to reduced Miller effect [18].

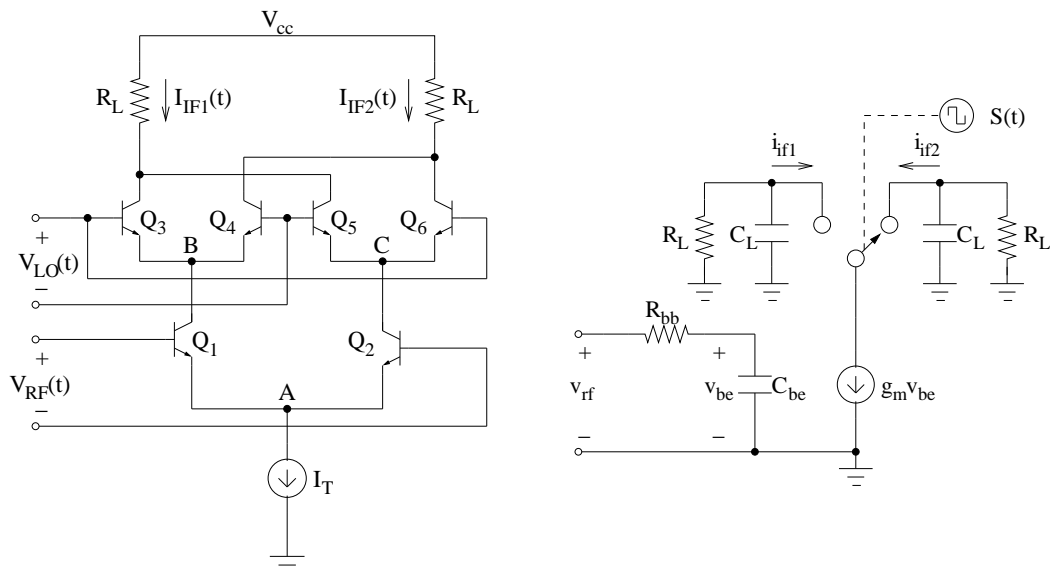


Figure 5.2 Left: The Gilbert Cell mixer topology. Right: Time-varying small-signal model for frequency response analysis.

The analysis of the frequency response of the Gilbert Cell mixer is based on the simplified

time-varying small-signal model shown in Fig. 5.2 where R_{bb} is the total base resistance. The switching quad is represented as an ideal polarity-switch [85] as

$$S(t) = \frac{4}{\pi} \cos(\omega_{LO}t) - \frac{4}{3\pi} \cos(3\omega_{LO}t) + \frac{4}{5\pi} \cos(5\omega_{LO}t) - \dots \quad (5.1)$$

where ω_{LO} is the LO angular frequency. The switching process eventually becomes limited by the unity current gain frequency, f_T , of the transistors in the quad. For frequencies below f_T , instantaneous switching of the quad can be assumed and the representation as an ideal polarity-switch is valid. Due to the symmetry of the Gilbert Cell mixer, point A in Fig. 5.2 is virtual ground for the RF signal, and a differential-mode half-circuit is sufficient for analysis [86]. As point B and C are virtual ground for the LO signal, the lower differential pair is assumed to be time-invariant. Assuming instantaneous switching of the quad points, B and C present, at all times low impedance points for the RF signal due to the resulting Cascode connection. This justifies the neglect of the internal feedback capacitance in the lower differential pair, because of the reduced Miller effect, as well as any capacitive loading that might exist at points B and C. The capacitive loading C_L at the output consists mainly of the sum of the collector-substrate and base-collector capacitances for the transistor pairs $Q3, Q5$ and $Q4, Q6$. While the capacitive loading is modulated by the LO signal, and C_L in principle is time-varying, the effect on the frequency response is believed to be very small and a fixed value can be assumed. The presence of the large LO signal and the small RF signal in the Gilbert Cell mixer in general results in mixing frequencies in the output currents i_{if1} and i_{if2} at [87]

$$\omega_{mix} = \pm\omega_{RF} + n\omega_{LO} \quad (5.2)$$

where ω_{RF} is the RF angular frequency and $n = \dots, -2, -1, 0, 1, 2, \dots$ as illustrated in Fig. 5.3a). An equivalent representation is shown in Fig. 5.3b) where only the components at frequencies

$$\omega_n = \omega_0 + n\omega_{LO} \quad (5.3)$$

with $\omega_0 = |\omega_{LO} - \omega_{RF}|$ have been included. That is, only the positive components of the upper sidebands and the negative components of the lower sidebands are included in this representation. However, because positive and negative frequency components are related as $i_{-n} = i_n^*$ knowledge of one sideband component is sufficient. With this notation the RF signal is at frequency ω_1 for low-side mixing (LO frequency below RF frequency) and at frequency ω_{-1} for high-side mixing (LO frequency above RF frequency). Considering low-side mixing only, conversion matrix analysis is applied in order to find the conversion transconductance from the RF input voltage $v_{rf,1}$ into the differential IF output current at the IF frequency ω_0 . The transconductance stage consists only of time-invariant elements, and is easily analyzed. The current components i_n from the transconductance stage then only includes frequency components already present in the RF input voltage signal as illustrated by the following equation

$$i_1 = \frac{g_m}{1 + j\frac{\omega_1}{\omega_v}} v_{rf,1} \quad (5.4)$$

where the input angular bandwidth $\omega_v = 1/(C_{be}R_{bb})$ for the transistors has been used. The conversion from the only nonzero current component i_1 from the transconductance stage into the differential IF output current components becomes

$$\frac{1}{2} \begin{bmatrix} i_{if1,-2}^* - i_{if2,-2}^* \\ i_{if1,-1}^* - i_{if2,-1}^* \\ i_{if1,0} - i_{if2,0} \\ i_{if1,1} - i_{if2,1} \\ i_{if1,2} - i_{if2,2} \end{bmatrix} = \begin{bmatrix} 0 & \frac{2}{\pi} & 0 & -\frac{2}{3\pi} & 0 \\ \frac{2}{\pi} & 0 & \frac{2}{\pi} & 0 & -\frac{2}{3\pi} \\ 0 & \frac{2}{\pi} & 0 & \frac{2}{\pi} & 0 \\ -\frac{2}{3\pi} & 0 & \frac{2}{\pi} & 0 & \frac{2}{\pi} \\ 0 & -\frac{2}{3\pi} & 0 & \frac{2}{\pi} & 0 \end{bmatrix} \begin{bmatrix} 0 \\ 0 \\ 0 \\ i_1 \\ 0 \end{bmatrix} \quad (5.5)$$

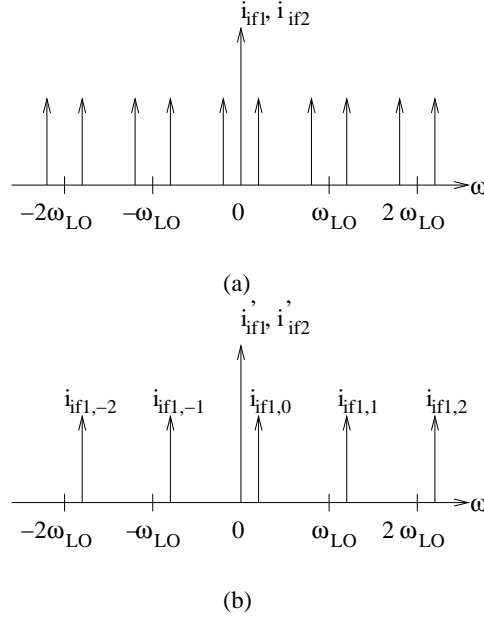


Figure 5.3 Spectrum of mixing frequencies in output currents i_{if1} and i_{if2} . (a) Spectrum for i_{if1} and i_{if2} shown for $|n| \leq 2$. (b) Equivalent representation showing positive components for the upper sidebands and negative components for the lower sidebands. The prime is used to indicate that i'_{if1} and i'_{if2} are not the full spectrum's.

where the Fourier coefficients of the polarity switching function $S(t)$ have been applied. From Equations 5.4 and 5.5 it follows that the frequency response of the conversion transconductance G_{cnv} is given as

$$G_{cnv} = \frac{2}{\pi} \frac{g_m}{1 + j\omega_1/\omega_v} \quad (5.6)$$

from which the main frequency limitation in the conversion from an RF input voltage into the differential IF output current seems limited by the input bandwidth of the transistors in the lower differential pair. For low frequencies ($\omega_1 \ll \omega_v$) the above equation becomes identical with previous reported results for the conversion transconductance [88], verifying the analysis approach. The differential IF output current flows through the reactive load consisting of R_L and C_L and is thus converted into a differential IF output voltage. The voltage conversion gain G_{av} then becomes

$$G_{av} = \frac{2}{\pi} \frac{g_m R_L}{(1 + j\omega_1/\omega_v)(1 + j\omega_0/\omega_L)} \quad (5.7)$$

where $\omega_L = 1/(R_L C_L)$. This equation shows that the two main bandwidth limiting mechanisms in the Gilbert Cell mixer can be separated into limitations on the RF and IF port respectively. First it is seen that the frequency response at the input port depends on the input bandwidth of the transistors in the transconductance stage. This in turn depends on the unity current gain frequency f_T as

$$\omega_v = 2\pi f_v = \frac{2\pi f_T}{g_m R_{bb}} \quad (5.8)$$

explaining the good correlation between RF port bandwidth for active mixers and f_T observed in chapter 3. Second of all, it is found that the frequency response at the output port depends on the capacitive loading at the output nodes of the Gilbert Cell mixer. This is in agreement with the observed dependence of the output port bandwidth on f_{max} in chapter 3. High f_{max} demands tight transistor structures. Tight transistor structures, in general, have low parasitic capacitances.

As an example, consider a Gilbert Cell mixer designed for a voltage conversion gain of 20 dB using $4 \times 0.8 \mu\text{m}^2$ area SiGe HBT devices from the $0.8 \mu\text{m}$ AMS process. For a tail bias current of $I_T = 2.8 \text{mA}$ the RF port bandwidth is calculated using extracted values as

$$f_v = \frac{1}{2\pi C_{be}(R_{bx} + R_{bi})} = 4.73 \text{GHz}. \quad (5.9)$$

The 20 dB gain requirement translates into a load resistance $R_L = 287 \Omega$ from which the IF port bandwidth is calculated as

$$f_L = \frac{1}{2\pi(2C_{bcp} + 2C_{bep} + 2C_{bc} + 2C_{bco})R_L} = 8.81 \text{GHz}. \quad (5.10)$$

These should be taken as best case bandwidth estimates, as the influence from input and output buffers, poly resistor, and interconnect line parasitics have not been considered. It thus seems necessary to exploit advanced circuit techniques for extending the RF and IF port bandwidth of the Gilbert Cell mixer.

5.2.2 The Principle of Strong Impedance Mismatch

The schematic of a wideband SiGe HBT active mixer design is shown in Fig. 5.4. The Gilbert Cell mixer uses emitter degeneration for the transconductance stage and a shunt feedback stage for the load circuit. Resistive emitter degeneration R_e in the transconductance stage allows a significant extension of the RF port bandwidth. This is at the expense of reduced conversion gain, however. A peaking capacitor C_e is used to extend the bandwidth with relaxed resistive emitter degeneration. The shunt feedback stage provides a low impedance at the output node of the Gilbert Cell mixer which increases the output port bandwidth. Furthermore, the transfer function of the shunt feedback stage may have two complex conjugated poles with possible improvement in bandwidth by high-frequency peaking [89]. The shunt feedback stage has several advantages compared to other circuit techniques suitable for extending the output port bandwidth. The output port bandwidth depends on the time constant at the output nodes of the switching quad so the obvious solution would be to lower the value of the load resistor [18]; this however lowers the conversion gain as well, and a high-gain output buffer might be needed. In another method [78], a common-base stage is inserted between the switching quad and the load. This reduces the impedance at the output nodes of the Gilbert Cell mixer, however, with limited head-room for the circuit. A straight-forward technique suitable for low-voltage designs is to use a reactive load [26]. This approach however, requires on-chip inductors with high self-resonance frequency which are usually not available in Si/SiGe Bipolar technologies. The shunt feedback stage extends the bandwidth of the output port without sacrificing conversion gain. If the current in the load circuit is kept small, the head-room limitations are reduced. The present wideband SiGe HBT active mixer design follows the principle of strong impedance mismatch between succeeding stages [90, 91]. The benefits of this principle for wideband circuit design are as follows:

- Reduced influence from frequency dependent input and output impedances.
- All circuit nodes are low impedance meaning reduced influence from parasitic capacitances.
- At high frequency where the mismatch is degraded the input and output impedances approaches complex conjugated pairs further extending the bandwidth [92].

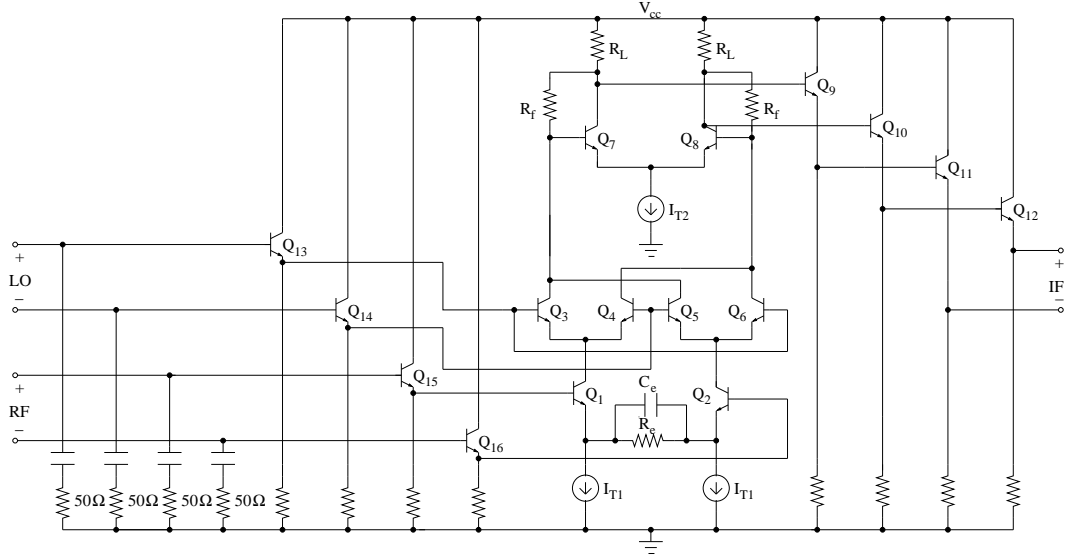


Figure 5.4 Wideband SiGe HBT active mixer with emitter degeneration of transconductance stage and shunt feedback load circuit. Input and output emitter followers are used for improved impedance mismatch between stages.

The emitter followers are included for improved mismatch between succeeding stages as well as level shifting and buffering. Impedance match at the RF and LO ports is provided by ac-coupled 50Ω shunt resistors. This simple scheme allows for the beneficial use of the input wirebond inductance in an MCM environment to further improve the return loss [91].

The transconductance stage with emitter degeneration can be analyzed using the equivalent circuit shown in Fig. 5.5. The transfer function from the input RF voltage v_{rf} to the output

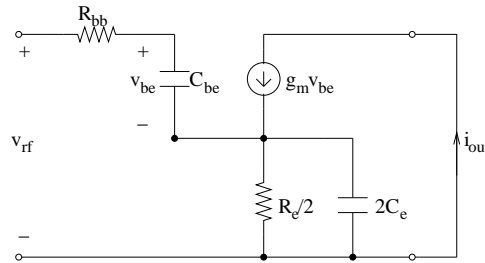


Figure 5.5 Equivalent circuit of transconductance stage with emitter degeneration.

current i_{out} is expressed as

$$\frac{i_{out}(s)}{v_{rf}(s)} = \frac{g_m}{1 + g_m R_e/2} \frac{1 + sC_e R_e}{1 + \frac{C_e R_e + C_{be}(R_{bb} + R_e/2)}{1 + g_m R_e/2} s + \frac{C_{be} R_{bb} C_e R_e}{1 + g_m R_e/2} s^2} \quad (5.11)$$

and, as expected, shows a reduction in low frequency transconductance gain. If the capacitor C_e is not present and the transconductance stage is heavily degenerated, e.g if $g_m R_e/2 \gg 1$, then the transconductance gain approach $2/R_e$ and the bandwidth approaches f_T . The capacitor C_e generates a zero in the transfer function at $-1/C_e R_e$ which can be used to peak the transconductance gain at high frequencies with relaxed emitter degeneration. The influence of the peaking capacitor on the gain flatness and phase linearity of the transconductance stage is found by simulations on the equivalent circuit shown in Fig. 5.5. From the frequency response of the transconductance gain and phase shown in Fig. 5.6 it is observed that an optimal value of the peaking capacitor C_e exist with respect to bandwidth extension, gain flatness, and linear phase characteristic.

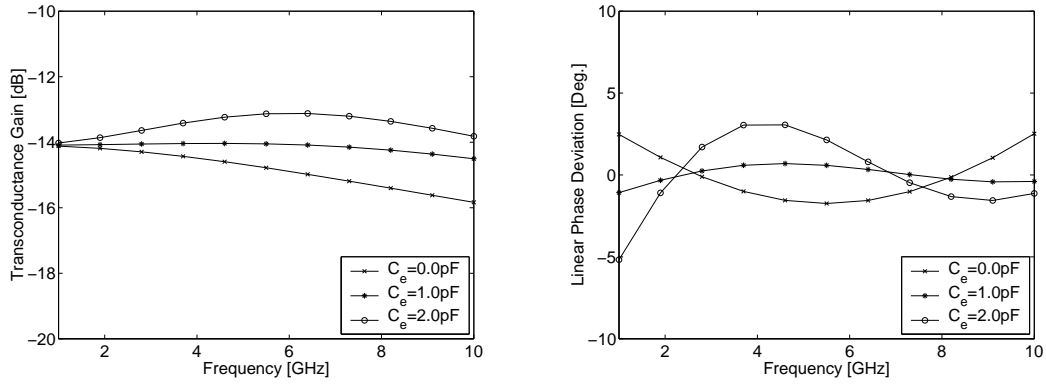


Figure 5.6 Typical frequency response for transconductance stage with emitter degeneration for different peaking capacitors C_e . Assumes a $4 \times 0.8 \mu\text{m}^2$ area SiGe HBT device biased at peak f_T . Left: Transconductance gain. Right: Deviation from linear phase response.

The shunt feedback load circuit is most easily analyzed using feedback theory [93]. In order to apply feedback theory, the equivalent circuit shown in Fig. 5.7 has been applied. A number of approximations have been used to simplify the analysis. First, it is assumed that the signal fed back through the device is much smaller than the signal fed back through R_f , so that the base-collector capacitance can be neglected. It is further assumed that the forward transmission through the feedback resistance is negligible compared with the transmission through the device because the latter has gain. The complex load consists of a parallel combination of the load resistance R_L and parasitic capacitance C_L . The parasitic capacitance consists of the collector-substrate capacitance of the differential transistor pair $Q_7 - Q_8$, the base-collector capacitance of the emitter follower transistors $Q_9 - Q_{10}$, and interconnect line parasitics in the active mixer circuit shown in Fig. 5.4. The basic amplifier open loop gain, a , and feedback network transfer

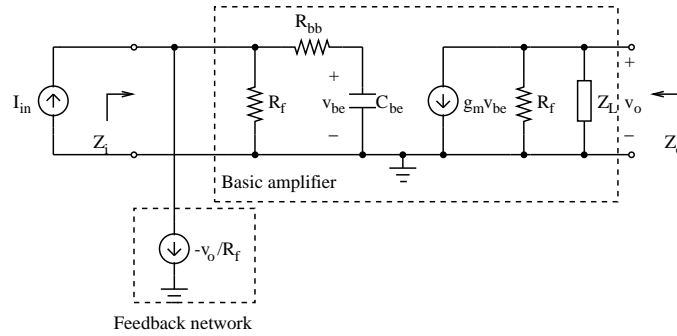


Figure 5.7 Equivalent circuit of shunt feedback load circuit. The loading due to the feedback network is absorbed in the basic amplifier.

function, f , are found from Fig. 5.7 as

$$a = \frac{-g_m R'_L R_f}{(1 + s(R_f + R_{bb})C_{be})(1 + sR_L C_L)} \quad (5.12)$$

and

$$f = -\frac{1}{R_f} \quad (5.13)$$

respectively, where $R'_L = R_L R_f / (R_L + R_f)$ is the effective load resistance when the loading effect from the feedback network is taken into account. From [93] the input impedance of this circuit

is given as

$$Z_i = \frac{Z_{ia}}{1 + af} \quad (5.14)$$

where Z_{ia} is the input impedance of the transistor with the loading due to the feedback network absorbed. Inserting Equation 5.12 and Equation 5.13 into the expression for the input impedance gives

$$Z_i = \frac{R_f}{1 + g_m R'_L} \frac{1 + s R_{bb} C_{be}}{1 + s(R_f/(1 + g_m R'_L) + R_{bb})C_{be}} \quad (5.15)$$

where it has been assumed that the time constant $R_L C_L$ is unimportant for the frequency response of the input impedance. From Equation 5.15 a reduction in the input impedance is observed, beneficial for wideband operation at the output port of the Gilbert Cell mixer. Similar, the output impedance looking from the emitter followers back into the load circuit is expressed as

$$Z_o = \frac{R'_L}{1 + g_m R'_L} \frac{1 + s(R_f + R_{bb})C_{be}}{1 + s \frac{(R_f + R_{bb})C_{be}}{1 + g_m R'_L}} \quad (5.16)$$

where it again has been assumed that the $R_L C_L$ time constant is negligible. If the low frequency loop gain $|a_v| = g_m R'_L$ is large, the output impedance shows an inductive component (rise with frequency). The input impedance of an emitter follower has a capacitive component at high frequencies, thus a complex conjugated match may exist at the interface between the shunt feedback stage and the emitter follower stage. The transfer function for the transimpedance gain can be represented by a second order response as

$$\frac{v_o}{i_{in}} = \frac{a}{1 + af} \approx \frac{-R_f}{1 + s \frac{2k}{\omega_0} + \frac{s^2}{\omega_0^2}} \quad (5.17)$$

where

$$\omega_0 = \sqrt{\frac{|a_v|}{C_L R'_L (R_f + R_{bb}) C_{be}}} \quad (5.18)$$

and

$$k = \frac{1}{2} \sqrt{\frac{(C_L R'_L + (R_f + R_{bb}) C_{be})^2}{|a_v| C_L R'_L (R_f + R_{bb}) C_{be}}} \approx \frac{1}{2} \sqrt{\frac{((R_f + R_{bb}) C_{be})}{|a_v| C_L R'_L}} \quad (5.19)$$

are the natural angular frequency and the damping factor respectively. The approximation in Equation 5.19 is valid if $C_L R'_L \ll (R_f + R_{bb}) C_{be}$, which is normally the case. The frequency ω_0 determines the bandwidth of the shunt feedback load circuit². The frequency response peaks when the damping factor becomes $k < 1/\sqrt{2}$. In general, the following observations regarding bandwidth and peaking of the frequency response for the shunt feedback load circuit are made:

- For increasing loop gain, the bandwidth increases, once $k < 1/\sqrt{2}$ however, the frequency response peaks (optimal loop gain exist).
- For increasing feedback resistance the bandwidth decreases (conversion gain versus bandwidth trade-off).
- For increasing load capacitance C_L , the bandwidth decrease and the frequency response peaks (however, capacitive loading is necessary for achieving gain flatness).

²At ω_0 the transimpedance gain is down by $2k$ compared with the low-frequency value.

The derived expression for ω_0 and k differs from is found in the literature, e.g. [89]. In the referenced work, the influence of the load capacitance C_L is neglected. Following the above discussion it should be obvious that both ω_0 and k depends to a large extent on the load capacitance. To elaborate further on this point, simulation on an equivalent circuits for the the shunt feedback stage has been performed for several values of the load capacitance C_L . The results are shown in Fig. 5.8 (left plot), and agrees well with the theoretical predictions. Without the presence of a load capacitance, the transimpedance gain has a first order response and no peaking occurs. To high a value of the load capacitance leads to a significant peaking in the frequency response, which deteriorates the linear phase response as shown in Fig. 5.8. For a given loop gain an optimal value of load capacitance exists, where both bandwidth extension, gain flatness and linear phase characteristic occurs. This shows the importance of properly optimizing the transistors in the differential stage as well as the emitter followers in the next stage. The conversion gain of the Gilbert Cell Mixer depends upon R_f but is independent of the loop gain in the shunt feedback stage. Thus, some degree of freedom exists in the design of the shunt feedback load circuit for optimal performance.

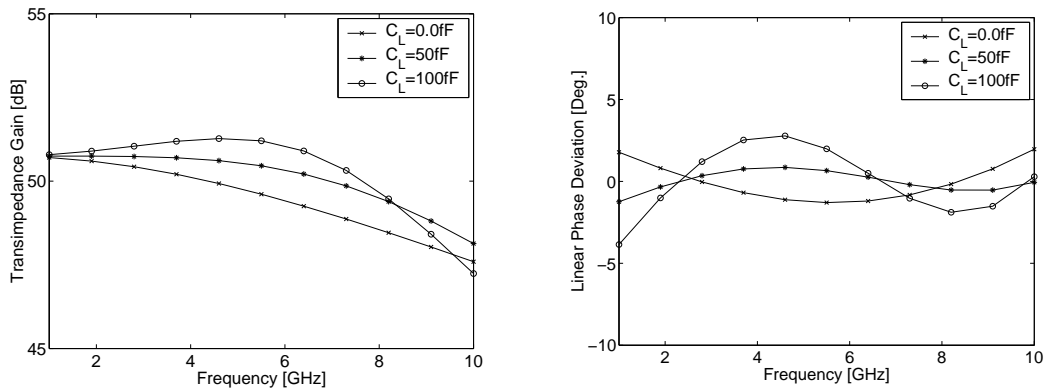


Figure 5.8 Typical frequency response of shunt feedback stage with different capacitance loading C_L . Assumes a $4 \times 0.8 \mu\text{m}^2$ area SiGe HBT device biased at peak f_T . Left: Transimpedance gain. Right: Deviation from linear phase response.

5.2.3 Experimental Results

The wideband SiGe HBT active mixer was implemented in the $0.8 \mu\text{m}$ SiGe HBT process from AMS. The layout of the fabricated circuit is shown in Fig. 5.9. Ground-shielded pads have been used to reduce the influence from substrate effects. Because the AMS SiGe HBT process only has two metal layers available, great care have been taken to minimize interconnect line parasitics. The circuit was laid out in a very compact and highly symmetric manner. An unavoidable asymmetry exists at the crossing of the transistors in the switching quad of the Gilbert Cell mixer. The critical interconnect lines leading from the circuit core to the pads have been laid out in the top metal layer. Special care has been given to shorten the critical interconnect lines between the emitter follower stages. It is well known that capacitive loaded emitter followers may have an input impedance with a negative real component. The low output impedance of the driving emitter follower or load circuit has an inductive component which together with the parasitic inductance from the interconnect lines may lead to on-chip oscillation [91]. Passive components are shielded from the substrate by n-well shields. The power supply is decoupled on-chip with a 17.85pF capacitor. The chip size including pads is $0.9 \times 0.9 \text{mm}^2$.

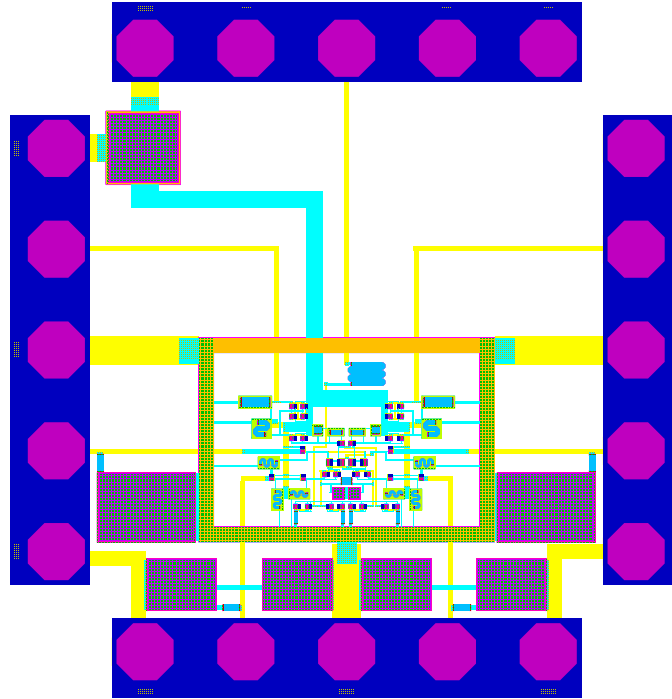


Figure 5.9 Layout of wideband SiGe HBT active mixer.

Measurement Condition and Experimental Setup

The circuit was measured on-wafer using a Cascade probe station with Cascade GSGSG probes for connecting to the mixer ports and Cascade WPH-705-150-PPPPP power probes for the bias supply. The measurement setup is shown in Fig. 5.10. The circuit was biased from a 5V supply voltage (V_{cc}) and a current consumption of 34mA was obtained by adjusting V_{bias} . Bias for the LO and RF port were applied through bias-T's. All measurements have been taken single-ended by terminating the unused ports in 50 Ω loads. The output spectrum at the IF-port was measured using a HP 8563E spectrum analyzer. For RF and LO port frequencies above 2 GHz, HP 8672A and HP 8671B synthesized CW signal generators (2-18 GHz) were used. For measurement below 2 GHz, the internal generator of the HP 8510B network analyzer was applied to the RF port and a SMIQ03 signal generator from Rohde and Schwarz (300KHz-3.3GHz) was used for the LO port. The frequency dependent losses in the cables and probe heads were estimated using a through line from an ISS calibration substrate and subtracted from all measurements results. Measurement of the active mixer phase characteristic was not possible using the available equipment.

Measurement Results and Discussion

The first issue in the verification of the active mixer is to find the optimum input power at the LO-port. The quantity of main interest in mixer measurements is the power conversion gain, defined as the ratio between the power delivered to the load (the spectrum analyzer) to the power available from the generator. In Fig. 5.11, the measured down-conversion gain versus LO power is shown for a LO frequency of 1.25 GHz and RF frequency of 1.65 GHz. At low LO power levels, the conversion gain depends linearly on the applied LO-power because the transistors in the quad do not have sufficient signal drive to operate as current switches. As the LO power level increase, an optimum is reached where the assumption of ideal current switches applies. Beyond this optimum point, the transistors in the switching quad saturate and the conversion

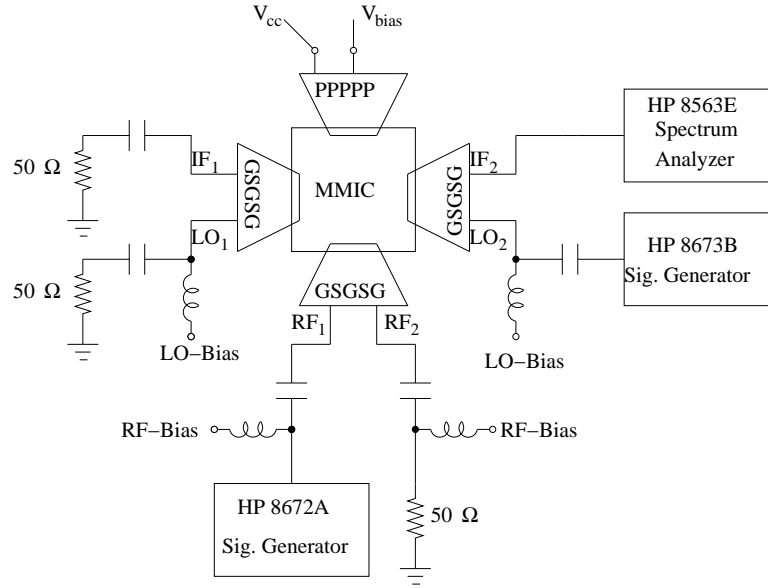


Figure 5.10 Experimental Setup.

gain drops. All succeeding measurement results are based on an LO power level of 0 dBm where the conversion gain is maximized. An input RF power level of -18 dBm was measured at 1dB conversion gain compression. An RF power level of -30 dBm was used in the measurements to ensure that the active mixer was not compressed. The bandwidth limitation of the active mixer

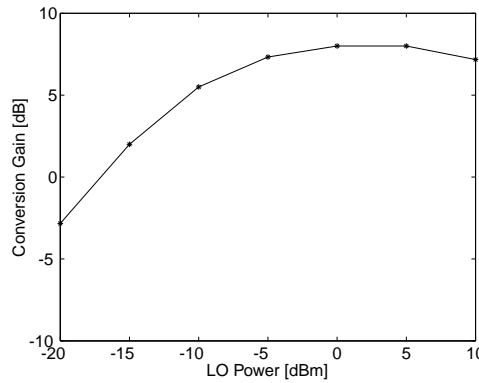


Figure 5.11 Conversion Gain versus LO power ($F_{LO} = 1.25\text{GHz}$, $F_{RF} = 1.65\text{GHz}$, $F_{IF} = F_{RF} - F_{LO} = 0.4\text{GHz}$).

is shown in Fig. 5.12. With both RF and LO ports swept in frequency with a fixed IF frequency of 0.4 GHz, a conversion gain of 8.5 dB and a 3dB bandwidth of 11 GHz was achieved. A 3dB bandwidth of 7.5 GHz was achieved with both RF and IF port swept in frequency and a fixed LO frequency of 2 GHz. These measured results are very well predicted by simulation. As shown in Fig. 5.13 the LO suppression at the IF port is better than -30 dB below 2 GHz and better than -25 dB up to 16 GHz despite the single-ended operation of the Gilbert Cell mixer. Applying single-ended to differential conversion at the LO port would improve the LO suppression even further. Fig. 5.14 shows the RF and IF port return loss which has been found from on-wafer S-parameter measurements on the mixer circuit. A reasonably good return loss below -17 dB is observed at L-Band for the RF port due to the ac-shunted 50Ω resistors while the IF port return loss is very poor due to the low output impedance of the emitter followers in the output buffer. The IF return loss, however, is not well predicted by simulation even though parasitics due to interconnect lines have been included. The ripples observed at high frequencies in the IF port

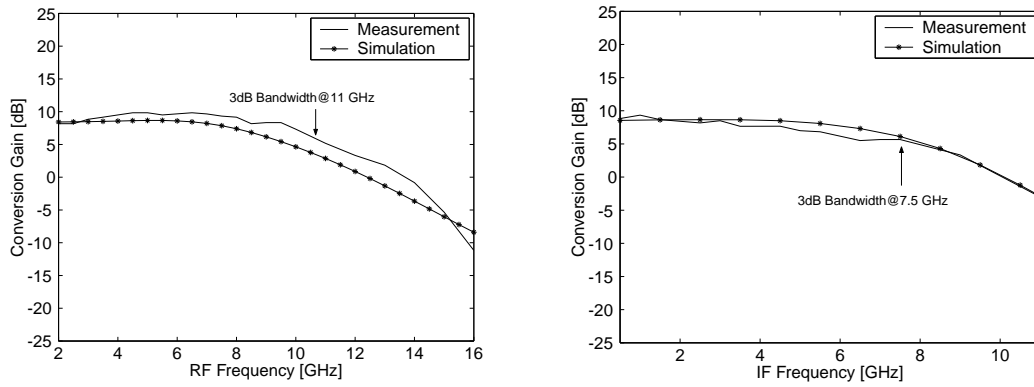


Figure 5.12 Comparison of measured and simulated input (RF) and output (IF) port bandwidth limitation. Left: Conversion gain with swept RF-frequency and fixed IF-frequency ($F_{IF} = F_{LO} - F_{RF} = 0.4\text{GHz}$). Right: Conversion gain with swept IF-frequency and fixed LO-frequency ($F_{LO} = 2\text{GHz}$, $F_{IF} = F_{RF} - F_{LO}$).

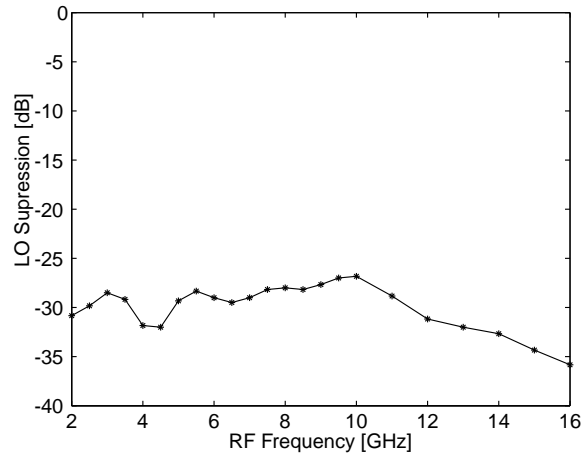


Figure 5.13 LO suppression at the IF port versus RF port frequency ($F_{IF} = F_{LO} - F_{RF} = 0.4\text{GHz}$).

return loss is very likely a manifestation of the problem with capacitive loaded emitter followers as mentioned earlier.

After the presentation of the general characteristics for the designed active mixer the, usefulness of the circuit in a quadrature modulator and demodulator for SAR applications will be shown next. In the quadrature modulator and demodulator subsystems, the LO-frequency is fixed and the IF and RF port frequencies are swept over a large bandwidth. The active mixers in this application require flat conversion gain over the full bandwidth covered by the signal at the IF and RF ports in order to modulate/demodulate the signal undistorted. As shown in Fig. 5.15 (left plot) the active mixer is capable of demodulation of a RF input signal with at least a 1.5 GHz signal bandwidth around a 1.25 GHz carrier. The variation in conversion gain over the bandwidth is within ± 0.4 dB. Furthermore it is seen (right plot) that the modulation from a baseband signal covering the frequency range from DC-1.2 GHz onto a 1.25 GHz carrier seems possible. The higher conversion gain at low frequencies is caused by the use of ac-coupled 50 Ω resistors on the input port. In the flat region, the variation over the bandwidth is within ± 0.2 dB. It is believed that these small variations over the covered frequency range are caused mainly by

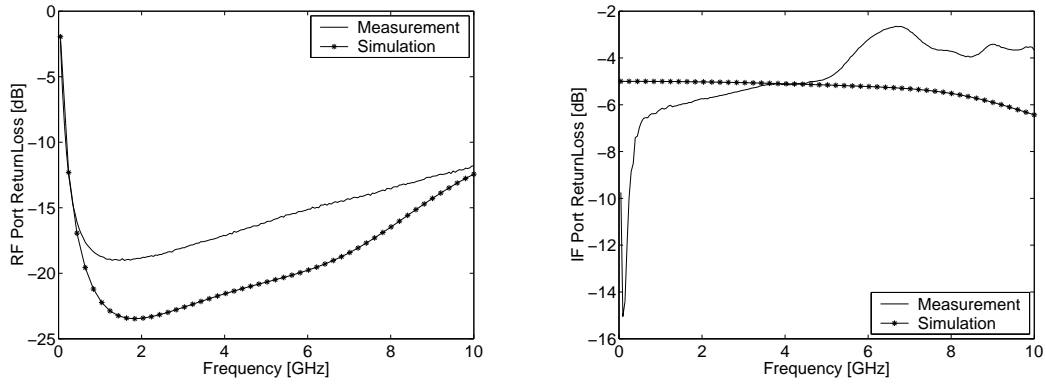


Figure 5.14 Comparison between measured and simulated wideband port return losses. Left: RF port return loss. Right: IF port return loss.

inaccuracy of the spectrum analyzer readings and calibration of cable losses.

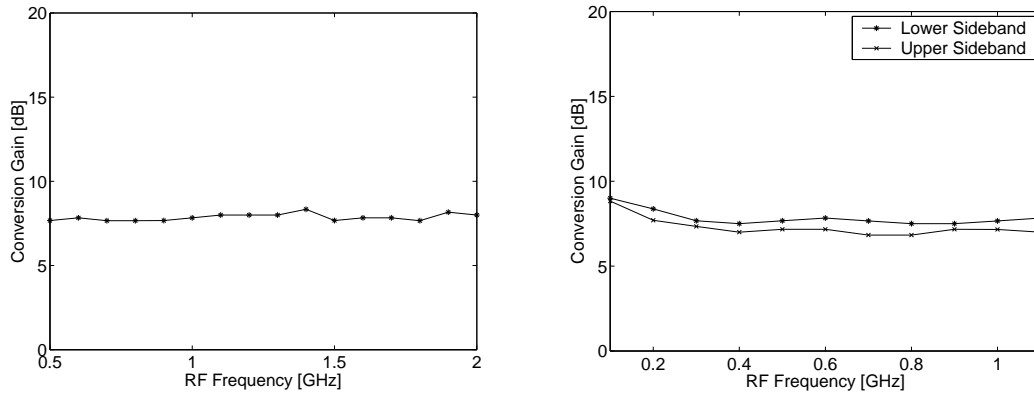


Figure 5.15 L-Band conversion gain. Left: Downconversion gain with fixed LO-frequency and swept RF-frequency ($F_{LO} = 1.25\text{GHz}$, $F_{IF} = |F_{LO} - F_{RF}|$). Right: Upconversion gain with fixed LO-frequency and swept RF-frequency ($F_{LO} = 1.25\text{GHz}$, $F_{USB} = F_{LO} + F_{RF}$, $F_{LSB} = F_{LO} - F_{RF}$).

It is concluded that the designed wideband SiGe HBT active mixer has sufficient bandwidth to be used as quadrature mixers operation in a wideband SAR systems. This has been made possible by careful investigation of the main bandwidth limitation in the Gilbert Cell mixer as well as by exploiting advanced circuit techniques for extending the bandwidth performance at both the RF and IF port. Actually, the designed SiGe HBT active mixer demonstrates state-of-the-art results compared with other wideband active mixers implemented in comparable processes (see chapter 3, Fig. 3.2 and Fig. 3.3).

5.3 Wideband SiGe HBT Input Buffer Designs

Input buffers are needed in the quadrature modulator and demodulator SiGe HBT MMIC's for several reasons. Input buffer can provide adjustment to compensate for the DC-offset present in the input signals to the quadrature modulator. The problem with high noise from the active mixers can be overcome if a low noise input buffer is placed in front of the mixer. Input buffers

provide single-ended to differential signal conversion. Differential signals reduce substrate coupling and instability problems due to parasitic ground and supply inductances [91]. An input buffer with low gain imbalance and phase imbalance is needed at the LO port to reduce the LO leakage to the input and output ports. The disadvantages of using input buffers are the reduced linearity and added complexity of the quadrature modulator/demodulator SiGe HBT MMIC's.

5.3.1 Differential Amplifier Stage with Shunt Feedback

From the above discussion it is clear that an ideal wideband input buffer, besides the usual requirement on gain flatness and phase linearity, should fulfill the additional requirements:

- Good wideband input impedance match.
- DC adjustment possibility.
- Low noise figure in 50Ω environment.
- Single-ended to differential signal conversion with low gain imbalance and phase imbalance over signal bandwidth.
- Simple circuit configuration.

The wideband input buffer shown in Fig. 5.16 can be designed to meet all the above requirements. The circuit consists of a differential amplifier stage (Q_1 and Q_2) with shunt feedback (R_f ,

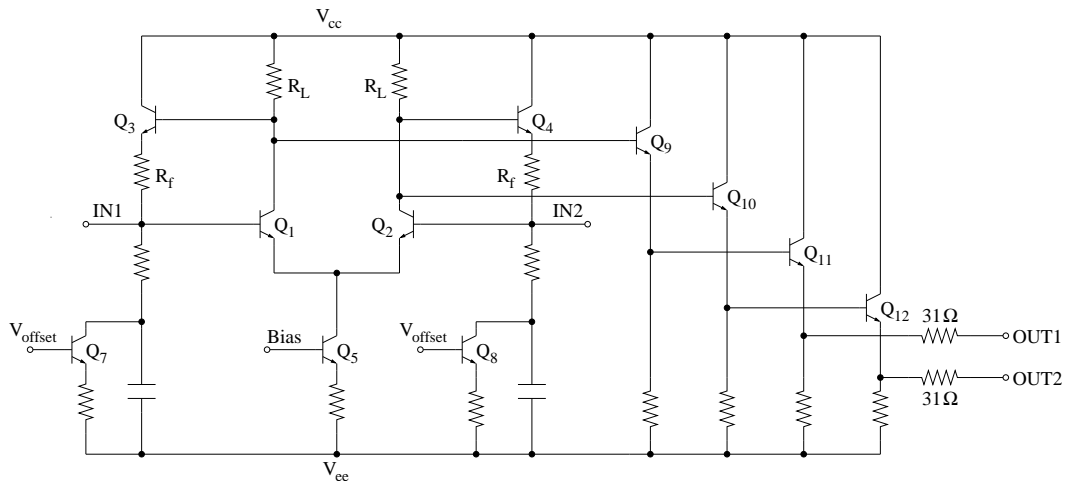


Figure 5.16 Wideband Input buffer using differential amplifier input stage with shunt feedback and DC offset adjustment.

Q_3 , and Q_4). The use of an emitter follower in the feedback path increases the base-collector voltage across the transistors (Q_1 , Q_2) which increase the bandwidth of the circuit without degrading the input impedance match and noise figure [94]. The emitter follower may, however, lead to stronger peaking due to the increased phase delay through the feedback path [95] and should be optimized carefully. The offset adjustment implemented with transistors (Q_7 and Q_8) controls the current through the feedback path which in turns controls the DC offset voltage [96]. Wideband operation for the input buffer is ensured by following the principle of strong impedance mismatch between succeeding stages. The emitter followers at the output are for improved mismatching, level shifting and output buffering. A series resistor of 31Ω has been added to the outer emitter follower stage to improve the output impedance match. This

also prevents the potential stability problem due to capacitive loading (from interconnect lines and pads) of the emitter followers at the last stage.

The analysis of the differential amplifier with shunt feedback can be performed using feedback theory, as was previously done for the shunt feedback load circuit for the active mixer. Things are, however, slightly complicated by the presence of the emitter follower in the feedback path. Due to the well known large bandwidth of emitter-followers [93], it can be assumed in the analysis that the frequency response of the feedback path is not of importance for describing the frequency response for the input buffer. The active feedback network can thus be analysed using the low-frequency two-port model shown in Fig. 5.17(a). The two-port Y-parameters for

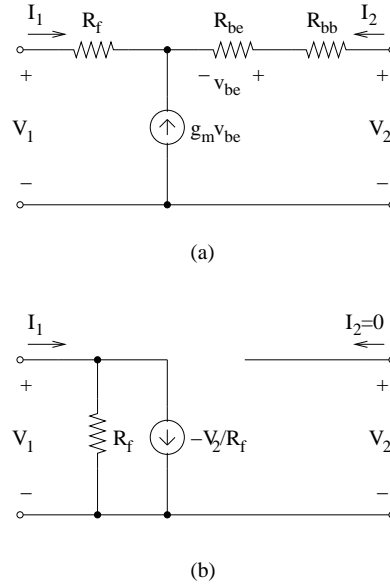


Figure 5.17 (a) Low-frequency two-port model for active feedback network. (b) Equivalent representation of the active feedback path.

the active feedback network are given as

$$Y_{fb} \approx \begin{bmatrix} \frac{1}{R_f} & -\frac{1}{R_f} \\ 0 & 0 \end{bmatrix} \quad (5.20)$$

where the approximation is valid if $\beta \gg 1$. The equivalent representation of the shunt feedback network shown in Fig. 5.17(b) clearly identifies the feedback transfer function f , and loading due to the active feedback network [93]. The input and output impedances for this circuit are given by Equations 5.15 and 5.16 respectively. Due to the reduced loading from the feedback network, $R'_L \approx R_L$ should be used for the load resistance. The low-frequency condition for impedance match to a source impedance R_s becomes

$$R_s = \frac{2R_f}{1 + g_m R_L} \quad (5.21)$$

where the factor of two accounts for the effective input impedance when the differential stage is driven from a single-ended voltage source V_s . That is, a factor of two results because the differential impedance is $2Z_i$. The transfer function for the input buffer is similar to that of the shunt feedback load stage used in the active mixer, and the same conclusions about the frequency response apply. In general, the feedback resistance R_f is a trade-off between high gain/low noise (high R_f) and large bandwidth (low R_f). Too low a value of R_f , however, leads to peaking and should be avoided.

5.3.2 Experimental Results

The shunt feedback input buffer was implemented in the $0.8\mu\text{m}$ SiGe HBT process from AMS. The layout of the circuit is shown in Fig. 5.18. Ground shielded pads have been applied for reduced substrate effects. An n-well shield was applied for all passive components. The circuit has been laid out in a highly symmetric and very compact manner. Both the positive and negative power supplies are decoupled on-chip using 17.85 pF capacitors. The chip size including pads is $0.9\times 0.6\text{ mm}^2$.

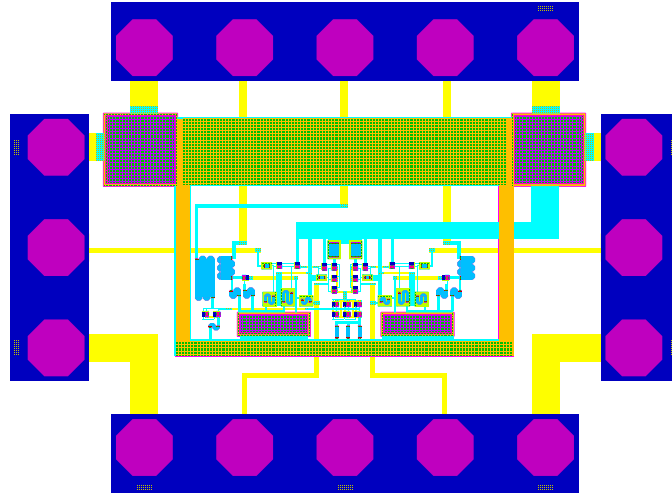


Figure 5.18 Layout of wideband SiGe HBT input buffer.

Measurement Condition and Experimental Setup

The performance of the wideband input buffer was verified by on-wafer S-parameter measurements using a HP 8510B network analyzer in the frequency range from 45 MHz - 10 GHz . The input buffer was measured applying the input signal through Cascade GSGSG probes with the unused port terminated in $50\ \Omega$. The two output signals of the input buffer were measured in turn using Cascade GSG probes with the unused port terminated in $50\ \Omega$. Bias supplies for the circuit were applied using a Cascade PPPPP probe. The current consumption for the input buffer was 17 mA from a $\pm 2.5\text{ V}$ supply voltage. A bias control voltage, V_{bias} , was used to adjust the bias current. The two DC offset adjustment voltages were connected together in all measurements (no imbalance compensation was used in the measurement). The experimental setup is seen in Fig. 5.19.

Measurement Results and Discussion

It has been stated in the literature, that the use of an emitter follower in the feedback path may lead to strong peaking due to the increased phase delay in the feedback loop [95]. The implementation of the DC adjustment network actually gives a possibility to experimentally investigate the influence of the shunt feedback path with emitter follower on the frequency response of the input buffer. In Fig. 5.20 (left plot), the benefits of the feedback path on the input return loss and gain for the input buffer are shown. A superior performance with respect to gain flatness, bandwidth, and input return loss was obtained using feedback, compared to the condition where the feedback path was disconnected ($V_{adj} = 0\text{ V}$). Also the phase characteristic was found to be more linear with feedback than without feedback present as shown in Fig. 5.20 (right plot)

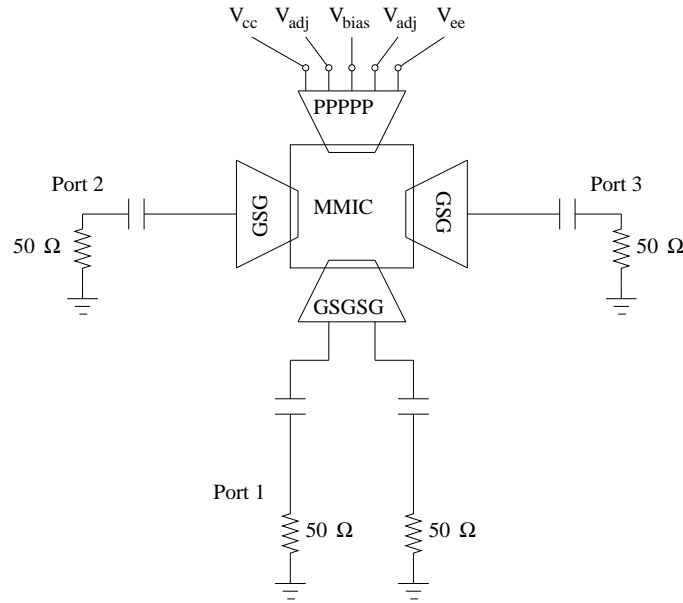


Figure 5.19 Experimental Setup.

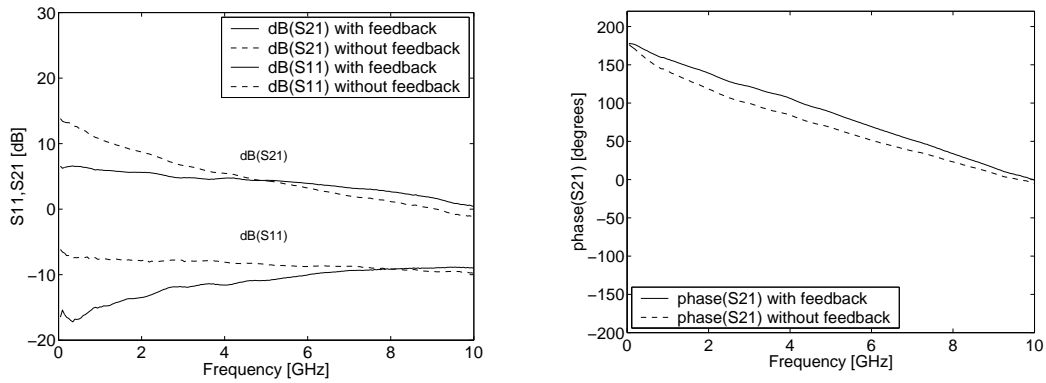


Figure 5.20 Influence of shunt feedback path on the frequency response for the input buffer. Left: Gain and input return loss. Right: Phase response.

The measured gain and phase of the input buffer from the input port (Port 1) to the output ports (port 2 and port 3) are compared to simulation results in Fig. 5.21 and Fig. 5.22. In general the prediction is reasonable, however, the measured 3-dB bandwidths of 6.6 GHz and 5.8 GHz for S_{21} and S_{31} respectively, are somewhat lower than predicted by simulations. The reason for this might be the combined influence from unaccounted interconnect line parasitics and poly resistor parasitics. The measurements shows a 1 dB high-frequency fall-off in the gain characteristic at 1.65 GHz and a $\pm 0.7^\circ$ deviation from linear phase from DC to 1.65 GHz for S_{21} . For S_{31} the high-frequency fall-off at 1.65 GHz is 0.8 dB, and the deviation from linear phase is $\pm 0.4^\circ$. In Fig. 5.23, the measured input and output return losses are compared with the prediction from simulations. From measurements an input return loss around -15 dB at frequencies below 2 GHz is found. Above 2 GHz the input return loss increases slightly but stays below approximately -10 dB. The same observations apply for the return loss at the two output ports. The good output port match arises because of the 31 Ω series resistors used. The measured input return loss is, however, approximately 10 dB above the simulation prediction for frequencies below 2 GHz while the measured output return loss differs by 5 dB. The input and output return losses are very sensitive to the value of the resistors explaining the observed

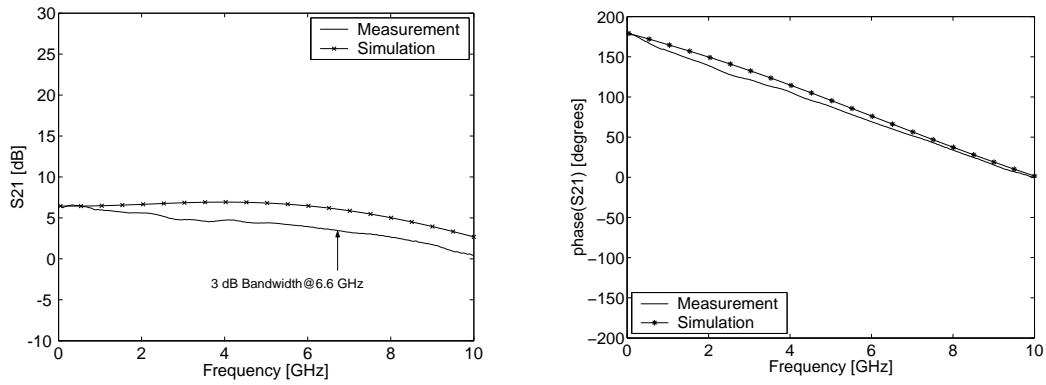


Figure 5.21 Comparison of measured and simulated frequency response S_{21} for wideband input buffer. Left: Gain. Right: Phase response.

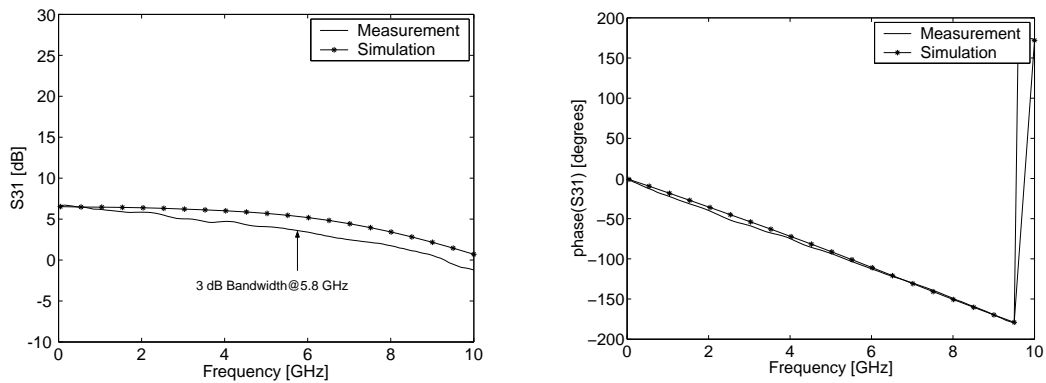


Figure 5.22 Comparison of measured and simulated frequency response S_{31} for wideband input buffer. Left: Gain. Right: Phase response.

difference between measurement and simulation results ³.

Finally the single-ended to differential conversion performance for the input buffer was investigated. In Fig. 5.24 the measured gain imbalance and phase difference is shown. The gain imbalance is below 0.5 dB for frequencies below 2 GHz and rises to 1.5 dB at 10 GHz. The phase difference is within the ideal 180° by $\pm 1^\circ$ for frequencies below 2 GHz but rises as the frequency increases.

The input buffer presented here, based on a differential stage with shunt feedback, seems well suited for use in quadrature modulator/demodulator subsystems for wideband SAR applications. The possible concern with unwanted peaking due to an emitter follower in the feedback path can be disregarded, as proven experimentally. Actually, the use of shunt feedback with an emitter follower is beneficial with respect to gain flatness, bandwidth, input impedance match, and phase linearity. Adding the excellent single-ended to differential conversion performance for this input buffer as well as the low circuit complexity it seems promising for further integration together with the quadrature mixers.

³Actually the 10 dB difference in input return loss could be caused by a change in low frequency input impedance from 40Ω to 45Ω .

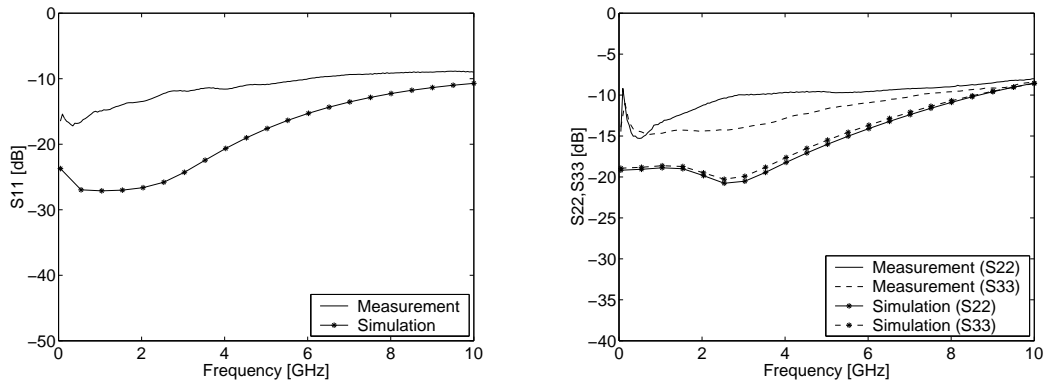


Figure 5.23 Comparison of measured and simulated frequency response of input and output return losses. Left: Input return loss. Right: Output return losses.

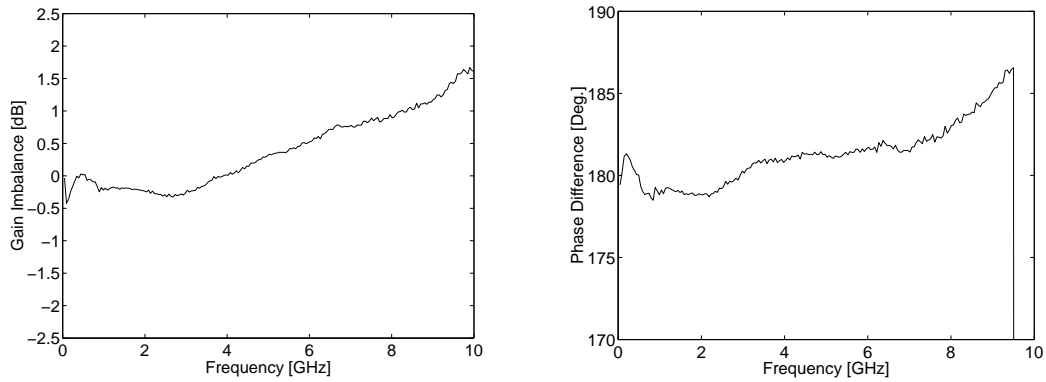


Figure 5.24 Measured single-ended to differential conversion performance. Left: Gain imbalance ($\text{dB}(S_{21}) - \text{dB}(S_{31})$). Right: Phase difference ($\text{phase}(S_{21}) - \text{phase}(S_{31})$).

5.4 System Design Simulation

The requirements on components for a wideband SAR system including monolithic microwave integrated circuits (MMICs) are related to the impulse response parameters for the total system, including transmitter, receiver and propagation path. In general, the MMICs should be designed for wide bandwidth, gain flatness, and phase linearity over the frequency band of interest in order not to degrade the impulse response parameters for the SAR system. Measurements of certain frequency response parameters, such as return loss, gain, and phase responses can give an indication of the suitability of a given design approach. It is, however, beneficial to be able to predict the impulse response parameters for a given MMIC design alone from simulation. In this section, a system design simulation using the designed SiGe HBT wideband active mixer applied in a quadrature demodulator configuration is described.

5.4.1 Quadrature Demodulator Configuration Simulation

The system design simulation was performed in HP ADS from Agilent. The principle block diagram for the quadrature demodulator configuration is shown in Fig. 5.25. Besides the SiGe HBT wideband active mixers, the quadrature demodulator consists of low pass filters, power

splitter and phase shifter. The low pass filters are implemented as the Butterworth type with 0.5 dB passband attenuation at 0.5 GHz and 40 dB stopband attenuation at 0.75 GHz in order to suppress the IF leakage. The local oscillator signal is implemented as a sinusoidal voltage source with available power of 0 dBm.

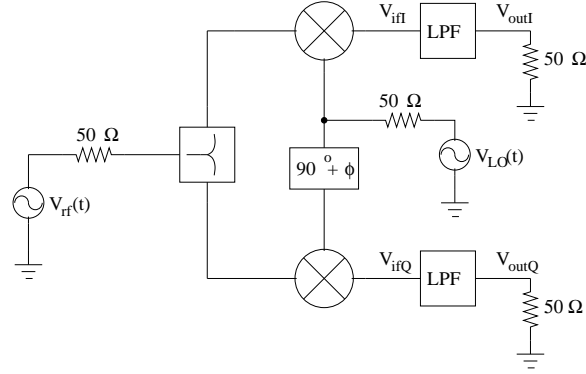


Figure 5.25 Quadrature demodulator configuration for system design simulation.

The quadrature demodulator is driven from a linear FM-modulated signal described as [97]

$$V_{IF}(t) = \begin{cases} A \cos \left(2\pi f_{IF}t + \pi \frac{B}{T_p} \left(t - \frac{T_p}{2} \right)^2 \right) & \text{for } 0 \leq t \leq T_p \\ 0 & \text{otherwise} \end{cases} \quad (5.22)$$

where f_{IF} is the IF frequency, B the signal bandwidth and T_p the pulse length. The complex baseband signal after quadrature demodulation is described as

$$m(t) = V_{outI} + jV_{outQ} \quad (5.23)$$

where V_{outI} and V_{outQ} are the in-phase and quadrature-phase components of the linear FM-modulated signal. In a real SAR system, a replica of the transmitted waveform serves as the reference modulation function for the matched filtering. In the system design simulation this corresponds to taking the reference modulation function as

$$m_{ref}(t) = \exp \left(\pi \frac{B}{T_p} \left(t - \frac{T_p}{2} \right)^2 \right). \quad (5.24)$$

The output of the matched filter is evaluated in the frequency domain as

$$S_o(f) = M(f)M_{ref}^*(f) \quad (5.25)$$

where $S_o(f)$, $M(f)$ and $M_{ref}(f)$ denotes the spectrum of the matched filter output, the complex baseband signal, and the reference modulation function respectively. Hamming weighting is applied to the spectrum of the complex baseband signal, before transforming back into the time-domain, in order to reduce the time side-lobes due to the uniform amplitude of the linear FM modulated signal. The matched filter output signal is shown in Fig. 5.26 for three different cases using an 800 MHz bandwidth linear FM-modulated signal at a 1.25 GHz IF frequency. The solid line represents the ideal impulse response obtained as the autocorrelation of the reference modulation function. The dotted line represents the matched filter output of the quadrature demodulator using Eq. 5.23 and thus includes the effect of the low pass filters. The main lobe is distorted and the sideband level is raised in this case, as a result of the poor phase linearity of the Butterworth filter used. The influence from the low pass filter can be eliminated by forming the complex baseband signal as

$$m(t) = V_{ifI} + jV_{ifQ} \quad (5.26)$$

and perform the necessary filtering as part of the signal processing. This case is shown as the dot-dashed line, hardly separable from the ideal impulse response. This shows that the designed SiGe HBT wideband active mixer does not degrade the impulse response performance for the total system.

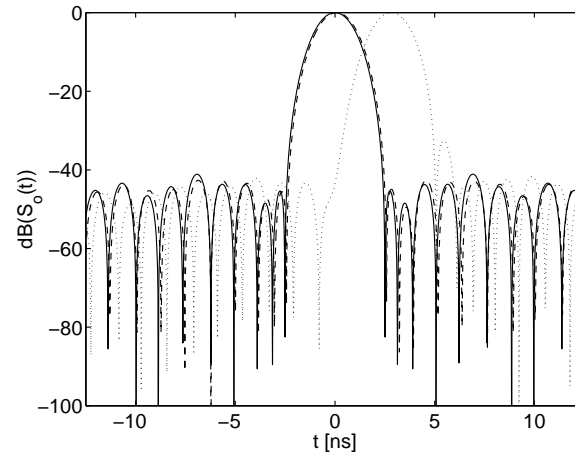


Figure 5.26 Matched filter output for quadrature demodulator using SiGe HBT MMICs ($f_{IF}=1.25$ GHz, $B=800$ MHz, $T_p=2\mu s$). The solid line is the ideal impulse response, the dotted line is the impulse response of the quadrature demodulator including the low pass filters and the dot-dashed line is the impulse response of the quadrature demodulator without the low pass filters.

Chapter 6

GaAs pHEMT Designs for RF Up/Downconverter Subsystem

High performance monolithic microwave integrated circuits are required for up/downconversion of wideband linear FM-modulated signals around microwave carriers in a SAR system. GaAs pHEMT technology have been chosen for implementing wideband active mixers for SAR applications at C- and X-band due to the high unity current gain frequency f_T for the devices in this technology.

The key specifications for the RF up/downconverter subsystem were given in chapter 2 of this thesis. In the present chapter the possible implementation of the GaAs pHEMT MMICs for the RF up/downconverter subsystem will be discussed. Very wideband performance has been reported for monolithic integrated mixers in InP HEMT technology based on the distributed mixing principle [98] and in GaAs HEMT technology based on a passive resistive mixer [99]. However the good microwave performance of GaAs pHEMT technology enables the design of very compact fully integrated double-balanced active mixers based on the Gilbert Cell mixer topology for downconversion applications up to 10 GHz as demonstrated in [25]. Frequency conversion between L-band and C/X-band in a wideband SAR system will be investigated here applying GaAs pHEMT technology for fully integrated double balanced active mixers.

In an upconverter for a wideband SAR system the LO leakage to the output port due to mixer imbalance is a serious concern as this signal causes passband ripples due to the AM/PM conversion process in the non-linear high-power traveling tube amplifier (the TWT). General equations are presented suitable for prediction of the various causes of LO leakage for a GaAs pHEMT Gilbert Cell mixer. Three special cases are considered in details. These are the effect of device mismatch, input balun imperfections and LO balun imperfections. The investigation of device mismatch shows the well-known result that LO leakage occurs due to mismatch in the lower devices of the Gilbert Cell mixer [17]. Input balun imperfections do not lead to LO leakage but the gain and phase imbalance affects the frequency converted signals. If the input balun imperfections vary over the frequency range of interest transfer function distortion may occur. LO balun imperfections lead to LO leakage at high frequency due to the forward transmission path through the gate-drain capacitance of the devices in the switching quad of the Gilbert Cell mixer. A differential output signal suppresses the LO leakage due to LO balun imperfections as verified by simulations.

A monolithic integrated wideband GaAs pHEMT active mixer design based on the Gilbert Cell mixer topology suitable for both up- and downconversion in a SAR system is then presented. Good balance over a wide bandwidth is assured by including wideband active baluns on both the input and LO port as well as a wideband active combiner at the output port. The experimental

results for the GaAs pHEMT active mixer achieves a conversion gain of 10 dB and a 3 dB bandwidth of 9.5 GHz on the RF port. The LO suppression is below -25 dB from 2-12 GHz. The experimental results are comparable to best published results for state-of-the-art highly integrated wideband active mixers based on FET technologies [21, 25, 100, 101]. However, the GaAs pHEMT active mixer seems useful only for downconversion from C-band to L-band as the measured bandwidth is not sufficient for operation to X-band.

6.1 RF Up/Downconverter Configuration

A possible implementation of a GaAs pHEMT MMIC for the RF up/downconverter subsystem is shown in Fig. 6.1. It consists of a double balance mixer and baluns on the input (RF/IF) and LO ports as well as a combiner on the output (IF/RF) port. A double-balanced structure is chosen because of the good port-to-port isolation and spurious signal rejection [85]. Wideband passive balun structures suitable for monolithic integration have been reported in [102] and [103]. However a careful examination of the experimental results for such passive balun structures shows that the possibility of achieving wideband operation combined with the required gain flatness and phase linearity needed in a SAR system is questionable. Therefore an all active design approach using active baluns, Gilbert Cell mixer topology and active output combiner is chosen to achieve wideband operation, avoid passband ripples due to passive balun structures and reduce size.

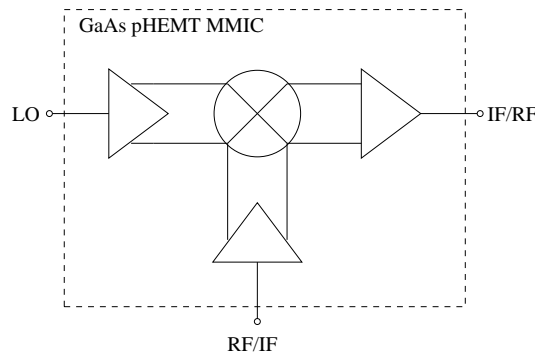


Figure 6.1 Implementation of GaAs pHEMT MMIC for the RF up/downconverter subsystem.

It will be attempted to use the same GaAs pHEMT MMIC for both the RF upconverter and RF downconverter subsystems. Thus wideband operation on all mixer ports are needed and the active baluns and combiner should ideally cover the full frequency range from L-band to X-band.

6.2 Balance Considerations in GaAs pHEMT Active Mixers

A schematic of a GaAs pHEMT active mixer suitable for monolithic integration is shown in Fig. 6.2 and consists of input balun, LO balun, Gilbert Cell mixer and an output combiner. Ideally the points where the drains of the upper devices ($FET3 - FET6$) are connected together represents a virtual ground for the input and LO signals and the drains of the lower device ($FET1 - FET2$) are virtual ground for the LO signal [85]. Thus the Gilbert Cell mixer topology ideally suppresses the LO leakage to the input and output ports as well as leakage from the input port to the output port. However due to the unavoidable device mismatch and balun imperfections the input and LO signal will leak to the output port. As mentioned before the LO

leakage to the output port in an upconverter for a wideband SAR system is a serious concern as this signal causes passband ripples due to the AM/PM conversion process in the TWT. The effect of device mismatch and balun imperfections for the GaAs pHEMT active mixer shown in Fig. 6.2 will now be discussed with emphasis on the mechanism leading to LO leakage.

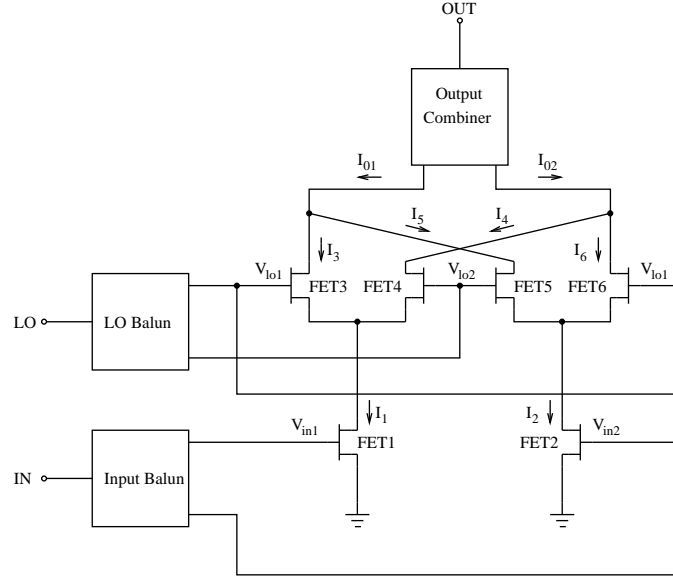


Figure 6.2 The GaAs pHEMT Active Mixer including input and LO port balun and output combiner.

An analytical treatment is possible assuming a Gilbert Cell mixer without any frequency limitations. However, LO leakage to the output port occurs at high frequencies due to the forward transmission path through the gate-drain capacitances of the switching devices ($FET3 - FET6$) and can not be neglected. This contribution is taken into account using a LO leakage coefficient γ . The lower devices ($FET1$ and $FET2$) are driven from small signal voltages V_{in1} and V_{in2} and the currents flowing in these devices are modeled as

$$I_1 = I_{ds} + \frac{\Delta I_{ds}}{2} + g_m V_{in1} \quad (6.1)$$

$$I_2 = I_{ds} - \frac{\Delta I_{ds}}{2} + g_m V_{in2} \quad (6.2)$$

where I_{ds} is the nominal DC-current in each of the transistors, ΔI_{ds} the DC-offset, g_m the transconductance of each device. The DC-offset is caused by device mismatch due to threshold voltage variation ΔV_t and device area mismatch [86]. The current flowing through the upper devices of the Gilbert Cell driven from a large LO signal at angular frequency ω_{LO} are modeled as

$$I_3 = \gamma V_{lo1} + I_1 \left(\frac{\alpha}{\pi} + \frac{2}{\pi} \left(\sin(\alpha) \cos(\omega_{LO} t) - \frac{\sin(2\alpha)}{2} \cos(2\omega_{LO} t) + \dots \right) \right) \quad (6.3)$$

$$I_4 = \gamma V_{lo2} + I_1 \left(\frac{\beta}{\pi} - \frac{2}{\pi} \left(\sin(\beta) \cos(\omega_{LO} t) - \frac{\sin(2\beta)}{2} \cos(2\omega_{LO} t) + \dots \right) \right) \quad (6.4)$$

$$I_5 = \gamma V_{lo2} + I_2 \left(\frac{\beta}{\pi} - \frac{2}{\pi} \left(\sin(\beta) \cos(\omega_{LO} t) - \frac{\sin(2\beta)}{2} \cos(2\omega_{LO} t) + \dots \right) \right) \quad (6.5)$$

$$I_6 = \gamma V_{lo1} + I_2 \left(\frac{\alpha}{\pi} + \frac{2}{\pi} \left(\sin(\alpha) \cos(\omega_{LO} t) - \frac{\sin(2\alpha)}{2} \cos(2\omega_{LO} t) + \dots \right) \right) \quad (6.6)$$

where the effect of LO balun imperfections on the switching process is combined with mismatch errors in the upper devices and cause a non-ideal duty cycle [84]. The non-ideal duty cycle

means that the devices $FET3$ and $FET6$ conduct currents in the period 2α and the devices $FET4$ and $FET5$ conduct currents in the remaining period, that is $2\beta = 2\pi - 2\alpha$. The nominal value of $\alpha = \pi/2$ occurs when the duty cycle is ideal. The high frequency LO leakage through the gate-drain capacitances is modeled using the LO leakage coefficient γ . The LO leakage coefficient is in general frequency dependent and gives a contribution to the current in the upper devices at the LO frequency due to the forward transmission of the LO drive signal. If a single-ended output is extracted ($I_3 + I_5$ or $I_4 + I_6$) the mixing process results in the following set of general equations

$$I_{01} = \frac{\alpha}{\pi} I_1 + \frac{\pi - \alpha}{\pi} I_2 + \frac{2}{\pi} \sin \alpha \cos(\omega_{LO} t) (I_1 - I_2) + \gamma(V_{lo1} + V_{lo2}) \quad (6.7)$$

$$I_{02} = \frac{\alpha}{\pi} I_2 + \frac{\pi - \alpha}{\pi} I_1 - \frac{2}{\pi} \sin \alpha \cos(\omega_{LO} t) (I_1 - I_2) + \gamma(V_{lo1} + V_{lo2}) \quad (6.8)$$

where higher order terms have been neglected because these do not contribute to the LO leakage. The differential output current formed from these equations is represented as

$$\Delta I_0 = \frac{1}{2}(I_{01} - I_{02}) = \frac{1}{2} \left(\frac{2\alpha}{\pi} - 1 \right) (I_1 - I_2) + \frac{2}{\pi} \sin(\alpha) \cos(\omega_{LO} t) (I_1 - I_2). \quad (6.9)$$

In the following three special cases of mismatch and balun imperfections are investigated based on these equations.

6.2.1 The Effect of Mismatch

The first case assumes ideal baluns but mismatch in the lower devices as well as in the upper devices of the Gilbert Cell mixer. The input signals are modeled as $V_{in1} = -V_{in2} = V_{in} \cos(\omega_{IN} t)$ where ω_{IN} is the input signal angular frequency. The differential output current from the mixing process is represented as

$$\Delta I_0 = \frac{1}{2} \left(\frac{2\alpha}{\pi} - 1 \right) \Delta I_{ds} + g_m \left(\frac{2\alpha}{\pi} - 1 \right) V_{in} \cos(\omega_{IN} t) + \frac{2}{\pi} \sin(\alpha) \Delta I_{ds} \cos(\omega_{LO} t) + \frac{2}{\pi} g_m V_{in} \sin(\alpha) \cos((\omega_{LO} + \omega_{IN})t) + \frac{2}{\pi} g_m V_{in} \sin(\alpha) \cos((\omega_{LO} - \omega_{IN})t) \quad (6.10)$$

and shows a residual DC-signal, input signal leakage, LO leakage and upper and lower sidebands at $\omega_{LO} \pm \omega_{IN}$. Notice that the input signal leakage depends on the matching accuracy in the upper devices of the Gilbert Cell mixer and the LO leakage depends on the mismatch in the lower devices as original stated in [17]. Furthermore it is noticed that the conversion transconductance G_{cnv} depends on the matching accuracy of the upper devices as shown by the equation

$$G_{cnv} = \frac{2}{\pi} g_m \sin(\alpha) \quad (6.11)$$

in agreement with recently published results for bipolar double balanced active mixers [84]. The amount of mismatch depends on the layout of the circuit and are therefore difficult to predict by simulations.

6.2.2 Input Balun Imperfections

The second case assumes ideal LO balun, zero device mismatch but non-ideal input balun. The input signals to the Gilbert Cell mixer in this case are modeled as

$$V_{in1} = V_{in}(1 + a) \cos(\omega_{IN} t + \phi) \quad (6.12)$$

$$V_{in2} = -V_{in} \cos(\omega_{IN} t) \quad (6.13)$$

where a and ϕ are the gain and phase imbalance for the input balun, respectively. If single-ended output is taken, and the gain and phase imbalance are small, the mixing process is represented as

$$I_{01} = g_m V_{in} \sqrt{a^2 + \phi^2} \cos(\omega_{IN} t) + \frac{2}{\pi} g_m V_{in} \left(1 + \frac{a}{2}\right) \cos((\omega_{LO} + \omega_{IN})t + \frac{\phi}{2}) + \frac{2}{\pi} g_m V_{in} \left(1 + \frac{a}{2}\right) \cos((\omega_{LO} - \omega_{IN})t - \frac{\phi}{2}) \quad (6.14)$$

and shows input signal leakage along with upper and lower sidebands at $\omega_{LO} \pm \omega_{IN}$. The LO leakage is fully suppressed in this case. If instead the output is taken differential the input signal leakage to the output port is suppressed and the mixing process is represented as

$$\Delta I_0 = \frac{2}{\pi} g_m V_{in} \left(1 + \frac{a}{2}\right) \cos((\omega_{LO} + \omega_{IN})t + \frac{\phi}{2}) + \frac{2}{\pi} g_m V_{in} \left(1 + \frac{a}{2}\right) \cos((\omega_{LO} - \omega_{IN})t - \frac{\phi}{2}). \quad (6.15)$$

It is observed that any gain imbalance or phase imbalance in the input balun are transferred to the frequency converted signals. If either the gain imbalance or phase imbalance varies over the frequency band of interest transfer function distortion occurs and degrades the impulse response parameters in a wideband SAR system.

6.2.3 LO Balun Imperfections

The third case assumes ideal input balun, zero device mismatch but non-ideal LO balun. Notice that $\alpha = \pi/2$ can be assumed in the present investigation as it has already been shown that the mismatch in the upper devices leads to input signal leakage and do not affect the LO leakage. The local oscillator signals are modeled as

$$V_{lo1} = V_{lo} (1 + a) \cos(\omega_{LO} t + \phi) \quad (6.16)$$

$$V_{lo2} = -V_{lo} \cos(\omega_{LO} t) \quad (6.17)$$

where a and ϕ are the gain and phase imbalance for the LO balun respectively. If single-ended output is taken, and the phase imbalance are small, the mixing process is represented as

$$I_{01} = \gamma \sqrt{a^2 + \phi^2} V_{lo} \cos(\omega_{LO} t) + \frac{2}{\pi} g_m V_{in} \cos((\omega_{LO} + \omega_{IN})t) + \frac{2}{\pi} g_m V_{in} \cos((\omega_{LO} - \omega_{IN})t) \quad (6.18)$$

and shows LO signal leakage along with upper and lower sidebands at $\omega_{LO} \pm \omega_{IN}$. If instead the output is taken differential the mixing process is represented as

$$\Delta I_0 = \frac{2}{\pi} g_m V_{in} \cos((\omega_{LO} + \omega_{IN})t) + \frac{2}{\pi} g_m V_{in} \cos((\omega_{LO} - \omega_{IN})t) \quad (6.19)$$

and the LO leakage signal is fully suppressed.

In order to verify the modeling of LO balun imperfections simulation on a GaAs pHEMT active mixer have been performed with ideal input balun and all devices matched. The LO balun is modeled with gain imbalance and phase imbalance, and the resulting LO suppression at the output port is observed. The LO suppression at 6.65 GHz LO frequency versus gain and phase imbalance is shown in Fig. 6.3. It is seen that for single-ended output an upconverter LO suppression of -38 dB below the wanted sideband (assumed here to be at 0 dBm power level) requires a gain and phase below 0.5 dB and 8 degrees, respectively. If the power level of the wanted sideband is lower than 0 dBm the requirements on LO balun imperfections becomes even more restrictive. If an active output combiner is included in the simulation on the GaAs pHEMT active mixer, it is shown in Fig. 6.3 that the required upconverter LO suppression can be met at relaxed LO balun requirements. The reason for this is that the LO leakage signal is suppressed due to the differential operation of the active output combiner as predicted from the modeling of LO balun imperfections.

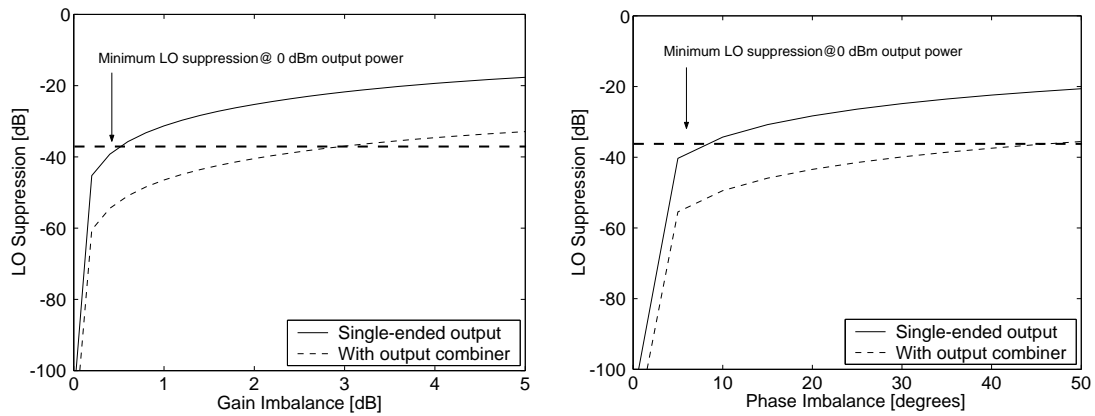


Figure 6.3 LO suppression at 6.65 GHz LO frequency in GaAs pHEMT active mixer with LO balun imperfections. Left: LO suppression versus gain imbalance. Right: LO suppression versus phase difference. The required upconverter LO suppression for an output power level of 0 dBm is shown as a thick dashed horizontal line.

6.3 Wideband GaAs pHEMT Active Mixer Design

The design considerations and experimental results for the GaAs pHEMT active mixer including active baluns, Gilbert Cell mixer and active output combiner are discussed in this section. The GaAs pHEMT MMIC requires no external matching, is ac coupled on the input and LO ports and DC coupled at the output port.

6.3.1 Active Balun Design

An active balun for the GaAs pHEMT active mixer MMIC should in addition to the usual requirements on gain flatness and phase linearity fulfill the following requirements:

- Good wideband input impedance match
- low noise figure in $50\ \Omega$ environment (for the input balun)
- low gain imbalance and phase imbalance to reduce LO leakage to the output port (for the LO balun)
- low gain imbalance and phase imbalance variations over the frequency range of interest to prevent transfer function distortion (for the input balun).

Topologically active baluns in FET technologies can be divided into three different configurations, the differential amplifier, the common-gate/common-source configuration and the FET phase inverter as shown in Fig. 6.4. In an ideal differential amplifier the applied single-ended voltage is evenly divided between the gate-to-source junctions of the differential transistor pair and perfectly balanced output signal results. In a real differential amplifier the finite common-mode rejection ratio due to the non-ideal impedance (Z_c) of the current source introduces a significant imbalance in the output signals. The highest possible common-mode rejection ratio is achieved by synthesis of a current source impedance with a negative real part [104]. The main problem with this configuration is that the synthesis of the optimal current source impedance

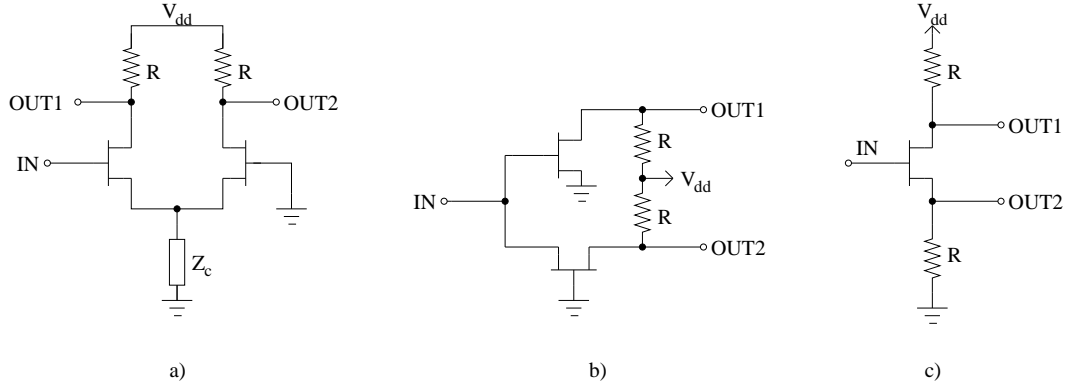


Figure 6.4 Active balun topologies. a) The differential amplifier. b) The common-gate/common-source configuration. c) The FET phase inverter.

over a wide frequency range is difficult. The common-gate/common-source configuration originally reported in [105] provide wideband impedance match due to the common-gate connected FET. It is capable of wideband operation, but the gain and phase imbalance are poor even at low frequencies [106]. The FET phase inverter is based on a FET in a combined source-follower/common-source degenerated configuration [85]. If the drain and source resistances are identical the voltage gain from the gate to the drain and source in this configuration is expressed at low frequencies as

$$G_v = \frac{\pm g_m R}{1 + g_m R + \frac{2R}{R_{ds}}} \quad (6.20)$$

where R is the drain and source load resistance, g_m is the transconductance of the FET and R_{ds} is the drain-source resistance of the FET. Thus the signals at the drain and source have equal amplitude and a phase difference of 180° . This condition can only be achieved at low frequencies because the parasitic capacitances of the FET will result in two different outputs at higher frequencies. To utilize this configuration in the gigahertz frequency range some kind of phase adjustment circuit must be used [107]. Initial experimental results have shown that the FET phase inverter exhibits small gain and phase imbalance (0.7 dB and 10° respectively) and is capable of wideband operation with excellent gain flatness and phase linearity over the frequency range of interest. The FET phase inverter thus seems like a promising active balun configuration for the GaAs pHEMT active mixer MMIC.

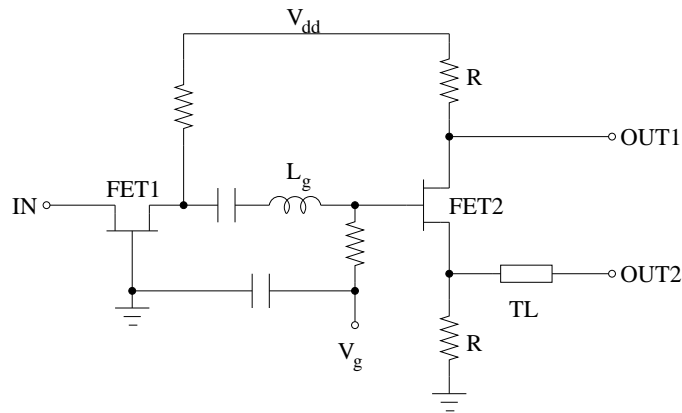


Figure 6.5 Active Balun based on the FET phase inverter configuration.

The schematic of an active balun design based on the FET phase inverter configuration is shown in Fig. 6.5. A FET device (*FET1*) in a common-gate configuration provides wideband active

impedance match to 50Ω [108]. An inductance (L_g) is included in series to the gate of the FET in the phase inverter ($FET2$) to extend the usable frequency range for the active balun. The value of this inductance is carefully optimized for gain flatness and phase linearity. The gate bias for $FET2$ is supplied through a high-value resistor. This biasing technique is very attractive since the gate draws no current and the resistor increases the stability of the circuit [41]. A transmission line following the source output of $FET2$ is one possible implementation of a phase adjustment circuit [107]. Fig. 6.6 shows the simulated performance of the FET phase inverter with and without the transmission line. A transmission line length of $250\mu\text{m}$ improves the phase imbalance variation over the frequency range from 45 MHz-26.5 GHz from above 20° to below 5° . Notice also the excellent gain imbalance possible with this active balun configuration. A possible concern with this active balun configuration is the difference in output impedance level at the drain and source terminal of $FET2$. If the following Gilbert Cell mixer is driven from non-identical source impedances imbalance is introduced in the circuit, especially at higher frequencies.

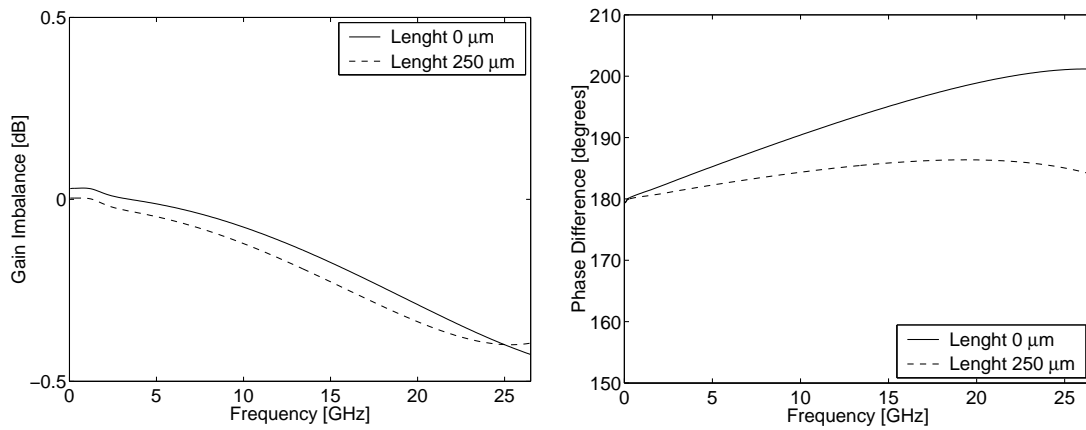


Figure 6.6 Simulated performance of FET phase inverter with and without phase adjustment circuit. Left: Gain Imbalance. Right: Phase difference.

6.3.2 Double Balanced Active Mixer Design

The main part of the active mixer is based on the Gilbert Cell mixer topology as shown in Fig. 6.7. The low output impedance of current sources in FET technologies do not eliminate the need for an input balun as is often the case in bipolar technologies. The current source commonly found in the transconductance stage of a Gilbert Cell mixer has been left out, because the input balun provide the necessary balanced input signal. This also improves the voltage headroom in the Gilbert Cell mixer. Because the bias level at the outputs of the active balun based on the FET phase inverter is non-identical, both the input and LO ports are ac coupled. It should be noticed that even a slight mismatch in the DC level input to the lower FET devices in the Gilbert Cell mixer would lead to LO leakage as explained previously. The input bias voltage ($V_{rf,bias}$) controls the bias current in the circuit and can provide adjustment if process spreading in the threshold voltage occurs. The LO bias voltage ($V_{lo,bias}$) provide the necessary gate bias voltage for the upper devices in the Gilbert Cell mixer. In the Gilbert Cell mixer the capacitive loading at the output node needs special attention if wideband operation is needed on the output port. In GaAs pHEMT technology the use of a shunt feedback load circuit, as applied successfully in the wideband SiGe HBT Gilbert Cell mixer, becomes impractical as the drain and gate bias needs to

be ac-coupled to prevent the devices from entering the linear region¹. Instead an inductor (L_L) is added in series with the load resistor R_L to compensate the high-frequency degradation of the conversion gain due to capacitive loading at the output [109]. This compensation technique is useful in the GaAs pHEMT Gilbert Cell mixer because of the high self-resonance frequency of the inductors available in this technology.

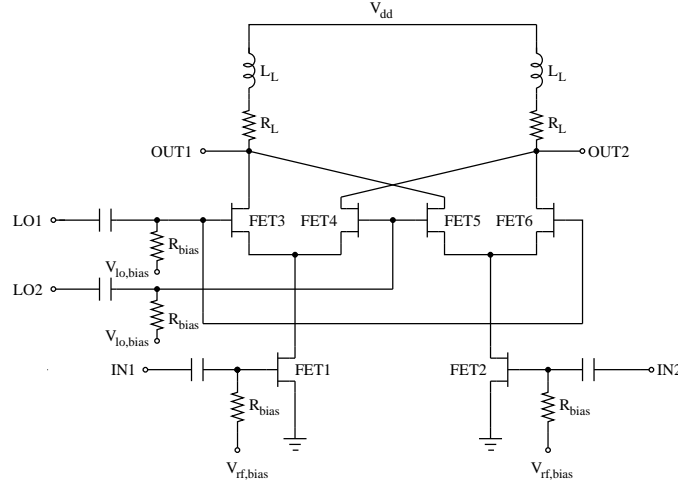


Figure 6.7 GaAs pHEMT active mixer based on the Gilbert Cell mixer topology.

6.3.3 Active Combiner Design

An active combiner is needed at the output of the Gilbert Cell mixer in order prevent the LO leakage, caused by LO balun imperfections, from reaching the output port. An active combiner design based on source follower stages and a differential amplifier output stage is shown in Fig. 6.8. With this configuration operation to DC is possible on the output port. Level shift diodes are inserted in the source follower stages to provide the necessary bias for the differential amplifier stage. The series resistance components of the level shift diodes degrades the frequency response of the source follower stages. Therefore a capacitor (C_s) is shunted across the diodes to provide a short for the high-frequency signal. This permit an increase in high-frequency gain and expansion of the bandwidth [109]. The differential amplifier stage is degenerated with source resistors for increased linearity and wideband operation. An open drain arrangement is used at the output because this allows for beneficial use of the bond inductance for further extension of the output port bandwidth and allows easy adaption to various load conditions.

6.3.4 Experimental Results

The designed wideband active mixer including active baluns, Gilbert Cell mixer and active output combiner have been implemented in the ED02AH process from OMMIC. GaAs pHEMTs with a gate length of $0.2\mu\text{m}$ and a unity current gain frequency f_T of 63 GHz are available with this process. The layout of the fabricated circuit is shown in Fig. 6.9. The circuit is laid out in a highly symmetrical manner to prevent device mismatch in the Gilbert Cell mixer. The balance of the active balun is improved if the source interconnect line length is slightly increased over the length of the drain interconnect line. However accidentally the length of the source and drain interconnection lines were interchanged during the layout part of the circuit so the drain interconnect line is actually longer than the source interconnect line. The balance of the active

¹For pHEMT devices the linear region corresponds to the saturated region for bipolar transistors and the gain of the devices drops significantly in this region.

current consumption was 64mA. Several bias voltages are needed for adjusting the bias points in the circuit. This allows the circuit to be adjusted for optimum RF performance even with large process spreading in the threshold voltage. During the measurements the unused output port was terminated in a 50Ω load. The output spectrum at the output port was measured using a HP 8563E spectrum analyzer. HP 8671B and HP 8672A synthesized CW signal generators (2-18 GHz) were used for the input and LO port respectively. The frequency dependent losses in the cables were estimated from through line calibration and subtracted from all measurements result. Measurement of the mixer phase response was not possible with the available equipment.

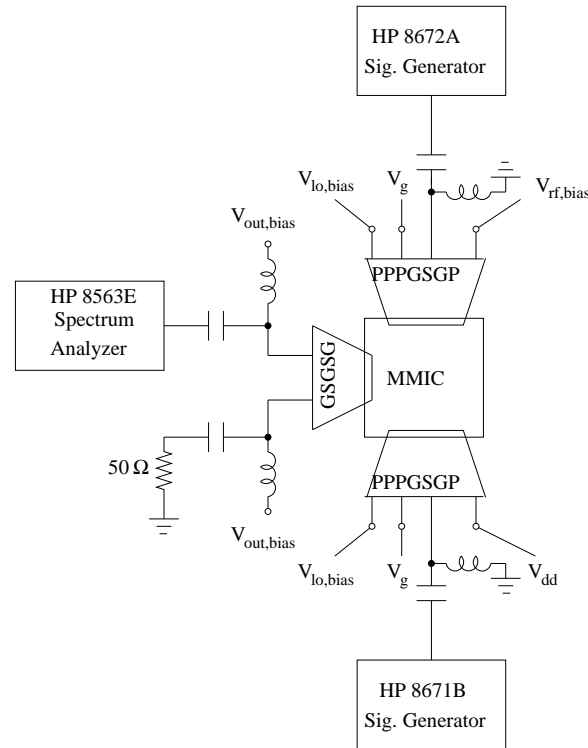


Figure 6.10 Experimental Setup.

Measurement Results and Discussion

The first part of the experimental investigation of the GaAs pHEMT active mixer is to find the LO power requirements for optimum conversion gain. In Fig. 6.11 the conversion gain from a RF frequency frequency of 5.4 GHz to IF frequency at 1.25 GHz is shown for a 6.65 GHz LO frequency. The conversion gain saturates at about 10 dB for LO power levels above 10 dBm. Therefore all succeeding measurements results are based on a LO power level of 12.5 dBm. The 1 dB compression point for the conversion gain is found at an input power level of -5 dBm which corresponds to an undistorted output signal at power levels below +5 dBm. An input power level of -30 dBm was used in all measurements assuring that conversion gain compression never occurs. The bandwidth limitation of the GaAs pHEMT active mixer are shown in Fig. 6.12. With both RF and LO ports swept in frequency with a fixed IF port frequency of 1.25 GHz a conversion gain of 10 dB and a 3 dB bandwidth of 9.5 GHz was achieved as shown the left plot of Fig. 6.12. The low RF port bandwidth makes the GaAs pHEMT active mixer unsuitable for downconversion from X-band to L-band. The measured conversion gain is well predicted by simulation at low frequencies however the high-frequency fall-off was not expected. This high-frequency fall-off is believed to be caused mainly by insufficient bandwidth performance

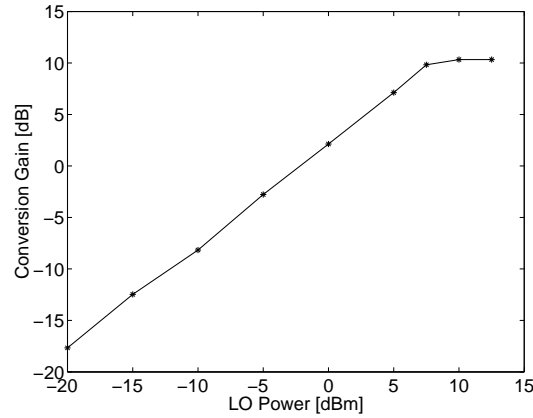


Figure 6.11 Conversion gain versus LO power ($f_{LO} = 6.65$ GHz, $f_{RF} = 5.4$ GHz, $f_{IF} = f_{LO} - f_{RF} = 1.25$ GHz).

of the active baluns. However the exact reason for this is still unknown. With swept RF port frequency and fixed LO port frequency at 2.2 GHz the frequency response at the IF port is as shown in the right plot of Fig. 6.12. The performance of the GaAs pHEMT active mixer was not optimized for the particular situation investigated in the right plot of Fig. 6.12 explaining the rather poor result in both measurement and simulation. The measured LO suppression is

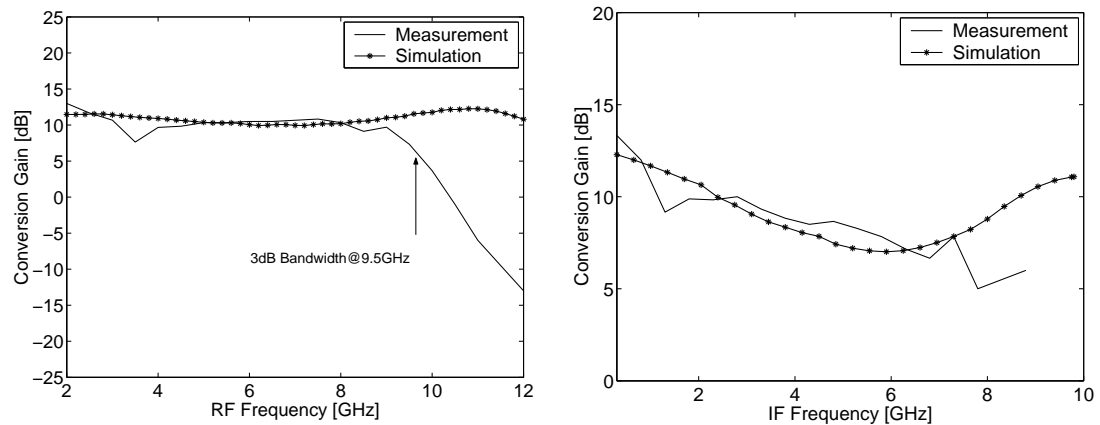


Figure 6.12 Comparison of measured and simulated input (RF) and output (IF) port bandwidth limitations for the GaAs pHEMT active mixer. Left: Conversion gain with swept RF frequency and fixed IF frequency ($f_{IF} = f_{LO} - f_{RF} = 1.25$ GHz). Right: Conversion gain with swept input (RF) frequency and fixed LO-frequency ($f_{LO} = 2.2$ GHz, $f_{IF} = f_{RF} - f_{LO}$).

better than -25 dB from 2-12 GHz as shown in Fig. 6.13. The expected LO suppression from simulation on the active mixer circuit with active baluns having zero transmission line length was about -40 dB. The observed difference may be explained by the non-optimal phase balance due to the interchange of the drain and source interconnect line lengths in the layout. The drop in LO suppression at higher frequencies supports the idea of limited bandwidth performance of the active baluns. If an unexpected drop in the gain of the active baluns occurs at higher frequencies less LO signal reaches the switching devices of the Gilbert Cell mixer and less LO signal leak to the output port.

In order to demonstrate the usefulness of the designed GaAs pHEMT active mixer in the C-band

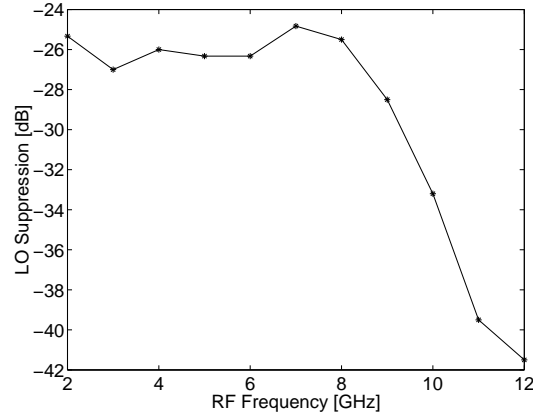


Figure 6.13 LO suppression at output port versus RF port frequency at fixed IF frequency ($f_{IF} = f_{LO} - f_{RF} = 1.25$ GHz).

RF downconverter subsystem, frequency conversion of a wideband linear FM-modulated signal from C-band to L-band was measured. The measured conversion gain versus RF frequency with fixed LO frequency at 6.65 GHz is shown in Fig. 6.14. The conversion gain characteristics shows a single ripple component of approximately 0.25 dB amplitude. Whether this is caused by measurements inaccuracy due to the spectrum analyzer measurement and calibration of cable losses or actually active mixer performance is unknown. However this single ripple component would lead to a PSLR performance of -30.6 dB barely fulfilling the requirement for the total SAR system. This example demonstrates clearly the difficulties experienced in the verification of monolithic microwave integrated circuits for a wideband SAR system. The performance of the GaAs pHEMT MMIC can only be verified by measurements in a SAR system.

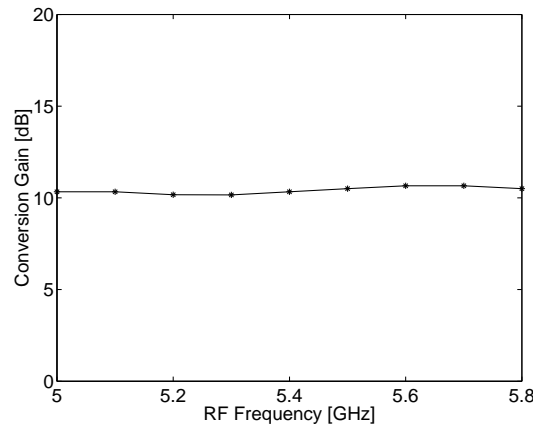


Figure 6.14 Measured demonstration of C-Band RF downconversion ($f_{LO} = 6.65$ GHz, $f_{IF} = f_{LO} - f_{RF}$).

In conclusions, the performance of the fully integrated GaAs pHEMT active mixer as a RF downconverter from C-band to L-band have been successfully demonstrated. The experimental results are comparable to best published results for state-of-the-art highly integrated wideband active mixers based on FET technologies [21, 25, 100, 101]. However, the GaAs pHEMT active mixer do not have sufficient bandwidth for operation at X-band. The insufficient bandwidth performance seems to be caused by the active baluns, however more measurements are needed in order to clarify the problem.

Chapter 7

Conclusions

In this thesis a technology study of monolithic microwave integrated circuits (MMICs) for future wideband SAR systems operating at L-, C-, and X-band has been performed. As a prerequisite for SAR applications, these MMICs should demonstrate high degree of gain flatness and phase linearity. A $0.8\mu\text{m}$, 35 GHz f_T SiGe HBT process and a $0.2\mu\text{m}$, 63 GHz f_T pHEMT GaAs process was chosen for the implementation of the key components in the quadrature modulator/demodulator and RF up/downconverter subsystems respectively.

To develop MMIC designs for a wideband SAR system, the accuracy of the available models becomes an important issue. An investigation of the influence of substrate effects on the frequency response of SiGe HBT wideband MMIC's is performed. It is concluded that it becomes necessary to include the substrate effects associated with pad structures and interconnect lines in the simulations in order to match measured results even at L-band frequencies. As part of the investigation, parameter extraction methods for device models including substrate parasitic are developed. Especially a direct parameter extracted method suited for modern poly-Si SiGe HBT devices is developed. The applicability of the direct parameter extraction method for VBIC95 model parameter extraction is successfully demonstrated.

Key components for the quadrature modulator/demodulator subsystems are wideband active mixers and input buffers. A simplified time-varying small-signal model for analyzing the main bandwidth limitation of active mixers based on the Gilbert Cell mixer topology has been proposed. The analysis shows that in general it is possible to consider separately frequency responses at the input and output port of the Gilbert Cell mixer. Advanced circuit techniques are exploited. They are useful when the objective is to achieve wideband operation with high degree of gain flatness and phase linearity on the mixer ports. Experimental results on a wideband active mixer implemented in the $0.8\mu\text{m}$, 35 GHz f_T SiGe HBT process from AMS achieves a 8.5 dB conversion gain with 3 dB bandwidth of 11 GHz and 7.5 GHz for the input and output ports respectively. The experimental results are very well predicted by simulations and demonstrates state-of-the-art results compared with other wideband active mixers implemented in comparable processes. In the frequency range of interest for the quadrature modulator and demodulator, the active mixer achieves excellent gain flatness when the LO frequency is fixed at 1.25 GHz. It is concluded that the designed SiGe HBT active mixer has sufficient bandwidth to be used as quadrature mixers in a wideband SAR system. The experimental results for an input buffer implemented in the $0.8\mu\text{m}$, 35 GHz f_T SiGe HBT process from AMS achieves a 3dB bandwidth of 6.6 GHz with a 1 dB high-frequency fall-off and good phase linearity at L-Band. The gain and phase imbalance for the single-ended to differential conversion are better than 0.5 dB and $\pm 1^\circ$ respectively at L-band. In conclusions, the wideband input buffer seems promising for further integration, however a redesign might be needed in order to achieve larger bandwidth

performance.

Further work on the quadrature modulator/demodulator involves the full integration of wideband active mixers, and wideband input buffers into quadrature modulator/demodulator SiGe HBT MMIC's. Furthermore the use of quadrature oscillators locked to a highly stable external reference oscillator is interesting from the point of view of increased integration level in the analog subsystems. Recently a $0.35\mu\text{m}$, 70 GHz f_T SiGe HBT process has become available at a low cost. The key components will be redesigned in this faster process, and a significantly larger bandwidth performance is expected.

Key components for the RF upconverter/downconverter includes wideband active mixers, active baluns and active output combiners. The LO leakage in the RF upconverter is of great concern in a SAR system due to the AM/PM modulation process in the following non-linear high-power amplifier (the TWT). Though filtering at the output of the RF upconverter may reduce the problem, a good balanced performance is desired in the RF upconverter. The causes of LO leakage in a GaAs pHEMT active mixer has been analyzed in terms of mismatch effects, input balun imperfections and LO balun imperfections. A fully integrated RF up/downconverter including an active mixer, active baluns on the input and LO port and an active output combiner on the output port was implemented in the $0.2\mu\text{m}$, 63 GHz f_T GaAs pHEMT process from OMMIC. The experimental results for the GaAs pHEMT MMIC demonstrates a 10 dB conversion gain and a 9.5 GHz 3 dB bandwidth at the RF port. These results are comparable to best published results for state-of-art highly integrated wideband active mixers based on FET technologies. RF downconversion from C-band to L-band is demonstrated with flat conversion gain over a 800 MHz bandwidth. The GaAs pHEMT active mixer seems useful only for downconversion from C-band to L-band as the measured bandwidth is not sufficient for operation to X-band. The experimental results for the GaAs pHEMT MMIC is well predicted by simulations up to approximately 8 GHz, however unexpected bandwidth limitation occurs at higher frequencies.

Further work on the RF upconverter/downconverter mainly includes an investigation of the cause of the insufficient bandwidth performance of the fully integrated GaAs pHEMT MMIC. Initial investigations indicates insufficient bandwidth performance for the active baluns, however, the exact reason for this is still unknown.

In general terms, wideband operation have been demonstrated for key components in modulators, demodulator, upconverters and downconverters in both SiGe HBT and GaAs pHEMT MMIC technology. The wideband operation was not achieved at the expense of gain flatness or phase linearity making the developed MMICs suitable for use in a wideband SAR system. Parameter extraction methods for device models including substrate effects have been developed in SiGe HBT technology. As a consequence, a high degree of prediction ability has been achieved for SiGe HBT wideband MMICs. Future work in this field should mainly concentrate on a higher level of monolithic integration of the critical subsystems, and the experimental evaluation of the MMICs bonded onto MCM modules.

References

- [1] E. Lintz Christensen, N. Skou, J. Dahl, K. W. Woelders, J. H. Joergensen, J. Granholm, and S. N. Madsen. EMISAR: An Absolutely Calibrated Polarimetric L- and C-band SAR. *IEEE Trans. Geoscience and Remote Sensing*, Vol. 36(6):1852–1865, Nov. 1998.
- [2] E. Lintz Christensen (ed), J. H. Joergensen, J. Dall, F. Hoeg, S. N. Madsen, J. Vidkjaer, J. Granholm, T. K. Johansen, N. Skou, and K. Woelders. SAR++ System Design Report. Technical Report R 693, Technical University of Denmark, Dept. of Electromagnetic Systems, Jan. 2000.
- [3] R. A. Pucel. Design Considerations for Monolithic Microwave Circuits. *IEEE Trans. Microwave Theory and Techniques*, Vol. MTT-29(6):513–534, 1981.
- [4] M. Ludwig, H.-P. Feldle, and H. Ott. A Miniaturised X-Band T/R-Module for SAR-Systems Based on Active Phased Array Techniques. In *Int. Geoscience and Remote Sensing Symposium*, pages 2063–2065, 1995.
- [5] Y. Butel, T. Adam, B. Cogo, and M. Soulard. A 6W C-Band High Power MMIC Amplifier For a Space Radar Application. In *2000 IEEE GaAs Symposium*, pages 215–218, 2000.
- [6] F. A. Petz, J. R. Guasch, C. Mavrocordatos, and C. V. Rao. Modular Design of SAR Electronics. *IEEE Trans. Microwave Theory and Techniques*, Vol. 47(12):2220–2227, Dec. 1999.
- [7] J. Sevenhans, F. O. Eynde, and P. Reusens. The Silicon Radio Decade. *IEEE Trans. Microwave Theory and Techniques*, Vol. 50(1):235, Jan. 2002.
- [8] C. Kermarrec. RF IC Techniques from GaAs to SiGe to CMOS. In *APMW02 Workshop: RF Technologies for Wireless Terminals*, pages 217–223, 2002.
- [9] G. Freeman et al. 40-Gb/s Circuits Built From a 120-GHz f_T SiGe Technology. *IEEE Trans. Solid-State Circuits*, 37(9):1106–1115, Sept. 2002.
- [10] K. W. Kobayashi. Design and Technology Trades of 10 Gb/s and 40 Gb/s Transimpedance Amplifiers. In *2002 Asia Pacific Microwave Conference*, pages 925–930, 2002.
- [11] M. L. Skolnik. *Introduction to Radar Systems*. McGraw-Hill International Editions, second edition, 1980.
- [12] S. N. Madsen et al. KRAS’86 Design Report. Technical Report R 690, Technical University of Denmark, Dept. of Electromagnetic Systems, Oct. 1986.
- [13] D. R. Wehner. *High Resolution Radar*. Artech House, first edition, 1987.

- [14] E. L. Christensen, S. N. Madsen, and N. Skou. Review of the the Homodyne Technique for Coherent Radar. In *IEEE International Radar Conference*, pages 159–163, 1990.
- [15] S. J. Roome. Analysis of Quadrature Detectors Using Complex Envelope Notation. *IEE Proceedings*, Vol. 136(2):95–100, April 1989.
- [16] B. Gilbert. A Precise Four-Quadrant Multiplier with Subnanosecond Response. *IEEE Journal of Solid-State Circuits*, SC-3(4):365–373, Dec. 1968.
- [17] A. Bilotti. Applications of a Monolithic Analog Multiplier. *IEEE Journal of Solid-State Circuits*, SC-3(4):373–380, Dec. 1968.
- [18] K.W. Kobayashi et al. A DC-20GHz InP HBT Balanced Analog Multiplier for High-Data-Rate Direct-Digital Modulation and Fiber-Optic Receiver Applications. *IEEE Transaction on Microwave Theory and Techniques*, 48(2):194–202, Feb. 2000.
- [19] J. Wholey, I. Kipnis, and C. Snapp. Silicon Bipolar Double Balanced Active Mixer MMIC's for RF and Microwave Applications up to 6GHz. In *IEEE Microwave and Millimeter-Wave monolithic Circuits Symposioum*, pages 133–137, 1988.
- [20] P. Weger et al. Gilbert Multiplier as An Active Mixer with Conversion Gain of up to 17 GHz. *Electronic Letters*, 27(7):570–571, Mar. 1991.
- [21] S. Fujita, Y. Imai, Y. Yamane, and H. Fushimi. DC-10GHz Mixer and Amplifier GaAs ICs for Coherent Optical Heterodyne Receiver. In *IEEE International Solid-State Circuits Conference*, pages 122–125, 1991.
- [22] J. Glenn et al. 12-GHz Gilbert Mixers using A Manufacturable Si/SiGe Epitaxial-Base Bipolar Technology. In *IEEE Bipolar/BiCMOS Circuit Tech. Meeting*, pages 186–189, 1995.
- [23] S. Hackl et al. Low-noise, low-power monolithic integrated active 20GHz mixer in SiGe technology. *Electronic Letters*, 37(1):36–37, Jan. 2001.
- [24] K. Osafune and Y. Yamauchi. 20-GHz 5-dB-Gain Analog Multipliers with Al-GaAs/GaAs HBT's. *IEEE Transaction on Microwave Theory and Techniques*, 42(3):518–520, Mar. 1994.
- [25] C.F. Campbell and J.M. Beall. Design and Performance of a Highly Integrated Wideband Active Downconverter MMIC. In *IEEE Radio Frequency Integrated Circuits Symp.*, 2001.
- [26] W. Durr et al. Low-power low-noise active mixers for 5.7 and 11.2GHz using commercially available SiGe HBT MMIC technology. *Electronic Letters*, Vol.34(No.21):1994–1996, Oct. 1998.
- [27] K.W. Kobayashi et al. InAlAs/InGaAs HBT X-band Double-Balanced Upconverter. *IEEE Journal of Solid-State Circuits*, Vol.29(No. 10):1238–1243, Oct. 1994.
- [28] Austria Mikro Systeme International AG. BYS/BYR 0.8 μ m SiGe HBT-CMOS. Process Data Sheet, Sept. 1999.
- [29] Austria Mikro Systeme International AG. High Performance SiGe Road Show. SiGe Seminar, Lund, Sweden, March 2000.
- [30] M. Nakamae. SiGe HBT Technologies: Expectations and Realizations. In *EuMW 99 Workshop: Silicon and SiGe Technologies and Circuits*, pages 8–11, 1999.

- [31] J. D. Cressler. SiGe HBT Technology: A New Contender for Si-based RF and Microwave Circuit Applications. *IEEE Transaction on Microwave Theory and Techniques*, Vol. 46(5):572–589, May 1998.
- [32] S. Wada et al. A Manufacturable 0.18- μm SiGe BiCMOS Technology for 40-Gb/s Optical Communication LSIs. In *IEEE Bipolar/BiCMOS Circuit Tech. Meeting*, pages 84–87, 2002.
- [33] J. C. Cowles. A Comparison of SiGe and GaAs HBT Technologies for RFICs. In *EuMW Workshop: Silicon and SiGe Technologies and Circuits*, pages 12–17, 1999.
- [34] C. T. Kirk. A Theory of Transistor Cutoff Frequency (f_T) Falloff at High Current Densities. *IRE Trans. Electron Devices*, ED-9:164–174, 1962.
- [35] H. F. Cooke. Microwave Transistors: Theory and Design. *Proc. IEEE*, Vol. 59:1163–1181, Aug. 1971.
- [36] D.L. Harnage et al. Si/SiGe Epitaxial-Base Transistors-Part I: Materials, Physics, and Circuits. *IEEE Transaction on Electron Devices*, Vol. 42(3):455–468, March 1995.
- [37] L. Larson and M. J. Delaney. Applications of Si/Si/Ge Technology for High-Speed Communications Systems. In *IEEE MTT-S Digest*, pages 1077–1080, 1999.
- [38] G. Gonzalez. *Microwave Transistor Amplifiers: Analysis and Design*. Prentice Hall, second edition, 1984.
- [39] J. Vidkjaer. Class Note 48260 RF-Communication: Linear, Active two-ports, Noise and Distortion. Technical Report NB221, Technical University of Denmark, Dept. Electromagnetic Systems, 2000.
- [40] <http://cmp.imag.fr/>.
- [41] I. D. Robertson, editor. *MMIC Design*. The Institution of Electrical Engineers, 1995.
- [42] H. M. Rein, M. Pfof and T. Holzwarth. Modeling of the Substrate Effect in High-Speed Si-Bipolar ICs. In *Proc. IEEE 1995 BCTM*, pages 182–185, 1995.
- [43] H. M. Rein, M. Pfof and T. Holzwarth. Modeling Substrate Effects in the Design of High-Speed Si-Bipolar IC's. *IEEE Jour. Solid-State Circuits*, Vol. 31(10):1493–1501, Oct. 1996.
- [44] R. Gharpurey. Modeling and Analysis of Substrate Coupling in Integrated Circuits. *IEEE Jour. Solid-State Circuits*, Vol. 31(3):344–353, Mar. 1996.
- [45] M. Pfof and H. M. Rein. Modeling and Measurement of Substrate Coupling in Si-Bipolar IC's up to 40 GHz. *IEEE Jour. Solid-State Circuits*, Vol. 33(4):582–591, April 1998.
- [46] M. Pfof, H. M. Rein, W. Steiner, and A. Sturmer. Simulation of Substrate Coupling with Special Regard to Shielding in High-Speed Si/SiGe Bipolar ICs. In *29th European Microwave Conference*, pages 133–136, 1999.
- [47] N. K. Verghese, D. J. Allstot, and M. A. Wolfe. Verification Techniques for Substrate Coupling and Their Application to Mixed-Signal IC Design. *IEEE Jour. Solid-State Circuits*, Vol. 31(3):354–365, Mar. 1996.

- [48] J. T. Colvin, S. S. Bhatia, and K. K. O. Effect of Substrate Resistances on LNA Performance and a Bondpad Structure for Reducing the Effect in a Silicon Bipolar Technology. *IEEE Jour. Solid-State Circuits*, Vol. 34(9):1339–1344, Sept. 1999.
- [49] J. Vidkjær. Substrate effects in HBT modelling for RFIC design. In *ECCTD*, 2001.
- [50] E. Sonmez et al. Parameter extraction of Si-Ge HBT's for a scalable MEXTRAM model and performance verification by a Si-Ge HBT MMIC active reveive mixer design for 11 GHz. In *Topical meeting on Silicon monolithic integrated circuits in RF systems*, pages 159–162, 2000.
- [51] D. Costa, W. U. Liu, and J. S. Harris. Direct Extraction of the AlGaAs/GaAs Heterojunction Bipolar Transistor Small-Signal Equivalent Circuit. *IEEE Trans. Electron Devices*, Vol. 38(9):2018–2024, Sept. 1991.
- [52] S. Lee, B. R. Ryum, and S. W. Kang. A New Parameter Extraction Technique for Small-Signal Equivalent Circuit of Polysilicon Emitter Bipolar Transistors. *IEEE Trans. Electron Devices*, Vol. 41(2):233–238, Feb. 1994.
- [53] S. Bousnina et al. A New Analytical and Broadband Method for Determining the HBT Small-Signal Model Parameters. In *IEEE MTT-S Digest*, pages 1397–1400, 2000.
- [54] Y. Suh et al. Direct Extraction Method for Internal Equivalent Circuit Parameters of HBT Small-Signal Hybrid- Π Model. In *IEEE MTT-S Digest*, pages 1401–1404, 2000.
- [55] E. Wasige et al. An analytic expression for the HBT extrinsic base-collector capacitance derived from S-parameter measurements. In *IEEE MTT-S Digest*, pages 733–736, 2002.
- [56] B.S. Kim et al. Analytic determination of hybrid π equivalent circuit parameters of SiGe HBTs using admittance equations. In *Asia-Pacific Microwave Conference*, pages 466–469, 2002.
- [57] A. Fraser, R. Gleason, and E.W. Strid. GHz on-silicon-wafer probing calibration methods. In *IEEE BCTM*, pages 154–157, 1988.
- [58] P.J. van Wijnen, H. R. Claessen, and E. A. Wolsheimer. A new straightforward calibration and correction procedure for "on wafer" high-frequency s-parameter measurements (45 mhz-18 ghz). In *IEEE BCTM*, 1987.
- [59] M. Koolen, J. Geelen, and M. Versleijen. An improved de-embedding technique for on-wafer high-frequency characterization. In *IEEE BCTM*, pages 188–191, 1991.
- [60] H. Cho and D. E. Burk. A Three-Step Method for the De-Embedding of High-Frequency S-Parameter Measurements. *IEEE Trans. Electron Devices*, Vol. 38(6):1371–1375, June 1991.
- [61] T. E. Kolding. *On-Wafer Measuring Techniques for Characterizing RF CMOS Devices*. PhD thesis, Aalborg University, RISC-Group Denmark, Denmark, 2000.
- [62] Ian Getreu. *Modeling the Bipolar Transistor*. Tektronix, Inc., 1976.
- [63] M. P. J. G. Versleijen. Distributed High Frequency Effects in Bipolar Transistors. In *IEEE 1991 Bipolar Circuits and Technology Meeting*, pages 85–88, 1991.
- [64] H. C. de Graff and F. M. Klaassen. *Compact Transistor Modeling for Circuit Design*. Springer-Verlag, 1990.

- [65] S. Lee and A. Gopinath. Parameter Extraction Techniques for HBT Equivalent Circuit Usign Cutoff Mode Measurement. *IEEE Trans. Microwave Theory and Techniques*, Vol. 40(3):574–577, March 1992.
- [66] Y. Gobert, P. J. Tasker, and K. H. Bachem. A Physical, Yet Simple, Small-Signal Equivalent Circuit for the Heterojunction Bipolar Transistor. *IEEE Trans. Microwave Theory and Techniques*, Vol. 45(1):149–153, Jan. 1997.
- [67] J. A. Seitchik, C. F. Machala, and P. Yang. The Determination of Spice Gummel-Poon Parameters by a Merged Optimization-Extraction Technique. In *IEEE 1989 Bipolar Circuits and Technology Meeting*, pages 275–278, 1989.
- [68] C. McAndrew et al. VBIC95: An Improved Vertical, IC Bipolar Transistor Model. In *IEEE 1995 Bipolar Circuits and Technology Meeting*, pages 170–177, 1995.
- [69] C. C. McAndrew et al. VBIC95, The Vertical Bipolar Inter-Company Model. *IEEE Jour. Solid-State Circuits*, Vol. 31(10):1476–1483, Oct. 1996.
- [70] C. C. McAndrew and L. W. Nagel. Spice Early Modeling. In *IEEE 1994 Bipolar Circuits and Technology Meeting*, pages 144–147, 1994.
- [71] <http://www.designers-guide.com/VBIC/references.html>.
- [72] B. Senapati and C. K. Maiti. Advanced SPICE modelling of SiGe HBTs using VBIC Model. *IEE Proc. Circuits Devices Syst.*, Vol. 149(2):129–135, April 2002.
- [73] G. M. Kull, L. W. Nagel, S. Lee, P. Lloyd, E. J. Prendergast, and H. Dirks. A Unified Circuit Model for Bipolar Transistors Including Quasi-Saturation Effects. *IEEE Transaction on Electron Devices*, Vol. ED-32(6):1103–1113, June 1985.
- [74] M. Shur. *Physics of Semiconductor Devices*. Prentice Hall, 1990.
- [75] S. V. Cherepko and J. C. M. Hwang. VBIC Model Applicability and Extraction Procedure for InGaP/GaAs HBT. In *Asia Pacific Microwave Conference*, pages 716–721, 2001.
- [76] G.A.M. Hurkx. The Relevance of f_T and f_{max} for the Speed of a Bipolar CE Amplifier Stage. In *IEEE Bipolar/BiCMOS Circuit Tech. Meeting*, pages 53–56, 1996.
- [77] T. Okamura, C. Kurioka, Y. Kuraishi, O. Tsuzuki, T. Senba, M. Ushirozawa, and M. Fujimaru. 10-GHz Si Bipolar Amplifier and mixer IC's for Coherent Optical Systems. *IEEE Jour. Solid-State Circuits*, Vol. 27(12):1775–1780, Dec. 1992.
- [78] H. M. Rein, L. Schmidt, K. Worner, and Wilhelm Pieper. Wide-Band Symmetrical Analog Multiplier IC for Coherent Optical-Fiber Receivers Operating up to 10 gb/s. *IEEE Jour. Solid-State Circuits*, Vol. 26(12):1840–1846, Dec. 1991.
- [79] K. J. Negus and J. N. Wholey. Multifunction Silicon MMIC's for Frequency Conversion Applications. *IEEE Trans. Microwave Theory and Techniques*, Vol. 38(9):1191–1198, 1986.
- [80] H. Kikuchi, S-Konaka, and M. Umehira. GHz-Band Monolithic Modem IC's. *IEEE Trans. Microwave Theory and Techniques*, Vol. MTT-35(12):1277–1282, Dec. 1987.
- [81] T. Tsukahara, M. Ishikawa, and M. Muraguchi. A 2-V 2-GHz Si-Bipolar Direct-Conversion Quadrature Modulator. *IEEE Jour. Solid-State Circuits*, Vol. 31(2):263–267, Feb. 1996.

- [82] T. Tsukahara and J. Yamada. 3 to 5GHz Quadrature Modulator and Demodulator using a Wideband Frequency-Doubling Phase Shifter. In *2000 IEEE International Solid-State Circuits Conference*, pages 384–385, 2000.
- [83] E. Tiliharju and K. Halonen. A Quadrature-Modulator for 0.6-2.6GHz with Frequency Doubler. In *2002 IEEE international Symposium on Circuits and Systems*, pages 429–432, 2002.
- [84] D. Coffing and E. Main. Effects of Offsets on Bipolar Integrated Circuit Mixer Even-Order Distortion Terms. *IEEE Trans. Microwave Theory and Techniques*, Vol. 49(1):23–30, Jan. 2001.
- [85] S. A. Maas. *Microwave Mixers*. Artech House, INC, 2nd. edition, 1993.
- [86] R. G. Meyer. Intermodulation in High-Frequency Bipolar Transistor Integrated-Circuit Mixers. *IEEE Jour. Solid-State Circuits*, Vol. SC-21(4):560–563, 1986.
- [87] S. A. Maas. *Nonlinear Microwave Circuits*. Artech House, INC, 1. edition, 1988.
- [88] K.L. Fong and R.G. Meyer. Monolithic RF Active Mixer Design. *IEEE Transaction on Circuits and Systems-II: Analog and Digital Signal Processing*, 46(3):231–239, Mar. 1999.
- [89] K. Ohhata, T. Masuda, E. Ohue, and K. Washio. Design of a 32.7-GHz Bandwidth AGC Amplifier IC with Wide Dynamic Range Implemented in SiGe HBT. *IEEE Jour. Solid-State Circuits*, Vol. 34(9):1290–1297, Sept. 1999.
- [90] E. M. Cherry and D. E. Hooper. The design of wide-band transistor feedback amplifiers. *Proc. I.E.E.*, Vol. 110(2):375–389, Feb. 1963.
- [91] H.-M. Rein and M. Moller. Design Considerations for Very-High-Speed Si-Bipolar IC's Operating up to 50 Gb/s. *IEEE Jour. Solid-State Circuits*, Vol. 31(8):1076–1090, Aug. 1996.
- [92] M. Moller, H.-M. Rein, and H. Wernz. 13 Gb/s Si-Bipolar AGC Amplifier IC with High Gain and Wide Dynamic Range for Optical-Fiber Receivers. *IEEE Jour. Solid-State Circuits*, Vol. 29(7):815–822, July 1994.
- [93] P. R. Gray and R. G. Meyer. *Analysis and Design of Analog Integrated Circuits*. John Wiley & Sons, Inc., third edition, 1993.
- [94] H. Knapp, D. Zoschg, T. Meister, K. Aufinger, S. Boguth, and L. Treitinger. 15 GHz Wideband Amplifier with 2.8 dB Noise Figure in SiGe Bipolar Technology. In *2001 Radio Frequency Integrated Circuits Symposium*, pages 287–290, 2001.
- [95] M. Neuhauser, H.-M. Rein, and H. Wernz. Low-Noise, High-Gain Si-Bipolar Preamplifiers for 10 Gb/s Optical-Fiber Links—Design and Realization. *IEEE Jour. Solid-State Circuits*, Vol. 31(1):24–29, Jan. 1996.
- [96] W. Pohlmann. A Silicon-Bipolar Amplifier for 10 Gbit/s with 45 dB Gain. *IEEE Jour. Solid-State*, Vol. 29(5):551–556, May 1994.
- [97] N. Skou and B. Laursen. Additional Radar Notes for 48372. Technical Report NB218, Technical University of Denmark, Dept. Electromagnetic Systems, 1998.
- [98] Y. Imai, S. Kimura, Y. Umeda, and T. Enoki. DC to 38-GHz distributed analog multiplier using InP HEMT's. *IEEE Microwave Guided Wave Letter*, pages pp.399–401, Dec. 1994.

- [99] T. H. Chen, K. W. Chang, S. T. Bui, L. T. Liu, G. S. Dow, and S. Pak. Broadband Single- and Double-Balanced Resistive HEMT Monolithic Mixers. *IEEE Trans. Microwave Theory and Techniques*, Vol. 43(3):477–484, March 1995.
- [100] M. Kasashima, K. Tanaka, H. Yamazaki, K. Tanaka, and H. Nakamura. 2-8 GHz Gilbert-Cell Mixer IC for 2.5Gb/s Coherent Optical Transmission. In *IEEE 1993 GaAs IC Symposium*, pages 295–298, 1993.
- [101] C. F. Campbell. A Wideband pHEMT Downconverter MMIC for Satellite Communication Systems. In *IEEE MTT-S Digest*, pages 55–58, 1998.
- [102] T. Chen, K. W. Chang, S. B. Bui, H. Wang, G. S. Dow, L.T. Liu, T. S. Lin, and W. S. Titus. Broadband Monolithic Passive Baluns and Monolithic Double-Balanced Mixer. *IEEE Trans. Microwave Theory and Techniques*, Vol. 39(12):1980–1996, Dec. 1991.
- [103] C. Trantanella, M. Shifrin, and B. Bedard. Low Cost, Plastic Encapsulated Mixers for C/X-Band Applications. In *1998 IEEE Radio Frequency Integrated Circuits Symposium*, pages 131–134, 1998.
- [104] J. Gonzalez. A New Active Structure of High Frequency Wideband Differential Phase Shifters. *Int. Jour. Microwave and Millimeter-Wave Computer-Aided Engineering*, Vol. 6(2):107–114, 1996.
- [105] A. M. Pavio, R. H. Halladay, S. D. Bingham, and G. A. Sapshe. Double Balanced Mixers Using Active and Passive Techniques. *IEEE Trans. Microwave Theory and Techniques*, Vol. 36(12):1948–1957, Dec. 1988.
- [106] M. C. Tsai, M. J. Schindler, W. Struble, M. Ventresca, R. Binder, R. Waterman, and D. Danzilio. A Compact Wideband Balanced Mixer. In *IEEE 1994 Microwave and Millimeter-Wave Monolithic Circuits Symposium*, pages 135–138, 1994.
- [107] H. Kamitsuna and H. Ogawa. Ultra-Wideband MMIC Active Power Splitters with Arbitrary Phase Relationships. *IEEE Trans. Microwave Theory and Techniques*, Vol. 41(9):1519–1523, Sept 1993.
- [108] K. B. Niclas. Active Matching with Common-Gate MESFET's. *IEEE Trans. Microwave Theory and Techniques*, Vol. 33(6):492–499, June 1985.
- [109] H. Kikuchi, Y. miyagawa, and T. Kimura. Broad-Band GaAs Monolithic Equalizing Amplifiers for Multigigabit-per-Second Optical Receivers. *IEEE Trans. Microwave Theory and Techniques*, Vol. 38(12):1916–1923, Dec. 1990.

Optimization of SiGe HBT VCOs for Wireless Applications

Tom K. Johansen, Student Member, IEEE[†], Lawrence E. Larson, Fellow, IEEE

Department of Electrical and Computer Engineering, Center for Wireless Communications
University of California — San Diego

[†] Oersted-DTU, Department of Electromagnetic Systems
Technical University of Denmark — 2800 Kgs. Lyngby, Denmark

Abstract — This paper describes the optimization of phase noise performance in fully integrated SiGe HBT differential LC-tuned voltage-controlled oscillators (VCOs) for wireless applications. An accurate expression for phase noise in SiGe HBT LC-tuned VCOs is presented which takes the nonlinear operation of the oscillator into account. Design methods are shown which minimize the different sources of phase noise toward the intrinsic limit set by the resonator quality factor. A set of 2 GHz SiGe HBT VCOs have been implemented in a 0.5 μm , 47 GHz SiGe BiCMOS process to provide experimental verification of the benefits of the design methods presented in this paper.

I. INTRODUCTION

The present growth in wireless communication demands more available channels. This in turn leads to stringent requirement on the frequency stability of the local oscillators in wireless systems. Thus in recent years phase noise in fully integrated VCOs have been a topic of active research [1]-[2]. Due to their relative good phase noise performance, differential LC-tuned oscillators, are usually the preferred topology for fully integrated VCOs [3].

This paper presents the analysis and design of a fully integrated 2 GHz SiGe HBT LC-tuned VCO with very low phase noise implemented in a 0.5 μm , 47 GHz, SiGe BiCMOS process. SiGe HBT technology was chosen due to the excellent noise performance of the transistors in this technology [4]. First an accurate expression for phase noise in SiGe HBT differential LC-tuned VCOs is presented which takes the non-linear operation of the oscillator into account. Next the insight gained from the analysis is used to design a SiGe HBT VCO with very low phase noise.

The experimental results for a set of 2 GHz SiGe HBT VCOs shows the benefits of the design methods presented in this paper. The VCOs demonstrates very low-phase noise performance at low power consumption compared with other recent published results for SiGe HBT VCOs.

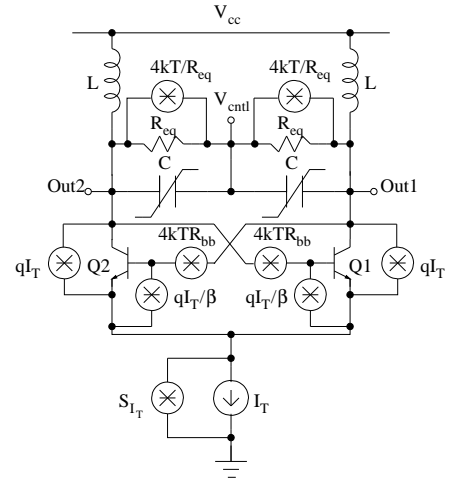


Fig. 1. SiGe HBT differential LC-tuned VCO with noise sources.

II. PHASE NOISE IN SiGe HBT DIFFERENTIAL LC-TUNED VCOs

A simplified schematic of a SiGe HBT differential LC-tuned VCO with its most important noise sources is seen in Fig. 1. The cross-coupled differential transistor pair presents a negative resistance to the resonator due to positive feedback. This negative resistance cancel the losses from the resonator enabling sustained oscillation. Frequency variation is achieved with a reverse-biased pn-junction diode or MOS varactor. The resonator losses are modeled as an equivalent resistance R_{eq} in parallel to the resonator.

A. Non-linear Phase Noise Analysis

The close-in phase noise behavior at an offset f_m from the carrier frequency f_0 in the differential LC-tuned VCO is found from Leeson's model [5]

$$\mathcal{L}(f_m) = \frac{2kTR_{eq}F}{A_0^2} \left(\frac{f_0}{2Qf_m} \right)^2 \left(1 + \frac{\Delta f_{1/f^3}}{f_m} \right) \quad (1)$$

where k is Boltzmann's constant, T is the absolute temperature, A_0 is the amplitude of oscillation, Q is the resonator loaded quality factor, $\Delta f_{1/f^3}$ is the corner frequency where $1/f$ device noise no longer predominate and F is the excess noise factor.

The excess noise factor is determined by the wide-band noise from the cross-coupled differential transistor pair and the tail current source taking the non-linear operation of the oscillator into account

$$F \approx 1 + \frac{R_{bb}}{2R_{eq}} \left(\frac{f_t}{f_0} \right) + \frac{S_{I_T} R_{eq}}{8kT} + \frac{qI_T R_{eq}}{4kT} \left(\frac{\Delta V}{\pi A_0} \right)^2 \left(1 + \sin^2 \left(\frac{\Delta V}{2A_0} \right) \right) \quad (2)$$

where ΔV is the signal level required to make the cross-coupled differential transistor pair switch completely to one side, f_t is the unity current gain frequency, I_T is the dc tail current and S_{I_T} is tail current source noise spectral density. This expression is derived using conversion-matrix analysis [6] on the oscillator circuit assuming the only important non-linearity is the transconductance of the cross-coupled transistor pair.

B. Up-conversion of Low-Frequency Noise

The excess noise factor in Leeson's model only includes noise injected into the feedback path of the VCO. A different phase noise mechanism is the up-conversion of low-frequency noise sources due to the modulation of non-linear elements in the oscillator. Taking this up-conversion into account a more accurate expression for phase noise becomes

$$\mathcal{L}(f_m) = \frac{2kTR_{eq}F}{A_0^2} \left(\frac{f_0}{2Qf_m} \right)^2 + \frac{|K_{I_T}|^2}{2f_m^2} S_{I_T} + \frac{|K_{AM}|^2}{2f_m^2} \left(\frac{2}{\pi} \right)^2 R_{eq}^2 S_{I_T} + \frac{|K_{VCO}|^2}{2f_m^2} S_{R_v} \quad (3)$$

where $|K_{I_T}|$ and $|K_{AM}|$ are defined as the sensitivity of the frequency of oscillation on low-frequency tail current variations due to the indirect stability effect and varactor AM-to-PM conversion respectively [7]-[8]. The sensitivity of the frequency of oscillation on control voltage noise with spectral density S_{R_v} is described by the varactor gain $|K_{VCO}|$ [9].

III. LOW PHASE NOISE SiGe HBT VCO DESIGN

The implementation of a low phase noise differential LC-tuned VCO with noise filter and fully integrated resonator is seen in Fig. 2 and will serve as the basis for the following discussion. The variable capacitance for frequency tuning is implemented with a series connection of pn-junction diodes with capacitance C_v and a MIM-capacitance C_m . This configuration linearizes the

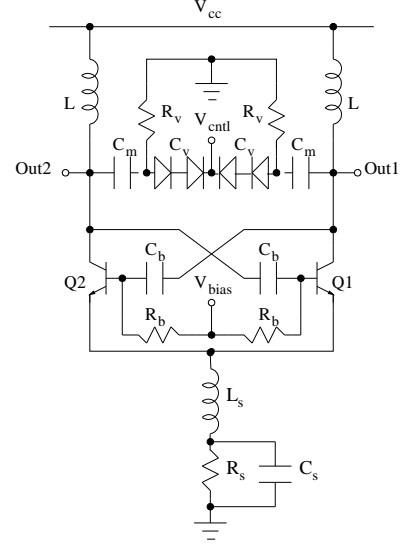


Fig. 2. SiGe HBT VCO with noise filter and fully integrated resonator.

overall capacitance variation with control voltage V_{cntl} at the expense of reduced tuning range. In the present design a quality factor $Q \approx 10$ is predicted for the fully integrated resonator at 2 GHz.

A. Improvement by Noise Filtering the Current Source

In SiGe HBT differential LC-tuned VCOs the excess noise factor F is dominated by the noise from the tail current source near even harmonics of the carrier frequency. In order to improve phase noise this contribution has to be minimized. An efficient way of doing this is to use a noise filtering technique [10]. In Fig. 2 inductor L_s and capacitor C_s forms a 2nd order low-pass filter which prevents noise at even harmonics from being injected into the feedback path of the oscillator. Inclusion of different size inductors shows regions of both phase noise improvement and degradation over the first order low-pass case with the capacitor C_s alone. This degradation of phase noise is explained by the increasing inductance driving the oscillator into the saturation region as illustrated in Fig. 3. In this figure the simulated phase noise performance versus tail current is compared to calculated phase noise using (3) and neglecting the contributions from shot noise and tail current source noise. It is seen that the phase noise has been reduced toward the intrinsic limit set by the resonator quality factor. The reason for this is that inclusion of a large tail capacitance C_s makes the transistors in the cross-coupled differential pair conduct in pulses at the peak of the oscillation waveform. Due to the cyclostationary property of the shot noise sources this will be the ideal operation condition with respect to

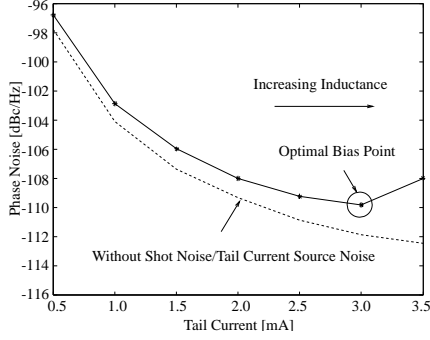


Fig. 3. Phase noise at 100 KHz offset from 2 GHz carrier versus tail current. Solid line: simulation, dashed line: calculated from (3) without shot noise and tail current source noise contribution.

phase noise for the oscillator [1].

B. Indirect Stability and Effect of Varactor Non-linearity

The noise filter leaves low-frequency noise from the tail current source unaffected. Two mechanisms by which this gets transformed into close-in phase noise is by the indirect stability effect and the AM-to-PM conversion of the varactors. The indirect stability effect is due to the modulation of the phase shift in the feedback loop caused by low-frequency variations in the tail current. According to Barkhausen's criterion this results in a variation of the frequency of oscillation [8]. An open-loop gain analysis on the differential LC-tuned VCO without noise filter gives the frequency of oscillation as

$$f_0 \approx \frac{1}{2\pi\sqrt{LC}} \left(1 - \frac{1}{2\pi\sqrt{LC}} \frac{R_{bb}}{2Qf_t R_{eq}} \right) \quad (4)$$

and predicts a rise in the frequency of oscillation at low current levels due to the current dependence of f_t . Once driven into saturation the frequency of oscillation drops due to the corresponding reduction of f_t in this region. When the noise filter is present the open-loop gain depends on the capacitor C_s which tend to reduce the variation of the frequency of oscillation with tail current. It is found however that this reduction depends on the device sizes with significant effect only for relative large devices. This is believed to be due to the fact that f_t is lower for larger devices at a given current level and therefore the reduction with the noise filter present is more significant for larger devices. From (3) it is seen that the contribution to phase noise due to the indirect stability effect depends on the sensitivity of the frequency of oscillation on tail current variations $K_{I_T} = \frac{\partial f_0}{\partial I_T}$. This sensitivity is evaluated for the SiGe HBT VCO with and without noise filter as seen in Fig. 4. The small sensitivity observed with noise filter present

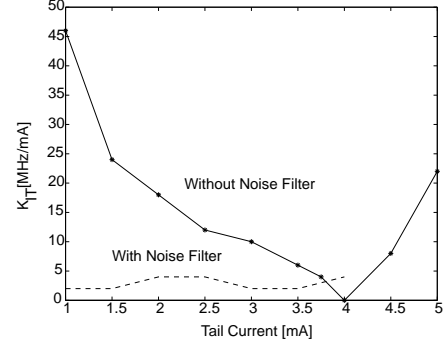


Fig. 4. Oscillation frequency sensitivity on tail current variations. Solid line: without noise filter, dashed line: with noise filter.

is due to the use of relative large devices which leads to reduced variation of the frequency of oscillation with tail current according with the above explanation.

Low-frequency noise from the tail current source is also up-converted to the carrier as amplitude modulation. Due to the non-linear $C - V$ characteristic of the varactors this amplitude modulation results in phase modulation. The contribution to phase noise depends on the frequency sensitivity on the oscillation amplitude variations $K_{AM} = \frac{\partial f_0}{\partial A_0}$. It can be evaluated by biasing the VCO where $K_{I_T} \approx 0$ and injecting a low-frequency current tone through the tail current source and observing the power in the up-converted sidebands. A sensitivity of only $|K_{AM}| = 6.4 \frac{MHz}{V}$ at $V_{cntl} = 0$ is calculated for the SiGe HBT VCO because of the good linearity of the MIM-varactor configuration used.

Low-frequency noise on the tuning line modulates the non-linear capacitance of the varactors giving rise to phase noise variation with control voltage. The contribution to phase noise due to this noise is dependent on the frequency sensitivity on control voltage variations $K_{VCO} = \frac{\partial f_0}{\partial V_{cntl}}$. The phase noise degradation due to control voltage noise is very significant at the lower tuning range where the varactors are most non-linear [9]. The stack of two varactors as seen in Fig. 2 reduces the varactor gain K_{VCO} at the lower tuning range which in turn reduces phase noise variation with control voltage.

IV. EXPERIMENTAL RESULTS

A set of three fully integrated 2 GHz VCOs have been implemented in IBM's 0.5 μm SiGe BiCMOS 5AM process. This process offers a thick top Al metalization layer for high Q-factor inductors. The first VCO (VCO1) is implemented with the noise filter and stacked varactors. The second VCO (VCO2) is identical to the first except that the inductor in the noise filter have been removed. A third VCO (VCO3) was implemented using single

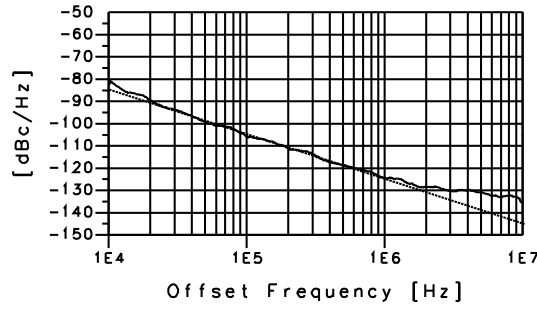


Fig. 5. Phase noise measurement between 10 KHz and 10 MHz offset from a 2.15 GHz carrier for VCO1. The dashed reference line have a 20dB/decade slope.

varactors scaled to provide the same overall capacitance variation as with the stacked varactors.

The VCOs were measured on-wafer using a Cascade probe station. Phase noise performance were measured using a HP 8563E spectrum analyzer with HP 85671A phase noise utility function. The wideband phase noise performance of the first VCO is shown in Fig. 5. Due to the very low $1/f$ device noise corner frequency in SiGe HBT technology the phase noise slope is 20 dB/decade until the noise floor of the measurement setup is reached. A summary of the measured performance for all three VCOs are shown in Table. I. The designed VCOs have identical phase noise performance; however the VCO without the inductor in the noise filter have higher power consumption than the other two. The phase noise variation over the tuning range is lowest in the VCOs with stacked varactors. This is due to the reduced tuning gain K_{VCO} at the lower tuning range. The tuning range however is lowered with stacked varactor which is explained by the larger parasitic capacitance present in this configuration. The single-ended output power for all VCOs are better than -5 dBm.

Different VCOs are compared using a Figure-of-Merit (FOM) that normalizes the phase noise performance to the same frequency, offset and power consumption [11] as

$$FOM = \mathcal{L}(f_m) - 20 \log \frac{f_o}{f_m} + 10 \log \frac{P_{diss}}{1mW} \quad (5)$$

	VCO1	VCO2	VCO3
Frequency [GHz]	2.150	2.161	2.156
Phase noise@100KHz [dBc/Hz]	-105.7	-105.3	-105.3
Tuning Range [MHz]	176	172	265
Phase noise variation [dBc/Hz]	2.47	3.00	3.84
Power consumption [mW]	10.8	12.2	10.8

TABLE I
SUMMARY OF VCO PERFORMANCE.

where P_{diss} is the dc power dissipated by the VCO. In this work we achieve a Figure-of-Merit of -182.0 dBc/Hz which is comparable to the best published results for Si/SiGe bipolar VCOs [7], [11]-[13].

V. CONCLUSIONS

Phase noise in SiGe HBT VCOs has been analyzed and design methods to reduce it toward the limit set by the resonator quality factor have been investigated. The design methods have been experimentally proven by measurement on a set of SiGe HBT VCOs showing low phase noise at low power consumption.

ACKNOWLEDGEMENTS

The authors would like to acknowledge the support of the UCSD Center for Wireless Communications and its member companies, and the support of IBM under a UPP program.

REFERENCES

- [1] A. Hajimiri and T.H. Lee, "A General Theory of Phase Noise in Electrical Oscillators," *IEEE J. Solid-State Circuits*, vol. 33, no. 2, pp. 179–194, Feb 1998.
- [2] C. Samori, A.L. Lacaita, F. Villa and F. Zappa, "Spectrum Folding and Phase Noise in LC Tuned Oscillators," in *IEEE Trans. Circuit and Systems-II*, vol. 45, no. 7, pp. 781–790, July 1998.
- [3] A. Hajimiri and T.H. Lee, "Design Issues in CMOS Differential LC Oscillators," in *IEEE J. Solid-State Circuits*, vol. 34, no. 5, pp. 717–724, May 1999.
- [4] G. Niu et al, "Transistor Noise in SiGe HBT RF Technology," in *IEEE 2000 BCTM*, 2000, pp. 207–210.
- [5] D. B. Leeson, "A Simple Model of Feedback Oscillator Noise Spectrum," in *Proceedings of the IEEE*, vol. 54, no. 2, pp. 329–330, 1966.
- [6] S. A. Maas, in *Nonlinear Microwave Circuits*, Norwood, MA, 1988.
- [7] A. Zanchi, C. Samori, S. Levantino and A. L. Lacaita, "A 2-V 2.5-GHz -104 dBc/Hz at 100 kHz Fully Integrated VCO with Wide-Band Low-Noise Automatic Amplitude Control Loop," in *IEEE J. Solid-State Circuits*, vol. 36, no. 14, pp. 611–619, April 2001.
- [8] C. Samori, A. L. Lacaita, A. Zanchi, S. Levantino and G. Calì, "Phase Noise Degradation at High Oscillation Amplitudes in LC-Tuned VCO's," in *IEEE J. Solid-State Circuits*, vol. 33, no. 12, pp. 1987–1991, Dec. 1998.
- [9] J.W.M Rogers, J.A. Macedo and C. Plett, "The effect of Varactor Nonlinearity on the Phase Noise of Completely Integrated VCOs," in *IEEE J. Solid-State Circuits*, vol. 35, no. 9, pp. 1360–1367, Sept. 2000.
- [10] E. Hegazi, H. Sjolund, and A. Abidi, "A Filtering Technique to Lower Oscillator Phase Noise," in *IEEE International Solid-State Circuits Conference*, pp. 364–365, 2001.
- [11] J. Plouchart, H. Ainspan, M. Soyuer and A. Ruehli, "A Fully-Monolithic SiGe Differential Voltage-Controlled Oscillator for 5 GHz Wireless Applications," in *IEEE Radio Frequency Integrated Circuits Symposium*, pp. 57–60, 2000.
- [12] J. Maurant, J. Imbornone and T. Tewksbury, "A Low Phase Noise Monolithic VCO in SiGe BiCMOS," in *IEEE Radio Frequency Integrated Circuits Symposium*, pp. 65–68, 2000.
- [13] X. Wang, D. Wang, K. Schelkle and P. Bacon, "Fully Integrated Low Phase Noise VCO Design in SiGe BiCMOS Technology," in *IEEE Radio and Wireless Conference*, pp. 109–112, 2001.